Fakultät für Physik und Astronomie
Ruprecht-Karls-Universität Heidelberg

Diplomarbeit
Im Studiengang Physik
vorgelegt von

Jan Egberts
aus Mülheim / Ruhr
2009

Untersuchungen zur transversalen Strahlprofilmessung mit hoher dynamischer Weite

Die Diplomarbeit wurde von

Jan Egberts

ausgeführt am

Max-Planck-Institut für Kernphysik

unter Betreuung von

Dr. Carsten Welsch

Max Planck Institut für Kernphysik

Department for Physics and Astronomy
University of Heidelberg

Diploma Thesis
in Physics
submitted by

Jan Egberts
born in Mülheim / Ruhr
2009

Investigations on transverse beam profile measurements with high dynamic range

The diploma thesis has been carried out by

Jan Egberts

at the

Max-Planck-Institute for Nuclear Physics

under the supervision of

Dr. Carsten Welsch

Max Planck Institute for Nuclear Physics

Abstract

A thorough understanding of halo formation and its possible control is highly desirable for essentially all particle accelerators. Particles outside the beam core are not only lost for further experiments, they are also likely to hit the drift chamber and thereby activate the beam pipe, which makes work on the accelerator costly and time consuming.

A well-established technique for transverse beam profile measurements is the observation of *synchrotron radiation*, *optical transition radiation* or the like.

A particular challenge, however, is the detection of particles in the tail regions of the beam distribution in close proximity of the very intense beam core. Results from laboratory measurements on two different devices are presented that might form the technical base of a future beam halo monitor: the novel SpectraCam XDR camera system which has an intrinsically high dynamic range due to its unique pixel design, and a flexible masking technique based on a *DMD micro mirror array* which allows for a fast mask generation to blank out the central core.

Zusammenfassung

Ein tiefgehendes Verständnis des Aufbaus und der möglichen Kontrolle von Strahlhalos ist sehr wünschenswert für nahezu alle Teilchenbeschleuniger. Teilchen außerhalb des Strahlkerns gehen im Normalfall nicht nur für weitere Experimente verloren, sondern treffen auch mit hoher Wahrscheinlichkeit auf die Driftkammer und aktivieren in Folge das Strahlrohr, was Arbeiten am Beschleuniger zeit- und kostenaufwendig macht.

Eine gängige Methode zur transversalen Strahlprofil-Messung basiert auf der Messung von *Synchrotronstrahlung*, *optischer Übergangsstrahlung* oder ähnlichem.

Eine besondere Herausforderung ist aber die Detektion von Teilchen im Halo-Bereich der Strahlverteilung in direkter Nähe zum sehr intensiven Strahl-Kern. Im Rahmen dieser Arbeit wurden Labormessungen an zwei verschiedenen Versuchsaufbauten durchgeführt, die eine Grundlage für einen zukünftigen Strahlhalomonitor bilden könnten: Das neuartige *SpactraCam XDR* Kamera System, das durch seine einzigartige Pixelarchitektur intrinsisch eine hohe dynamische Weite aufweist, und eine flexible Maskentechnik basierend auf einem *DMD Micro Mirror Array*, welches eine schnelle Maskengenerierung zu Ausblendung des zentralen Strahlkerns ermöglicht.

Contents

1 Introduction

Modern accelerators, like the Large Hadron Collider (*LHC*) [1, 2, 3], the International Linear Collider (*ILC*) [4, 5], or the Compact Linear Collider (*CLIC*) [6], are designed to provide highest luminosities. If there are many particles far off the beam axis, high current particle beams will suffer severe particle losses from collisions of beam particles with magnets, beam instrumentation, or the vacuum chamber. This leads to a decrease of the beam throughput and thus the number of events in the experiment for which the beam is used. At high energies another complication is that such collisions will cause activation of the vacuum chamber within a short time [7]. A contaminated beam pipe is not only hard to dispose after its use, but also requires careful and expensive measures for maintenance. The first step to minimise such losses is the measurement of those off-axis particles.

A well-established technique for transverse beam profile measurements is the monitoring of *synchrotron radiation (SR)* [8, 9] for high energy accelerators like the LHC, *optical transition radiation (OTR)* [10, 11, 12, 13, 14] at medium energies and currents, or the insertion of a phosphor screen [15, 16] at low energies. What applies for essentially all these light generation processes is that the light intensity is over a wide range proportional to the particle density, which makes the optical analysis of such light an ideal tool for beam profile measurements.

Due to the high particle density in the beam core the emitted SR or OTR light will be very intense in the centre of the profile. Since the beam halo is only sparsely populated, special techniques are required to measure the low intensity light of the beam halo without having the high intensity light from the beam core affecting the measurement. Measuring the halo with a low dynamic range camera will result in a saturation in the core region. The pixels will be overcharged and a so-called *blooming* will superimpose the halo signal.

It is the aim of this work to identify techniques to achieve highest dynamic ranges and to overcome the limitations of present beam profile monitors. This thesis is subdivided in three parts:

Firstly, a general introduction to accelerators is given and different mechanisms of beam halo formation are described. The properties of light generation processes suitable for beam diagnostics are then described.

Secondly, a CID-camera is presented and characterised by laboratory measurements. A CID-camera has an intrinsically high dynamic range due to its unique pixel design, which is described in further detail in section 5 of this work. According to literature, CID cameras are able to achieve dynamic ranges of up to $1{:}10^9$ [17]. This high dynamic range enables the camera to monitor the beam halo and the beam core simultaneously. For

the purpose of the here presented experimental studies Thermo Fisher Scientific kindly provided a model of the latest CID-camera, the "SpectraCam XDR".

In this thesis this camera was fully tested and its characteristics determined. For that purpose it was necessary to set up an experimental environment that realises a beam profile with a high dynamic range that the camera is capable of measuring.

Finally, a flexible core masking technique is presented. Measurements with fixed masks are often used for the observation of astronomical objects [18, 19]. However, in contrast to astronomical objects, the core of a particle beam is not of constant shape and varies with time. Initial experiments with fixed masks were already done at *CERN* [20] where the beam was adjusted to match a predefined mask. For time-dependant particle beams, a fixed mask will not suffice to blank out the beam core and thus a method is required to generate a mask on short time scales. In the frame of this thesis is was shown that this can be achieved by a *Micro-Mirror-Array (MMA)*. The concept of Micro-Mirror-Arrays is discussed in further detail in section 6.1 and results from measurements are shown.

2 Theoretical Background

In this section, the mechanisms that lead to beam halo formation are described. As the here presented monitor is based on the exploitation of light originating from the beam the concepts of SR, OTR, and luminescent screens are summarised.

2.1 Beam Profile

The beam profile gives the particle distribution within an accelerator beam. Since there are far too many particles in an accelerator to calculate the trajectory of each of them, a statistical approach is used. The trajectory of the ideal particle is called the *design orbit*. Particles on the design orbit move in the centre of the beam pipe and are therefore unaffected by *quadrupole* or *sextupole* magnets that are necessary to shape a beam of charged particles. The spatial coordinate and the momentum of such a design particle is used as the origin of the *phase space*. If all other particles are plotted in this *phase space diagram*, one can define a *phase space ellipse* which includes approximately 95% of the particles. In a linear approximation the particles perform harmomic oscillations along the design orbit. The phace space of a particle with fixed energy E is given as $kx^2 + p^2/m = 2E$, with k being a parameter of the restoring force and m being the mass. Since this is an ellipse equation, particles move on ellipse-shaped trajectories within the phase space, and the phase space ellipse itself is transformed along the accelerator path. Since the phase space in higher dimensions cannot be illustrated, *Poincaré sections* are used, in which the phase space is projected on only one spatial coordinate and its corresponding momentum[1].

The particle beam is modulated along the design orbit by *weak* or *strong focusing*. The weak focusing occurs within bending dipoles. As a simplification the *fringe fields* of the dipole magnet can be neglected, i.e. the magnetic field remains constant within the magnet and drops to zero outside. Assuming such a hard edge model of a 90° sector dipole and a *monochromatic* particle beam, i.e. without momentum spread, the *Lorentz force* will deflect all particles by 90° with the same bending radius. Therefore, all particles will leave the dipole at the same transverse position. The particle displacements still exist, but since the direction of flight has changed, the transverse displacements are transformed in longitudinal ones. The strong focusing principle is based on the combination of quadrupoles. Quadrupole magnets focus the beam horizontally and defocus the beam vertically, or vice versa. A combination of horizontally focusing magnets and horizontally defocusing magnets can be used to achieve a net focusing effect. It works analogously to the two dimensional *Paul trap*. *Liouville's theorem* states that the phase space volume of

[1] In accelerator physics, the angle is commonly used instead of the transverse momentum, e.g. $x' = \frac{p_r}{p_z}$

a system of non-interacting particles cannot be changed by any conservative force. Since quadrupoles generate a conservative field, the focusing increases the momentum spread, while reducing the transversal displacement. During the strong focusing the phase space ellipse rotates around the origin. The focusing strength of a quadrupole magnet depends on the transverse displacement which causes *betatron oscillations* of the particles perpendicular to the beam line. If the betatron frequency the so-called *tune* of the machine hits the beam cycle frequency in a ring, resonance effects occur that will blow up the beam. Based on these basic principles various accelerator and storage rings geometries can be developed. Even though the trajectories cannot be calculated at a single particle level, it is possible to determine an *envelope* of the particles within the phase space ellipse.

2.2 Accelerator Physics Notation

In accelerator physics, the origin of the coordinate system is conventionally placed on the design orbit with the x-axis in the horizontal and the y-axis in the vertical direction. In a storage ring, x is oriented along the radial direction, y upwards, and z points in the direction of motion of the particles. The path that the particle is moving on is denoted as s and is proportional to time for constant motion. Therefore, derivatives with respect to time are often replaced by spatial derivatives with respect to s. The *emittance* is a measure of the area of the phase space ellipse.

Due to the possibly very high energies within particle accelerators, one adopts the notation of the theory of special relativity, with p_x being the momentum in x-direction, E being the energy, $\beta = \frac{v}{c}$ and τ being the relativistic proper time. For statistical calculations, the *partition function* Z is used which is a measure for the number of micro states that the system can be in.

2.3 Beam Halo

There is no general definition of a *Beam Halo*. If particle beams travel propagate along an ideal accelerator, they will adopt Gaussian shaped profiles. Outside the main *core*, the real beam profile has nevertheless far broader shoulders than a Gaussian distribution. At the *Los Alamos Proton Storage Ring (PSR)* the demarcation between the Gaussian shaped beam core and the halo was reported to be clean and abrupt [21]. A beam profile measurement of the PSR is shown in Fig. 2.1. The solid blue curve is a Gaussian fit while the solid black curve is a fit based on the sum of two Gaussians. The demarcation between the core and the halo region is clearly visible [22].

From a geometrical perspective, it is therefore sensible to define the halo as the area that contains all particles outside the Gaussian shaped beam core. From the halo formation

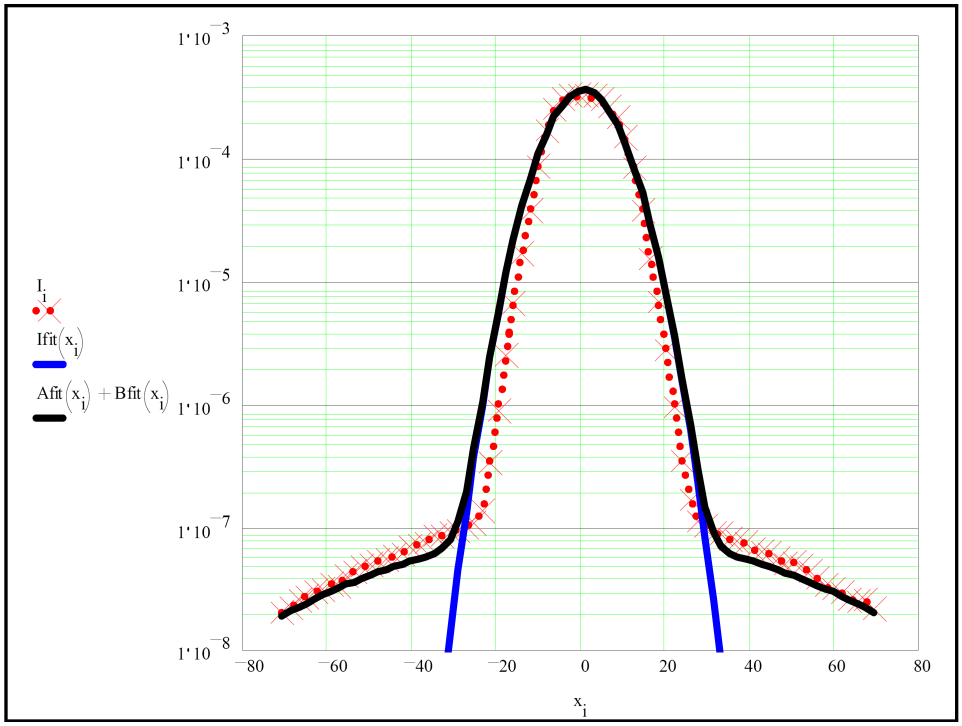

Figure 2.1: Beam halo measurement from the PSR in Los Alamos [22]

perspective on the other hand, it is reasonable to distinguish between the different halo formation mechanisms. From the diagnostic point of view, the main aspect of the halo is its low particle density in close proximity to the very dense beam core. An exact definition where the core ends and where the halo begins is therefore not possible. For diagnostic purposes, a high sensitivity as well as a high dynamic range is required for beam halo monitors. [23]

2.4 Mechanisms of Beam Halo Formation

An ideal accelerator model will lead to a perfect Gaussian shaped beam profile. In a real accelerator there are several effects that are not included in such a simple model, such as interactions of the beam particles among themselves or the residual gas, effects of non-ideal electro-magnetic fields, etc. Some of these effects will be described in this section.

2.4.1 Intrabeam Interactions

In this section, the interactions of particles with one another in a beam are described. Two cases have to be distinguished: Long-range and short-range interactions.

Since particles within the beam all have the same charge, electrostatic repulsion occurs.

This is called *space charge effect*. According to Turchetti [24], the long-range electrostatic repulsion between two particles in an accelerator does not act according to $F = -\frac{\alpha}{r^2}$ as it would in free space, but can be approximated by $F \propto -\frac{1}{r}$. In addition to these repulsive forces, the particles are refocused by the focusing quadrupoles. In the approximation of a constant focusing term, the focusing force is linear in the transverse coordinates. Both forces acting on the particles have a position dependency and are oppositely directed. The resulting oscillation can be described by the differential equation

$$m\ddot{x}_i + k_0 x_i = 2q^2 \sum_{j \neq i}^{N} \frac{x_i - x_j}{r_{ij}^2}. \tag{2.1}$$

In this equation, x_i is a transverse coordinate, k_0 the coefficient of the linear focusing force, N the number of particles with charge q, and r_{ij} is the distance between particle i and j. By combining the *space charge* forces on the right hand side of equation 2.1 to an effective potential $V^{(i)}$, one can form the *Hamiltonian* of the system:

$$H = \sum_{i=1}^{N} \left(\frac{p_{xi}^2 + p_{yi}^2}{2} + \omega^2 \frac{x_i^2 + y_i^2}{2} + \frac{\xi}{2} V^{(i)} \right) \quad . \tag{2.2}$$

The two parameters are given by $\omega = \frac{k_0}{mv^2}$ and $\xi = \frac{2Nq^2}{mv^2}$. Since the effective potential $V^{(i)}$ depends on the unknown positions (x_j, y_j) of all particles $j \neq i$, this problem can not be solved analytically. Nevertheless, it is possible to use a *mean field approximation* to generate a self-consistent solution. The self-consistent *Maxwell-Boltzmann (MB)* distribution is given by

$$\rho = Z^{-1} exp\left(-\frac{p_x^2 + p_y^2 + \omega_0^2(x^2 + y^2) + \xi V}{2k_B T} \right) \qquad [24], \tag{2.3}$$

with Z being the partition function, k_B the Bolzmann constant, and T being the temperature. The potential V and the frequency ω_0 can be calculated.

A result of a simulation is given in Fig. 2.2. The histogram corresponds to a simulation with $N = 10^3$ particles, the continuous lines to two different models, the *Kapchinskij-Vladimirskij (KV)* and MB model respectively. In the KV model, all particles are initially distributed uniformly within the beam centre and it is therefore the starting point for

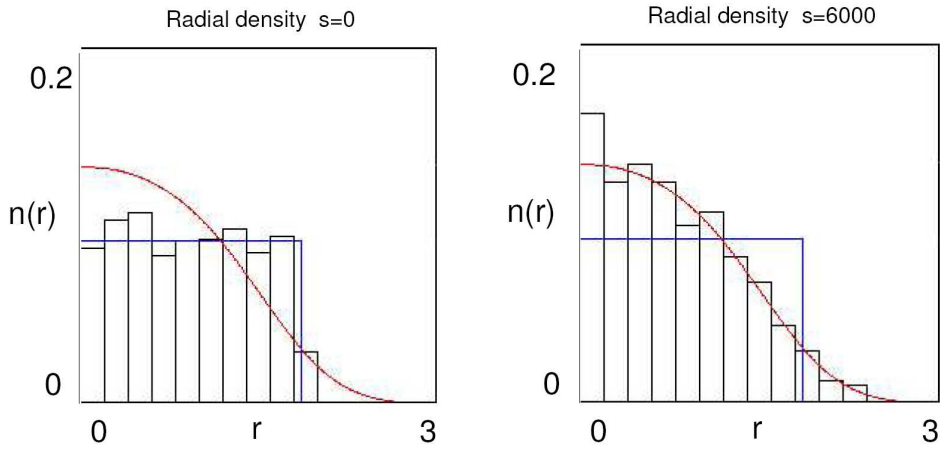

(a) simulation starts from KV-model

(b) after 6000 m simulation fits to MB-modell

Figure 2.2: Beam profile simulation with beam profiles according to the KV-modell (blue) and the MB-modell (red) [24]

this simulation of beam halo formation. The histogram in the left diagram refers to the simulation of the original KV distribution and the histogram in the right one to simulation of the profile after the beam travelled 6000 m [24].

The simulation proves that the long-range electromagnetic repulsion of the particles leads to no halo formation but can be compensated by the focusing. The resulting profile follows a Gaussian distribution.

However, at small distances scattering between two particles occurs. In this case they can be treated as two free particles interacting by the repulsive force $F = -\frac{\alpha}{r_{ij}^2}$. It can be shown [25] that the number of particles scattered per unit time into an emittance between ϵ and $\epsilon + \Delta\epsilon$ is given by

$$\frac{dN_\epsilon}{d\epsilon}d\epsilon = \iiint_{x,y,z} \iiint_{x',y',z'} \frac{dP'_\epsilon}{d\epsilon} d\epsilon f(x,y,z,x',y',z') dx dy dz dx' dy' dz'. \tag{2.4}$$

Here $f(x,y,z,x',y',z')$ is the distribution function of the beam and $\frac{dP'_\epsilon}{d\epsilon}d\epsilon$ is the probability per unit time for one particle at phase space position $(x,y,z,x',y'z')$ to scatter to an *x-emittance* between ϵ and $\epsilon + \Delta\epsilon$. The *x-emittance* is given by $\epsilon_x = (\frac{x}{x_0})^2 + (\frac{x'}{x'_0})^2$, with x_0 (x'_0) being the maximum values of x (x'). This probability can be derived from the differential cross section of *Coulomb scattering*. Numerical calculations have been done using the so called *water-bag* beam distribution [25] for different energies and equipartition conditions, defined by

$$f(x,y,z,x',y',z') = \begin{cases} f_0 & \text{if } (\frac{x}{x_0})^2 + (\frac{y}{y_0})^2 + (\frac{z}{z_0})^2 + (\frac{x'}{x'_0})^2 + (\frac{y'}{y'_0})^2 + (\frac{z'}{z'_0})^2 \leq 1 \\ 0 & \text{otherwise} \end{cases}.$$

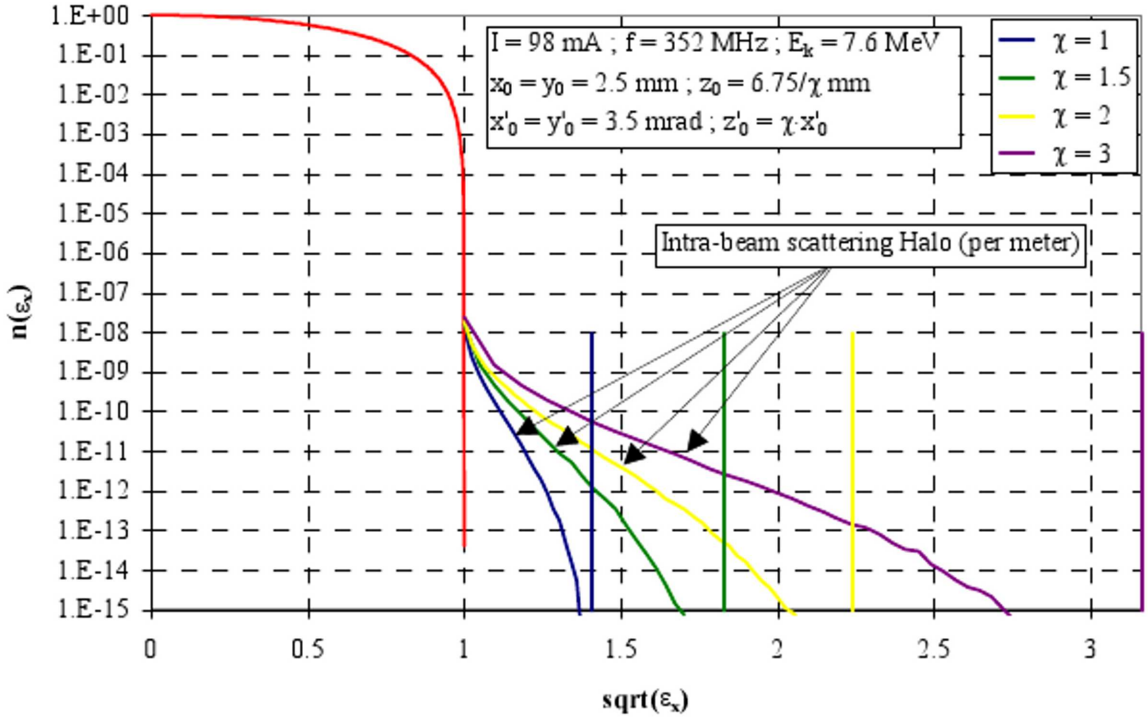

Figure 2.3: Beam Profile due to Scattering for different equipatition factors χ [25]

Assuming a symmetric beam profile in x and y, an *equipartition factor* can be defined as $\chi = \frac{z'_0}{r'_0}$ with $r'_0 = x'_0 = y'_0$. An equipartition factor of $\chi = 1$ corresponds to an equipartitioned beam. In Fig. 2.3 the halo creation per metre due to intrabeam scattering is listed for different equipartition factors. The vertical lines represent the maximum halo extent that can be reached theoretically. This maximum halo extent is due to the limitation of the energy transferred from one particle to another during a collision of two particles in a beam of given equipartition. Therefore, the extent of the halo increases with a higher equipartition factor, i.e. a higher longitudinal momentum compared to the transverse momentum [25].

2.4.2 Interactions with Residual Gas

In addition to these interactions between particles, also interactions with the residual gas occur. Since the beam particles are moving with a high velocity with respect to the residual gas, the interaction time is very short. Therefore, and since the residual gas atoms are uncharged, only collisions need to be taken into account. Due to the usually higher mass of the residual gas atoms, the lighter beam particle will be deflected during

collisions into outer accelerator orbits. If the new orbit is stable, the particle will populate the halo, otherwise it is lost. However, the beam particle can also scatter an electron out of the shell of the residual gas atom. Heavier beam particles will hardly be effected by these collisions, but the electron could be captured by the particle bunch and thereby reduce its internal space charge effect. It is nevertheless more problematic, if negatively charged ions are accelerated or stored. During collisions with the residual gas, the ions can lose one of their own electrons, and since they are no longer correctly charged, they get lost. Even though this effect does not contribute to the beam halo, it is a major source of particle losses in such machines. [26]

2.4.3 Interactions with the Accelerator

In circular accelerators and storage rings, all particles move along a circular accelerator path and perform an oscillation with a certain betatron frequency. Any errors within the accelerator will repeatedly distort the beam which can lead to a beam halo formation if the distortion is not sufficiently damped. Examples are misaligned dipole or quadrupole magnets. In high precision machines these devices are placed with an accuracy on the μm level [27].

Another problem that has to be taken care of during assembly and commissioning, is the mismatch of two different machine sections. Each accelerator has a certain *acceptance ellipse* in phase space that particles have to be in to be accelerated. Each particle at a certain position in phase space will move within the phase space ellipse according to the shape and orientation of the accelerator's phase space ellipse. In order to avoid widening of the phase space ellipse, and thereby increasing the emittance, the accelerator sections must match in a way that the beam emittance ellipse is similarly shaped and oriented as the acceptance ellipse[26].

2.4.4 Resonances

If the tune of the machine falls onto a resonance, the beam will continuously grow, leading to halo formation and most likely a beam loss. As an example a particle-core model by T. P. Wangler et al is described. The particle-core model predicts the halo that is formed from the resonant interaction between individual particles and a mismatch-induced core oscillation [28].

For the calculation a KV-distribution of the beam core is assumed, i.e. the beam core has a uniform particle density. For this special distribution Kapchinskij and Vladimirskij

have first calculated the so-called envelope equation [29]:

$$\frac{d^2R}{ds^2} + k_0^2 R - \frac{\epsilon^2}{R^3} + \frac{K}{R} = 0, \tag{2.5}$$

with R being the core radius, k_0 the focusing force, ϵ the total unnormalised emittance, and K a parameter depending on the charge, mass and axial velocity of the particles. In addition to the equation of motion for the core, the motion of a single particle is given by

$$\frac{d^2X}{ds^2} + k_0^2 X - F_{sc} = 0, \tag{2.6}$$

with X being the displacement and F_{sc} the space charge force for the homogeneous charge distribution of the KV-model, given by

$$F_{sc} = \begin{cases} KX/R^2, & |X| < R \\ K/X, & |X| \geq R \end{cases} . \tag{2.7}$$

The space charge force drops according to $F = \frac{\alpha}{r^2}$ outside the beam core and it increases linearly with the radius while the particle is inside the beam core since the effective amount of charge increases with R^3.

The two equations can be brought to a dimensionless form by introducing the new variables $r = \frac{R}{R_0}$, $x = \frac{X}{R_0}$ and $\tau = k_0 z$, with R_0 being the radius of the matched beam, given by $\frac{d^2R}{dz^2}|_{R=R_0} = 0$. A detailed derivation of the dimensionless equations is given in [28].

$$\frac{d^2r}{d\tau^2} + r - \frac{\eta^2}{r^3} + \frac{1-\eta^2}{r} = 0 \tag{2.8}$$

$$0 = \frac{d^2x}{d\tau^2} + x - (1-\eta^2) \times \begin{cases} x/r^2, & |x| < r \\ 1/x, & |x| \geq r \end{cases} . \tag{2.9}$$

The two equations only depend on the parameter $\eta = k/k_0$, with k being the wave number of a single particle. A second parameter μ is required to describe the mismatch of the beam. $\mu = r_{initial}$ is the is the initial core radius where the phase space ellipse is assumed to be upright, i.e. the beam has initially its smallest spatial extension.

The two differential equations can be solved numerically or used for Monte-Carlo simulations. Fig. 2.4(a) shows an example for a numerically solved solution with initial coordinates $x = 0.77$ and $x' = \frac{dx}{d\tau} = 0$ for $\mu = 0.62$ and $\eta = 0.5$. In the image the graphical meaning of the dimensionless variables and parameters becomes clear. The core oscillates around R_0 with an amplitude of $1 - \mu$ and the single particle oscillates with a frequency that is η-times lower than the core frequency. For the given parameters, the amplitude of the single particle oscillation is up to a factor of two higher than the core

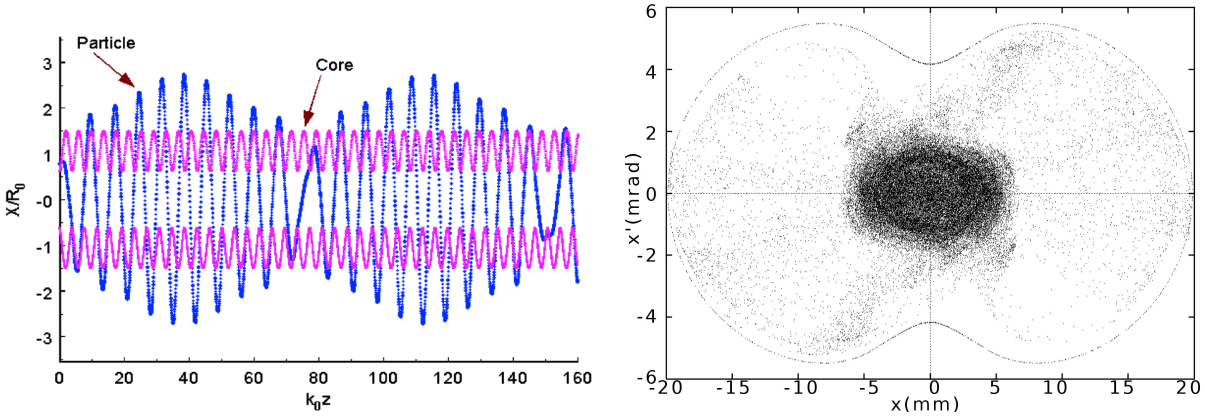

(a) Displacement versus time for a particle trajectory with initial coordinates $x = 0.77$ and $x' = 0$

(b) Beam phase space from a 2×10^6 particle simulation of an initial K-V distribution with a clear halo visible

Figure 2.4: Halo generation due to core - particle resonances with $\mu = 0.62$ and $\eta = 0.5$ [28]

oscillation which qualifies it as halo particle. Also the beat frequency is visible which indicates that particles oscillate between the core and the halo.

In Fig. 2.4(b) the result of a simulation with 2×10^6 particles is given in phase space. According to the common notation in accelerator physics, the divergence x' is denoted as an angle. The simulation started with a KV-distribution in accordance with the initial assumptions. Outside the central dense core region a broad peanut shaped halo is visible.

2.4.5 Conclusion

A real particle beam differs in many aspects form the ideal non-interacting many particle model. It was shown that the long-range electrostatic repulsion does not lead to halo formation but results in a Gaussian beam profile as long as no resonances are taken into account.

Nevertheless, short-range interactions, collisions with other beam particles, residual gas, or even thermal photons can scatter beam particles in the halo. Most of the discussed effects that scatter particles out of the central beam core can also be applied to halo particles. Therefore, halo particles have a certain probability to scatter back into the core. The beam particles are cycling between the core and the halo. This was particularly obvious in the Monte-Carlo simulation for core - particle resonances.

This collection of effects that lead to beam halo formation does not aim to be complete but rather to give an outline of processes leading to beam halo formation. The leading contributions vary for different accelerators and different operating conditions. Beam halo formation is a complex process which is not yet fully understood [30]. Halo formation and

transformation simulations are normally done at an accuracy of $10^{-3} - 10^{-4}$Additional research has to be done on theoretical simulations of beam halo formation as well as experimental measurements. For future beam halo measurements a halo monitor with high dynamic range is required to test theoretical simulations.

2.5 Light Creation

A central idea of the here presented work is that light emitted by beam particles shall be measured to determine the beam profile. The investigated instrumentation will thus be independent of the kind of the emitted light and is therefore applicable to accelerators of various types. Synchrotron radiation, optical transition radiation, or light emitted by a *phosphor screen* placed within the beam line are examples of light suitable for optical beam profile measurements.

2.5.1 Synchrotron Radiation (SR)

Synchrotron radiation (SR) is emitted when a charged particle is accelerated. This was at first considered an unpleasant effect since it limited the maximum achievable energy with the accelerator due to the energy loss resulting from SR. It also forced engineers to construct larger and larger lepton colliders like the *LEP* and it makes it virtually impossible to built TeV circular lepton accelerators [31]. However, synchrotron radiation has proven to be a unique tool for material research and spectroscopy. Today, electron storage rings are built with the single purpose of generating SR. The latest step towards next generation light sources, linear accelerators are constructed to serve as active elements in *free electron lasers* like the *FLASH* in Hamburg [32].

The energy loss S due to SR is given by

$$S = \frac{e^2 c}{6\pi\epsilon_0} \frac{1}{(m_0 c^2)^2} \left[\left(\frac{dp}{d\tau} \right)^2 - \frac{1}{c^2} \left(\frac{dE}{d\tau} \right)^2 \right] \qquad \text{[8]}. \tag{2.10}$$

If the acceleration is parallel to the velocity, the irradiated power is negligibly small. In case of a synchrotron, however, the centripetal acceleration keeps the charged particle on the circular orbit thereby causing the emittance of SR. Since the Lorentz force is perpendicular to the velocity it does not change the kinetic energy. The second term on the right hand side of equation 2.10 vanishes and in the limit of very high energies the equation becomes

$$S = \frac{e^2 c \gamma^2}{6\pi\epsilon_0 (m_0 c^2)^2} \left(\frac{dp}{dt} \right)^2 = \frac{e^2 c \gamma^4}{6\pi\epsilon_0 R^2} \tag{2.11}$$

using $\frac{dp}{dt} = p\omega = p\frac{c}{R}$, with R being the bending radius, and $E = pc$ for $\gamma \gg 1$ [9].

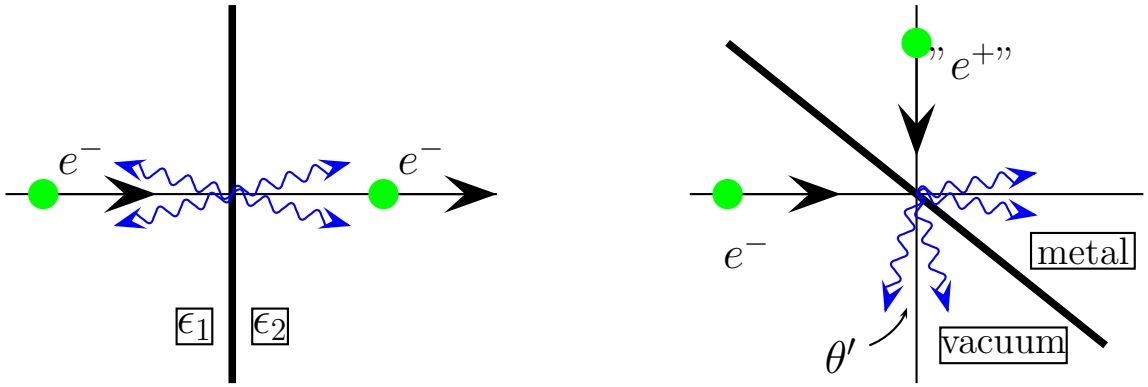

(a) Illustration of forward and backward radiation of OTR

(b) Illustration of OTR of an image charge "e^+" for 45° foil

Figure 2.5: Optical Transition radiation for a perpendicular and 45° metal foil [12]

In high energy storage rings, SR is a frequently used technique to monitor the beam profile since it provides an entirely non-perturbative way to monitor the beam profile. Because the emitted light intensity scales with γ^4 the light yield drops rapidly for low energy or heavy particle accelerators. Due to relativistic effects the light cone is boosted to the forward direction in a narrow angle which can be estimated to be $\theta \approx \frac{1}{\gamma}$ for $\gamma \gg 1$

The spectrum of synchrotron radiation is characterised by the critical frequency $\omega_c = \frac{3c\gamma^3}{\rho}$, with ρ being the bending radius. The emission of SR at frequencies higher than ω_c drops fast. Since the critical frequency scales with the third power of the relativistic γ the wavelength of SR is shifted to the infrared or even lower for energies below about 270 GeV. It is possible to take advantage of the edge emission which will increase ω_c by observing SR emitted in dipole fringe fields but beam diagnostics based on SR is nevertheless, only possible for high γ machines.

2.5.2 Optical Transition Radiation (OTR)

Optical Transition Radiation (OTR) was first predicted by Ginzburg and Frank in 1945 [10]. The great potential of OTR for beam diagnostics was then demonstrated in 1975 by Wartski [11]. OTR is emitted when charged particles cross the boundary between two media with different dielectric constants. This effect can be understood by considering that the electric field of the particle depends on the dielectric constant ϵ of the medium. When entering a medium with different dielectric constant, the electric field of the particle has to rearrange. During this process a fraction of the field may be "shaken off" as transition radiation. The light is radiated in forward and backward direction, as it is illustrated in Fig. 2.5(a).

If a charged particle moves from a medium of dielectric constant ϵ to vacuum, the emitted

OTR intensity in the forward direction is given by [12, 13]

$$\frac{d^2U}{d\omega d\Omega} = \frac{e^2\beta^2}{\pi^2\epsilon_0 c}\frac{\cos^2\theta\sin^2\theta}{(1-\beta^2\cos^2\theta)^2}\left|\frac{(\epsilon-1)(1-\beta^2-\beta\sqrt{\epsilon-\sin^2\theta})}{(\epsilon\cos\theta+\sqrt{\epsilon-\sin^2\theta})(1-\beta\sqrt{\epsilon-\sin^2\theta})}\right|^2 . \quad (2.12)$$

For relativistic particles with $\beta \approx 1$, and with $|\epsilon| \gg 1$ the right hand term approches unity. Because metals have a dielectric constant in the optical frequency range of about $\epsilon = -100$, this is a good approximation for metal foils. Since optical transition radiation has an opening angle of about $\theta \approx 1/\gamma$ for $\gamma \gg 1$, equation 2.12 can be simplified for small angles.

$$\frac{d^2U}{d\omega d\Omega} = \frac{e^2\beta^2}{4\pi^2\epsilon_0 c}\frac{\sin^2\theta}{(1-\beta^2\cos^2\theta)^2} = \frac{e^2}{\pi^2\epsilon_0 c}\frac{\theta^2}{(\theta^2+\gamma^{-2})^2} \qquad [12]. \quad (2.13)$$

Calculations based on equation 2.13 of the light intensity integrated over total solid angle as a function of γ and the angular distribution based on equation 2.12 of the OTR emitted by particles with $\gamma = 1.02$ as it is the case for the *University of Maryland Electron Ring (UMER)* is presented in Fig. 2.6.

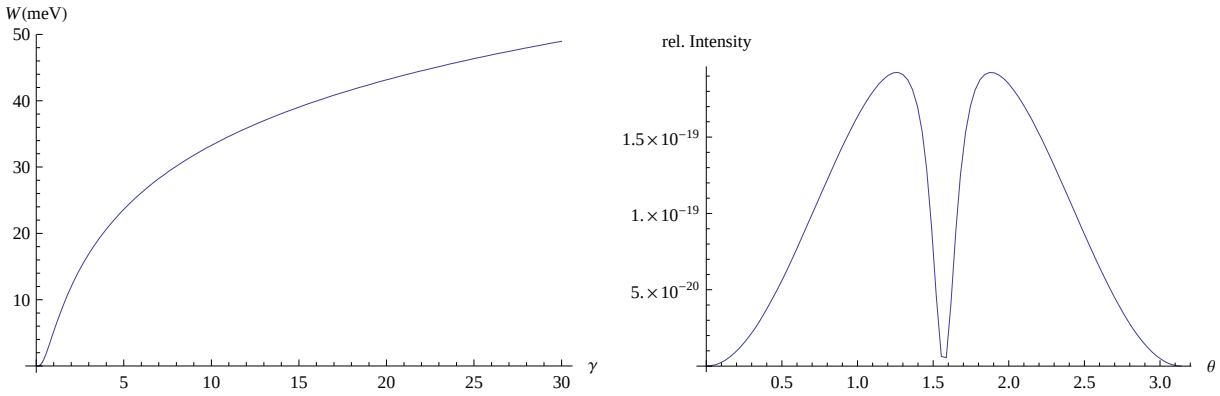

(a) Total energy loss due to OTR in the visible range at a single foil

(b) Angular distribution of OTR for γ=1.02

Figure 2.6: Optical Transition Radiation Characteristics for

The integration of equation 2.13 over the solid angle $d\Omega = \sin\theta d\theta d\phi$ from $\theta = 0$ to $\theta = \theta_{max}$ gives the energy dependence of the spectral intensity. The results can be simplified for very small and large angles θ_{max}:

$$\theta_{max} \ll 1/\gamma : \frac{dI}{d\omega} = \frac{e^2}{2\pi\epsilon_0 c}(\gamma\theta_{max})^4 \quad (2.14)$$

$$\theta_{max} \approx 1 \gg 1/\gamma : \frac{dI}{d\omega} = \frac{e^2}{\pi\epsilon_0 c}\left[2\ln(\gamma\theta_{max}) - 1\right]. \quad (2.15)$$

From equations 2.14 and 2.15 it can be deduced that the intensity of OTR light emitted

into very narrow angles increases with γ^4, while the total intensity has a logarithmic dependency, compare Fig. 2.6.

A very interesting feature for experiments is the backward radiated OTR. It can be deployed by inserting a metal foil into the beam at a 45° angle. In analogy to optical reflection, the backward component of the OTR will be emitted perpendicular to the beam axis. This can be interpreted as the OTR emitted by the image charge within the metal foil. The energy of the OTR is then given by [12]

$$\frac{d^2U}{d\omega d\Omega} = \frac{e^2}{4\pi^2\epsilon_0 c}\left|\frac{-\sin\theta}{1-\beta\cos\theta} + \frac{\sin\theta'}{1-\beta\cos\theta'}\right|^2 \quad , \tag{2.16}$$

where θ' is the angle of the emitted light with respect to the trajectory of the image charge. The perpendicular emission of the OTR allows an easy way of measuring the beam profile outside the vacuum chamber.

In contrast to synchrotron radiation, a foil has to be introduced to the beam axis which will negatively affect the beam. OTR decreases the beam energy only by a few eV, but during collisions of the beam particles with foil atoms, they emit *bremsstrahlung* which causes an energy loss of

$$\frac{dE}{dx} = -\frac{E}{X_0} \tag{2.17}$$

with X_0 being the *radiation length*, a constant which depends on the foil material. For metals, it ranges between 0.3 cm and 10 cm. Thereby, the energy loss can easily exceed a few keV per μm. At low momentum, ionization or excitation of atoms within the foil will also contribute to the total energy loss. This is described by the *Bethe-Bloch formula*.

But the energy loss is not as problematic as the increase of the beam divergence which can lead to beam instabilities. Even though the average momentum of the particles is not changed when the particles pass through the foil, the variance of the momentum increases due to Coulomb scattering. The initial divergence θ_0 will be increased according to

$$\theta^2 = \theta_0^2 + \theta_{scat}^2 \qquad [12] \tag{2.18}$$

where θ_{scat} is the increase of the divergence due to Coulomb scattering. It can be calculated to be

$$\theta_{scat} = \frac{21}{\sqrt{2}\beta pc}\sqrt{\frac{s}{X_0}} \qquad [12] \tag{2.19}$$

where s is the path length through the foil and pc is given in MeV. Values for foils of different material and energies are listed in table 2.1. For low energy particle beams with a divergence of a few mrad, OTR is no longer a non-perturbative measurement technique. For high energy particle beams however, the increase of divergence becomes negligible.

θ_{scat}/mrad	Aluminium	Titanium	Silver	Gold
4.5 MeV	11.1	17.4	36.2	59.3
20 MeV	2.5	3.9	8.1	13.3

Table 2.1: Angular divergence due to Coulomb scattering for 1μm foil [12]

High intensity particle beams can also damage the foil itself, which will limit its life time and will also affect the beam quality. Released ions could either focus the beam even further which would cause an increased damage, or they could blow up the beam. The effects of high electron currents passing through thin foils have been analysed at the *CLIC Test Facility 3 (CTF3)* [33].

For sufficiently thin foils ($\sim$ tens of microns), the *bremsstrahlung* is not re-absorbed by the radiator and can therefore be neglected for the calculation of the energy deposition in the foil. For high energy particles, it represents a large fraction of the lost energy. The total energy deposition in the foil causes a temperature increase as long as the energy deposition is larger than the energy loss which is mainly due to heat exchange. For high current beams, the foil is therefore preferably made of a material of high thermal conductivity which allows for faster cooling. Further material characteristics of interest are a high fusion temperature and a high specific heat. Based on these characteristics, Beryllium and Carbon are good candidates for OTR-foils at CTF3. A graphite target was able to withstand the total thermal load of a 20 MeV electron beam of 3.5 A average current focused down to σ =250 μm while heating up to 2250 °C [33]. The ideal material for a specific OTR monitor depends on the characteristics of the accelerator and no general solution exists.

The intensity of the *black body radiation* emitted at these temperatures is comparable to OTR which makes the OTR detection challenging. But since the black body radiation emits light in a different spectral range, the OTR can be isolated by a blue filter.

2.5.3 Phosphor Screen

The light emitted from a *phosphor screen* differs fundamentally from SR or OTR. In the latter, the light is generated by the accelerated particle itself, while in the case of a phosphor screen, the beam particles induce light emission from the screen atoms.

For low-energy machines such as the UMER [34] or the *Ultra-low energy Storage Ring (USR)* [35] Phosphor screens are often times the only possible way to generate enough light for beam profile measurements.

As already discussed for OTR, when charged particles pass through a foil, they can ionize or excite atoms within the foil. In phosphor screens the excitation of the atoms is maximised in such a way that the atoms will emit light in the visible range during the de-excitation process. The spectral intensity and the angular distribution of the emitted light therefore only depends on the properties of the foil. The time resolution of any monitor based on a phosphor screen is limited by the finite life time of the excited states of the atoms. The decay time of common phosphor screens are in the order of μs, but can also go down to the ns-regime [16].

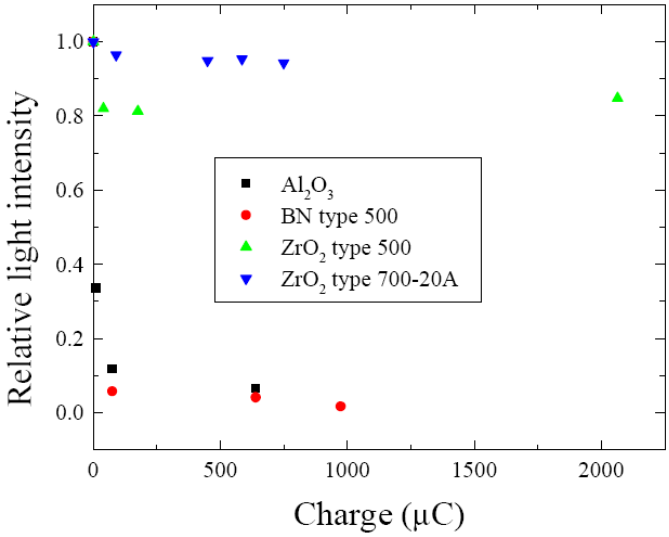

Figure 2.7: Luminescence yield of the different material as a function of the integrated beam charge [15]

As for OTR, the deposited heat on the foil may cause tremendous problems. An additional problem may occur since most scintillating screens are insulators and can therefore not easily be discharged. At CERN, three different scintillating materials have been tested for phosphor screens. Their material characteristics are given in table 2.2. The yielded *luminescence* as a function of the integrated beam charge is given in Fig. 2.7 for all three materials. The screens turn dark brown after approximately 24 hours of radiation.

Material	c_p(J/gK)	k(W/mK) at 100°C	T_{max}(°C)	ρ(Ωcm) at 400°C
Al_2O_3	0.9	30	1600	10^{12}
ZrO_2	6	2	1200	10^4
BN	2	35	2400	10^9

Table 2.2: Material characteristics of three different scintillating materials tested at CERN [15]

2.5.4 Conclusion

Since particle beams emit SR without including any objects in the beam line, it is the preferred way for non-destructive optical beam diagnostics. To increase the quality and intensity of the SR, one can also include an undulator or a wiggler in the beam line. Due to the narrow opening angle of SR of $\theta = 1/\gamma$ for high energies, the emitted light beam will have the same profile as the particle beam which reduces the need of further optical elements. Nevertheless, due to its γ^4 power and its γ^3 frequency dependence, the light

intensity will drop very fast for low energy or heavy particles. In addition, it is limited to circular accelerators and storage rings.

As the OTR light intensity increases according to a logarithmic law, it is advantageous to use OTR for low energy particles. It has a similar angular distribution as SR and has the advantage of light emission perpendicular to the beam line. But since a foil has to be included into the beam line to generate OTR, a beam profile monitor based on OTR will increase the *divergence* of the beam. This is less problematic for linear accelerators because the particles pass trough the foil only once.

For energy ranges, in which not even OTR will provide a high enough light intensity, phosphor screens are used. A phosphor screen will emit light as long as the beam is able to excite the atoms within the foil. Since the spontaneous emission of light is homogeneously distributed in all directions, only a small fraction of the light can be effectively monitored.

3 State of the Art

A variety of different monitors are presently used for measuring the beam profile in an accelerator or storage ring: Among the most common monitors are wire scanners that measure secondary electron emissions. Different layouts have been successfully used, including a single fixed or moving wire, a grid of wires, or even a laser beam as a replacement of the wire. Ionisation beam profile monitors are based on the ionisation of the residual gas by a beam particle. After the ionisation electrons and ions are bent towards electrodes where their signal is measured. Finally, optical methods can be employed where SR, OTR, and Phosphor screens are the most commonly used ones.

3.1 Commonly used Beam Profile Monitors

There are several different types of beam profile monitors. The monitors can be roughly categorised: wire scanners work by measuring of secondary electron emissions. This can be done by a single wire, a grid of wires, or even by a laser beam. Ionisation beam profile monitors work based on the ionisation of the residual gas by a beam particle. After the ionisation electron and ion migrate towards electrodes where the signal is measured. And as a third category optical methods can be employed. SR, OTR-screens, or phosphor-screens can be used for light generation.

Wire scanners have been used for measuring beam profiles successfully for a long time. They allow for a direct way of measuring the beam profile with high accuracy. For the *Los Alamos Proton Storage Ring (PSR)* a wire scanner with 100 μm SiC wires was developed which led to a dynamic range of up to 10^6. The emphasis was put on noise reduction for this device to achieve those high dynamic range [21].

The Los Alamos *Low Energy Demonstration Accelerator (LEDA)* uses another wire scanner with 33 μm carbon wires for the core and a scraper for the tail measurement. The scrapers consist of a 1.5 mm thick carbon mounted on a water cooled 1.5 mm thick copper plate. The wire is cooled by thermal radiation only which suffices to keep the temperature below 1800 K where thermionic emission starts. With this combined setting the beam profile monitor achieved a dynamic range of 10^5. In this particular case considerable challenge was the optimisation of the bias voltages for wires and scraper [21, 36].

Laser wire scanners are currently under development that have the advantage that they permit measurements at full beam power without the risk of damaging the diagnostic device as compared to solid wire scanners. Proof of principle for a laser wire scanner was demonstrated for the *Spallation Neutron Source (SNS)* linac. Short laser pulses from a Nd-YAG laser were used to strip H^- ions. By measuring the stripped electron the laser wire scanner achieved a dynamic range of 10^4 [21].

Another limitation of wire scanners are potential distortions of the beam if too much wire material is interacting with the beam. To overcome this limitation and to minimise losses the so-called flying wire scanner was developed. A flying wire beam profile monitor was set up at the 12 GeV KEK Proton Synchrotron. A 7 μm thick carbon wire rotates with high speed and crosses the beam line each time to scan the beam profile. The dynamic range of this monitor was demonstrated to be larger than two orders of magnitude [21, 37].

As already discussed in section 2.5, light emitted by the beam particles are a common tool for beam profile measurements also. The techniques for beam profile measurements presented in this thesis are based on the observation of SR, OTR, or light emitted by a phosphor screen. Beam profile measurements from the phosphor screens in UMER will now be described to highlight the limitations of current beam profile monitors.

3.2 University of Maryland Electron Ring

The UMER is an electron storage ring designed for measurements on space charge dominated beams. The *intensity parameter* χ is commonly defined as the ratio between the space charge force and the external force. $\chi = \frac{K}{k_0^2 a^2}$, with k_0 and K as defined in equation 2.5 as spring constant of the external force and measure of the space charge respectively, and with the beam radius a. $0 \leq \chi \leq 1$ must be fulfilled for a stable operation. For $\chi \geq 0.5$ the beam is considered to be space charge dominated and its dynamics will be governed by plasma oscillations instead of betatron oscillations [23].

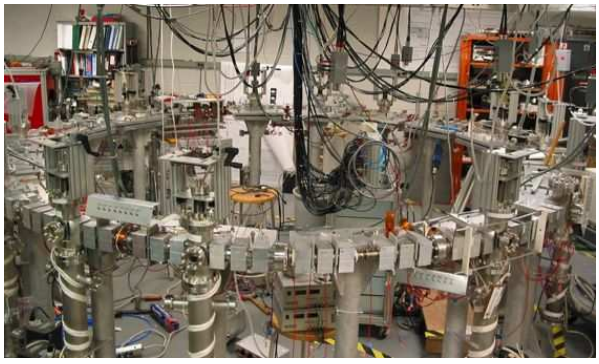

(a) Photo of the whole ring [38]

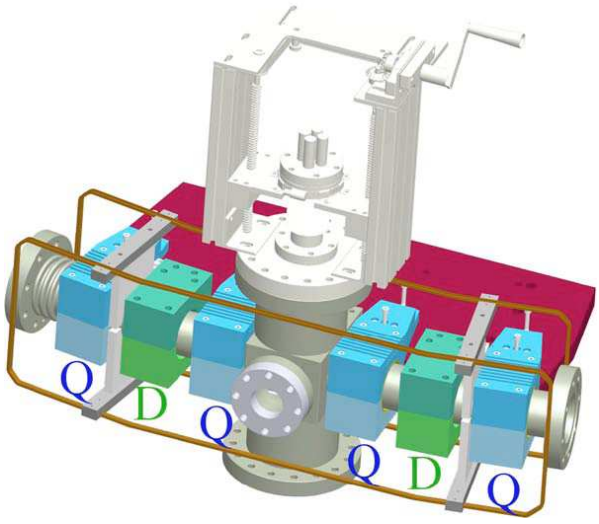

(b) design drawing of a single 20° section consisting of four quadrupole and two dipole magnets and one observation chamber used for profile measurements [39]

Figure 3.1: Images of the University of Maryland Electron Ring

The UMER was commissioned in 2001 as a low energy and high current storage ring. The ring is designed for 10 keV electrons and beam currents between 0.6 and 100 mA. The residual gas pressure is of the order of 10^{-10} mbar. It consists of a total number of eighteen 20° sections subdivided in two lattice periods of 32 cm length respectively. A design drawing of a single section consisting of two quadrupole and one dipole magnet on each side of an observation ring chamber is shown in Fig. 3.1(b) The ring has a total circumference of 11.5 m and a radius of 1.83 m. A photo of the UMER storage ring is shown in Fig. 3.1(a). On the left hand side the particles are injected and travel clockwise around the ring.

The electron beam itself has a normalized emittance of $\leq$ 3.0 mm·μrad and a beam diameter of $\leq$ 10 mm. The electron gun is equipped with various different apertures which allows for the generation of different beam profiles like a circular profile with reduced diameter or a pepper pot profile. The cathode can be operated at thermal or photo-emission mode which allows for a spatially or temporally modified current.

For diagnostic purposes beam position monitors (BPM) are mounted in the ring chambers with a spatial resolution of 0.1 mm and a temporal resolution of 2 ns [39]. Underneath each BPM a phosphor screen is mounted for beam profile measurements. The phosphor screen can be inserted in the beam line by an actuator. The light emitted by those screens can be monitored by 8 bit, 12 bit, and 16 bit cameras.

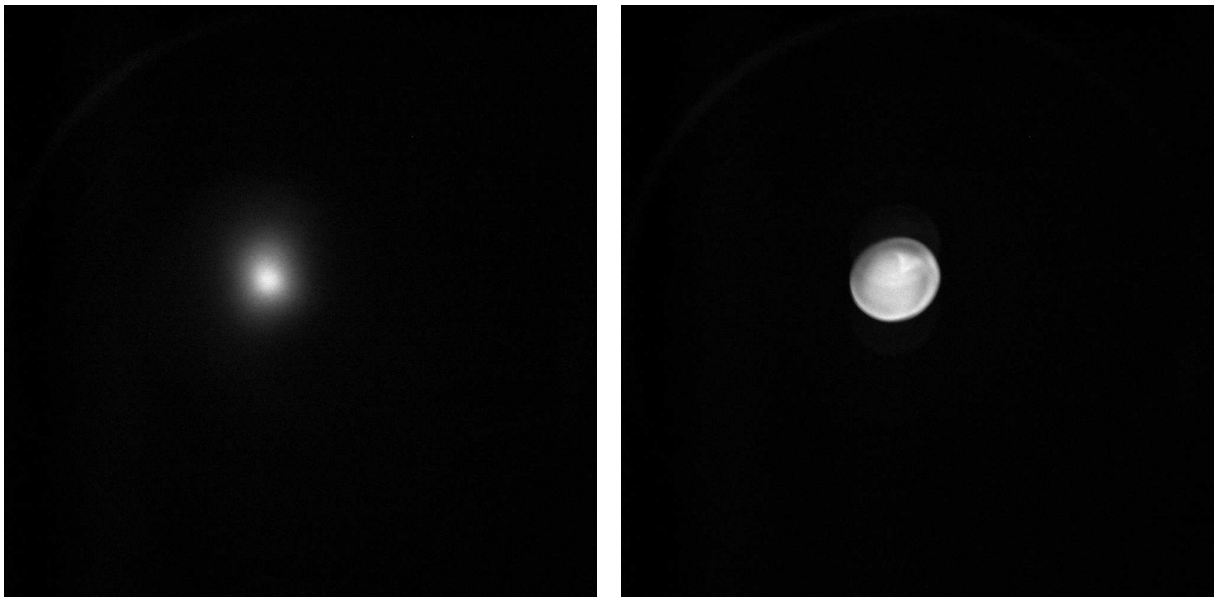

(a) Gaussian beam profile [40] (b) Rectangular beam profile [40]

Figure 3.2: Beam profiles of the University of Maryland Electron Ring

3.3 Analysis of UMER Beam Profile Measurements

The electron gun of the UMER can generate beam profiles of various shapes. Here, a Gaussian shaped beam and a rectangular beam profile are analysed. For profile measurements, a CCD-camera from Princeton Instruments was used, the PI-MAX2. It is a gated micro channel plate intensified CCD camera which cooled down to -20°C to decrease the read noise. With a full well capacity of 450,000 e^- the camera is able to achieve a dynamic range of 16 bit [41]. Due to its high range of exposure times varying from a few ns up to several hours, the camera was used to measure the beam halo down to very low intensities.

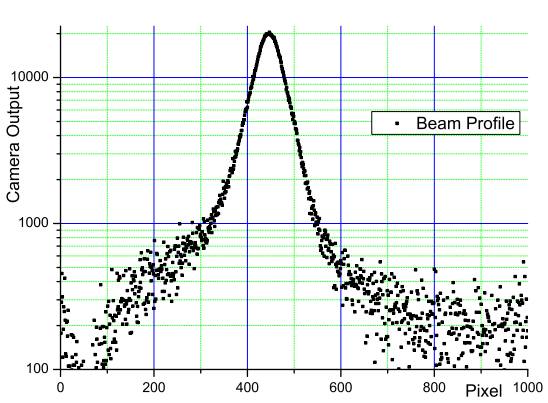

(a) Gaussian beam profile projected over 10 pixel rows [40]

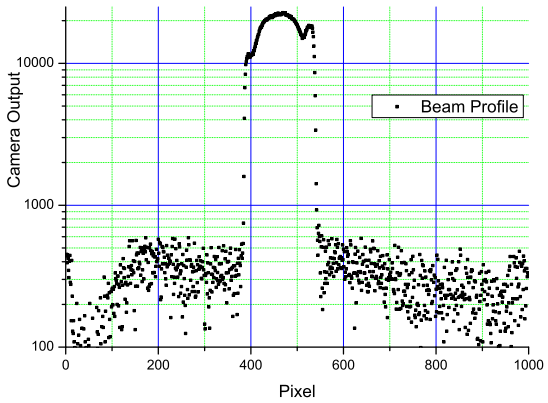

(b) Rectangular beam profile projected over 10 pixel rows [40]

Figure 3.3: Projected beam profiles of the UMER

Images of two different beam profiles are shown in Fig. 3.2. These images are converted into a text file containing a two dimensional array of 16 bit integer values for a quantitative analysis. The two dimensional profile is then projected over 10 pixel rows to achieve the one dimensional profiles shown in Fig. 3.3. Apart from the core a strong background is visible.

For both profiles the standard deviation of the background was calculated to be around 160. With a maximum count rate of a 16 bit camera of $2^{16} = 65536$, the dynamic range is DR=65536/160≈400.

For beam halo measurements this dynamic range does not suffice, but a higher dynamic range is required to measure the halo and compare the results to theoretical calculations. Simulations can be evaluated when measured beam profiles with a dynamic range of $\geq 10^4$ are available. Ideally such a monitor will be able to operate with any kind of light generated by beam of charged particles, such as SR, OTR, or light emitted by a phosphor screen.

4 Experimental Equipment

Halo measurements in an accelerator are often difficult to realise. The limited experimental space, available beam times, or high levels of radiations complicate tests of prototypes. For this reason an offline experimental zone was built up in the frame of this thesis and is described in this section.

4.1 Test Stand

All experiments were set up on an aluminium breadboard, 800 mm long and 600 mm wide. The board has M6 holes arranged in a regular 25 mm grid. Upon the breadboard, a box was installed to shield the ambient light. The box was built using *Item Building Kit* elements. Four bars were mounted on the breadboard in a rectangular shape to serve as a basis for the box. Another eight bars were attached to provide a cuboid frame. At each face of the cuboid, a 1.5 mm thick aluminium plate was mounted in each corner. At the edges of the aluminium plates foamed plastics were glued on to enhance the contact between the bars and the plate and to minimise the ambient light in the box.

In order to estimate the efficiency of the black box, the background light was measured. Therefore, the CID-camera, described in detail in section 5, is installed in the box and operated in the second pre-exposure mode which grants the highest light sensitivity. A measurement was done with the room fully illuminated (Fig. 4.2(a)), and as a comparison, a second measurement with all lights switched off and a closed objective lens mounted on the camera to measure the readout noise (Fig 4.2(b)). In Fig. 4.1, the average count rate per second (cps) in the horizontal direction of both measurements is displayed. It is clearly visible that the main light pollution is from the right hand side where the door of the box is located which cannot be fully sealed. Nevertheless, it can be noticed that the average count rate is about 1.4 cps only and thus close to the noise background of the camera of 1.1 cps.

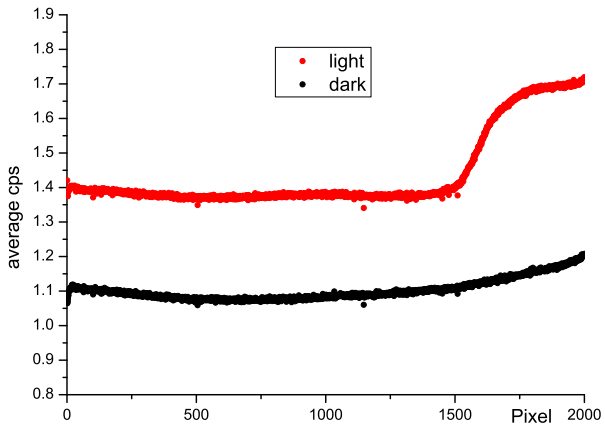

Figure 4.1: Average background for fully illuminated and totally dark room

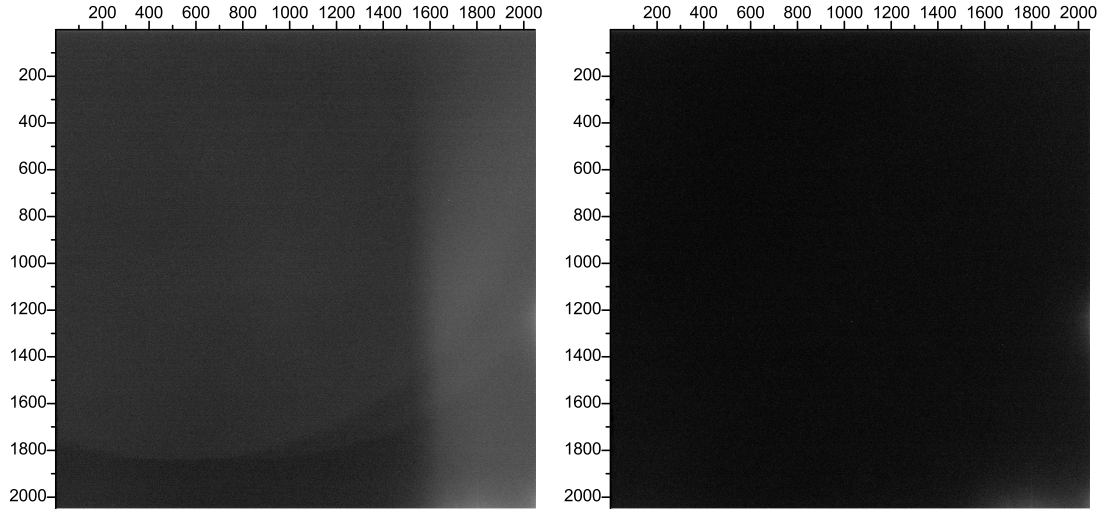

(a) Image in illuminated room (b) Image in dark room

Figure 4.2: Background measurement in the black box where the grey scale in a logarithmically

4.2 Laser

For reasons discussed in section 2, SR and OTR are often the method of choice for beam profile measurements. In the experiment a He-Ne laser is used to simulate SR or OTR. With an opening angle of 1.41 mrad, it has an angular distribution comparable to SR or OTR of an electron beam of a few hundred MeV. Since a laser and a particle beam have both a similar profile with a very dense Gaussian shaped core, a laser beam is a good approximation to SR or OTR emitted by a particle beam.

In contrast to the laser, which has a single wavelength of 633 nm, SR or OTR have continuous spectral distributions. An additional difference between laser light and SR or OTR light is the laser light's coherency, which will cause unwanted interference patterns during the experiment.

Unlike light emitted by an accelerator beam, an ideal laser will have no halo but is purely Gaussian shaped. This makes laser light a good tool for high dynamic range measurements.

In the here presented setup, a continuous laser is used with an output power of 0.5 mW. The laser grants the advantage of being a cheap and easily manageable light source. The light intensity of the laser is sufficiently high to observe the halo and can easily be reduced by neutral density filters. Using a laser simulating OTR or SR, it is possible to set up a test stand where optical methods for beam halo monitoring can be investigated.

4.3 Neutral Density Filters

In order to adjust the laser light intensity or to calibrate instruments, neutral density filters are frequently used during the experiment. A total number of 10 neutral density filters from Thorlabs GmbH [42] are used during the experiment. Their optical density ranges from 0.1 to 4.0 which corresponds to transmissions ranging from $10^{-0.1} = 0.79$ to $10^{-4} = 0.0001$ for a light wavelength of 633 nm, which is exactly the wavelength of the laser in use. The transmission is strongly wavelength dependant, in particular the high optical density filters. The transmission of different neutral density filters as a function of the wavelength is shown in Fig. 4.3, with NE10, NE20, or NE30 indicating a level 1, level 2, or level 3 density filter. For wavelengths above 700 nm, the transmission of the high level filters differ by an entire order of magnitude from their design value.

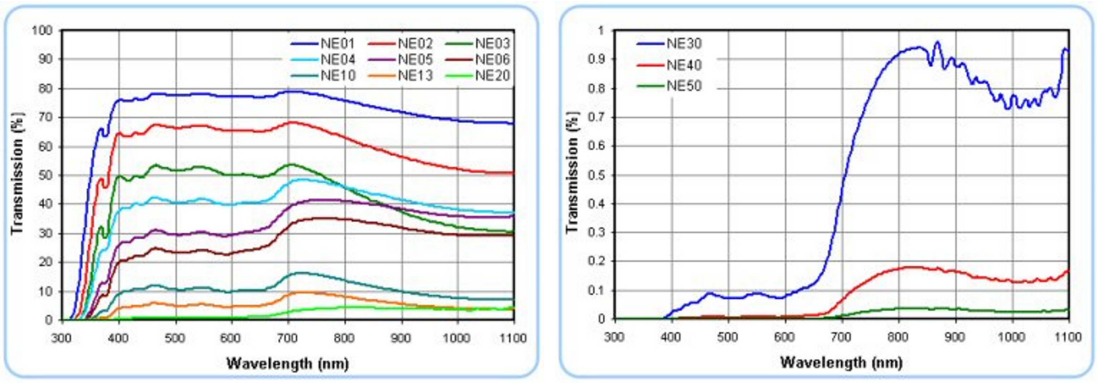

Figure 4.3: Wavelength dependency of the neutral density filters transmission [42]

The transmission errors and the material that they are made of are given in table 4.1. Due to exponential weighting of the errors, they are far larger than they appear. An exponential error of 0.2 corresponds to a relative uncertainty of about 50%.

Optical Density	0.1	0.2	0.3	0.4	0.5	0.6	1.0	2.0	3.0	4.0
Error	±0.01	±0.01	±0.01	±0.02	±0.03	±0.04	±0.06	±0.1	±0.15	±0.2
Substrate	NG11	NG11	NG11	NG11	NG4	NG4	NG4	NG9	NG9	NG9

Table 4.1: Neutral density filter information [42]

4.4 Homogeneous Light Source

In addition to the laser, a homogeneous light source was used for the camera calibration. The homogeneous light source consists of two parts: a fibre optics illuminator and a backlight. The fibre optics illuminator sends high intensity light into a light guide that delivers it to the backlight where it is transformed into a uniform light distribution.

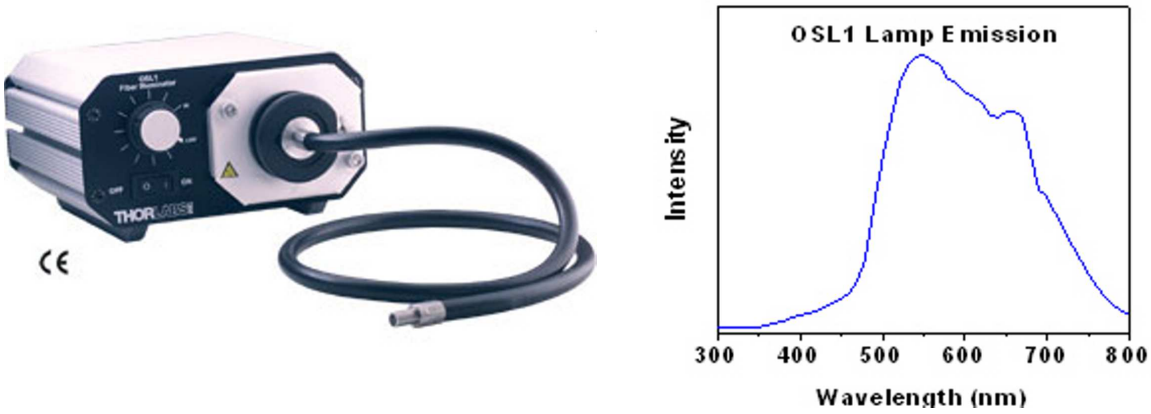

(a) Picture of the OSL1-EC [42] (b) Spectral distribution of the OSL1-EC [42]

Figure 4.4: Fiber illuminator OSL1-EC

An OSL-1EC is used as fibre optics illuminator, see Fig. 4.4(a). It is a halogen light source with a maximum power output of 150 W. The output can be adjusted in the range of 1000:1 and the colour temperature is 3200 K [42]. The spectral distribution is given in Fig. 4.4(b)

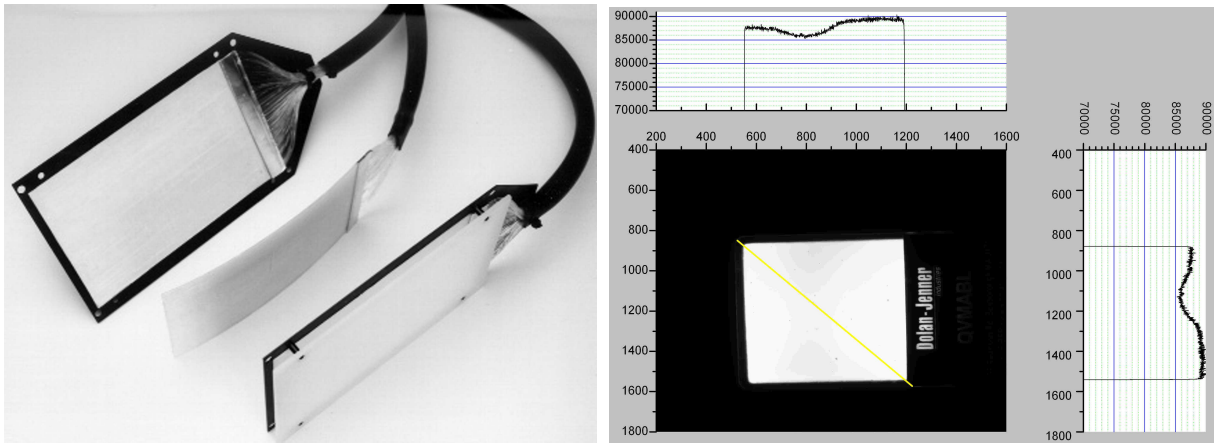

(a) Assembly of the backlight [43] (b) Light distribution measurement of the backlight

Figure 4.5: Backlight for the creation of uniform light

A 5cm×5cm sized backlight of Dolan-Jenner is used to generate a homogeneous light distribution. The assembly is shown in Fig. 4.5(a). The fibres of the light guide are slitted up and laid next to one another. Thereby, the backlight grants a very homogeneous light distribution with a uniformity of better than 95%. The results of the measurement are presented in Fig. 4.5(b). The light distribution varies by ∼3000 cps with a maximum intensity of 89000 cps which corresponds to a fluctuation of 3.4%.

4.5 Objective Lens

For laser beam profile measurements, no objective lens is required since the laser light is already highly focused. But for measurements like the image acquisition of the homogeneous light source, discussed in section 4.4, an objective lens is required to refocus the light on the pixel array.

The 'Sigma 18-50 mm 3.5-5.6 DC AF Nikon' is used as objective lens for the CID-camera described separately in section 5. The main feature of this objective lens is its small focal length of 25 cm and the Nikon F bayonette mount required for the attachment to the CID-camera shutter system. Further characteristic data of the objective lens is a magnification of up to 1:3.5 and a field viewing angle ranging between 69.3° and 27.9°.

4.6 CCD-Camera

For the core masking technique described in section 6 a CCD camera type UI-1540-M of "Imaging Development GmbH" [44] was used in combination with an MMA which is discussed separately in section 6.1. It is a monochrom camera with a resolution of 1280×1024 pixel. With a pixel size of 5.2 μm, this results in a chip size of 6.66 mm×5.32 mm. At highest resolution, the camera achieves a frame rate of 25 frames per second (fps) which can be boosted up to 219 fps by reducing the resolution down to 320×256. The exposure times may vary between 35 μs and 980 ms, which allows for an application in a wide range of light intensities.

4.7 Spatial Mode Filter

Since the assumption that a laser is Gaussian shaped over a sufficient range was found to be invalid, a *spatial mode filter* was inserted. A spatial mode filter allows for the discrimination of laser profile artefacts due to higher order modes. The laser passes through a lens and is focused. A pinhole is placed in the Fourier plane in which the focal point of the lens is located to cut off unwanted modes. An additional lens re-collimates the laser behind the pinhole. Since only the *TEM00* mode passes through the pinhole, the laser beam is perfectly Gaussian shaped as theory predicts. A sketch of the spatial mode filter setting is given in Fig. 4.6.

For the purpose of the here presented measurements, lenses of 15 mm focal length are used. According to the estimate for the size of the pinhole $D \approx 1.3 \cdot \lambda f/r$, a pinhole of 25 μm was chosen, with D being the pinhole diameter, λ=633 nm the wavelength, f the focal length, and r=0.57 mm the $1/e^2$ radius of the laser beam. For an easier adjustment the optical components are supported by a 30 mm cage system consisting of four 3" long

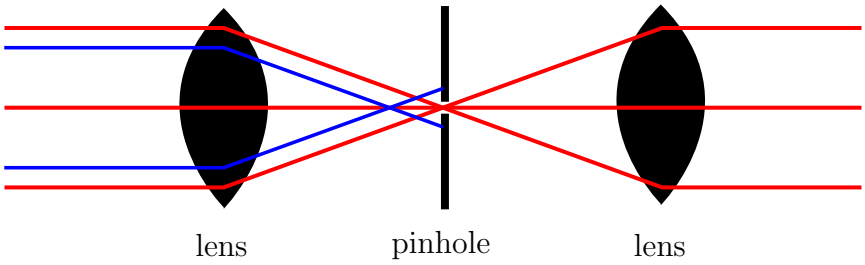

Figure 4.6: Design of a spatial mode filter

rods. The lenses are mounted on these rods to be movable in parallel to the beam axis. For the installation of the pinhole, an x-y-translation stage with two micrometer screws was used to precisely position the pinhole.

5 CID-Camera

As pointed out before beam halo measurements require a monitor with a high dynamic range. A CID-camera is a device with an intrinsically high dynamic range due to its pixel architecture. Thermo Fisher Scientific kindly provided a test model of their novel "SpectraCam XDR" for characterisation. In this section, the properties of this camera are presented with a focus on the achievable dynamic range which is required for beam halo measurements.

The Charge Injection Device was developed by General Electric Corporation in 1973. In contrast to *Charge Coupled Device (CCD)* cameras, CID-cameras are able to measure the collected charge non-destructively within a pixel. This option enables different readout modes and allows for high dynamic ranges required for halo measurements. The CID-camera used for this experiment is the SpectraCAM XDR of Thermo Fisher Scientific and was kindly provided by Thermo Fisher Scientific as a loan.

An alternative to CID cameras are *photomultiplier tubes (PMT)*. Nevertheless, the photomultiplier tube still has a lower dynamic range and a much larger pixel size. Typical parameters of all three devices is displayed in tab. 5.1

	CCD	**PMT**	**CID**
Pixel Size[μm]	$\sim$6.5×6.5	$\sim$100×100	$\sim$12×12
Pixel Full Well	$\sim$100,000	—	$\geq$500,000
Dynamic Range	$\sim 10^2$	$\sim 10^5$	$\sim 10^9$
Measurement Time [s]	$\sim$1	$\sim$1800	$\sim$600
Time resolution	$\sim$ms	$\sim$ns	$\leq$ ms

Table 5.1: Parameters of all three different detectors [45, 46, 47]

5.1 Architecture

The Charge Injection Device consists of a two-dimensional array of pixels. Each pixel consists of an n-doped epitaxial layer with a p-doped substrate layer underneath. This way they form a pn-junction. On top of the epitaxial layer there are two electrodes, as it is illustrated in Fig. 5.1. In common literature these electrodes are referred to as *drive* and *sense*, *collect* and *sense*, or *row* and *column*. Further on, I will use the terms drive and sense, as the most descriptive ones from a physical point of view. As the pixel design is symmetric, no further discrimination between the two electrodes is required from the technical perspective.

The measuring principle ia based on the *photo-electric effect*: If the pixel is hit by a photon, an electron-hole pair is created in the n-doped epitaxial layer. Since the electrodes are at all times negatively charged with respect to the substrate, the electrons can float into the substrate and the holes remain as photon generated charge. By changing the electrode potentials the holes can be moved from one electrode to the other within the pixel. [46]
All drive (sense) electrodes within one row (column) are interconnected. Therefore, each pixel is explicitly characterised by its row and column position. Since the pixel readout depends on the combined actuation of both electrodes a single pixel can be read by adjusting the voltages at its associated row and column wires without interfering with the charge acquisition of the other pixels in the same row or column. [48]

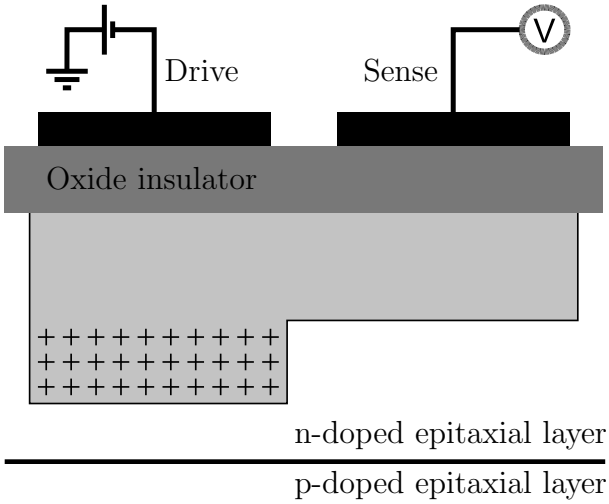

Figure 5.1: Pixel scheme

In the latest version, the *CID820* used in the *SpectraCam SPM*, each single pixel is equipped with its own preamplifier. This decreases the read noise down to 35 electrons root mean square (rms) compared to the read noise of 262 electrons rms of the SpectraCam84. By using multiple non-destructive readouts, this number can be reduced even down to 8 electrons rms.[47]

5.2 Readout

In the CCD, the accumulated charge is determined by collapsing the electrode potential and recombining electrons and holes. In this destructive kind of measurement the accumulated charge will be destroyed and cannot be used for further measurements. In contrast to this, the CID-camera is able to measure the photon generated charge non-destructively due to its two electrodes.

During charge accumulation one of the electrodes is set on a high and the other on a low potential. Since the photon generated charge is collected in the form of positively charged holes, the charge will pile up underneath the drive electrode, Fig. 5.2(a). The potential of the sense electrode is measured and the voltage of the drive electrode is changed to make the holes migrate below the sense electrode Fig. 5.2(b). When charge moves in or out of a capacitor, the electrode potential will change according to $dV = dQ/C$. Therefore, the change of the sense electrode potential is proportional to the amount of accumulated charges. The voltage change of the sense electrode is indicated in red in

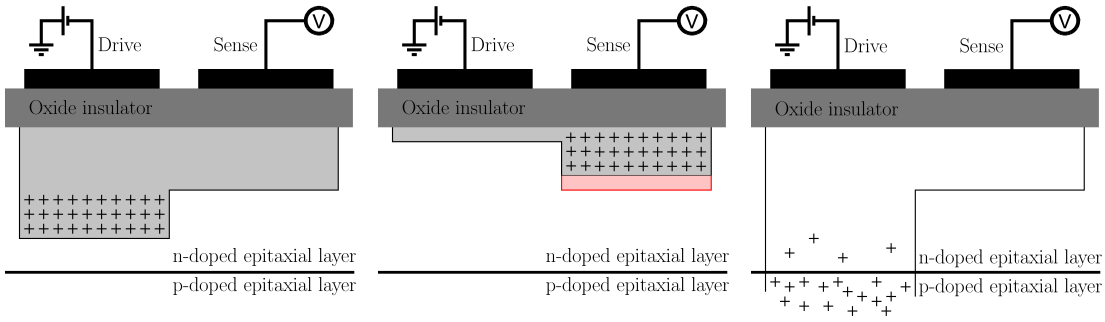

(a) Charge accumulation below one of the electrodes

(b) Drive electrode "drives" the charge under the sense electrode, causing a change in the sense electrode's voltage (red)

(c) When the pixel is full the charge is injected into the substrate

Figure 5.2: Pixel readout

Fig. 5.2(b). The mobility of the holes within the pixel cause therefore a coupling between the two electrodes with a coupling strength proportional to the accumulated charge. By measuring this coupling, one can determine the amount of charge.

After the readout of the pixel the electrodes can either be set to their original potentials, Fig. 5.2(a), or the holes can be injected into the substrate layer where they will recombine with the electrons, Fig. 5.2(c). Discharging the pixel this way is called injection. The *non-destructive pixel readout (NDRO)* is one of the unique features of CID cameras [48].

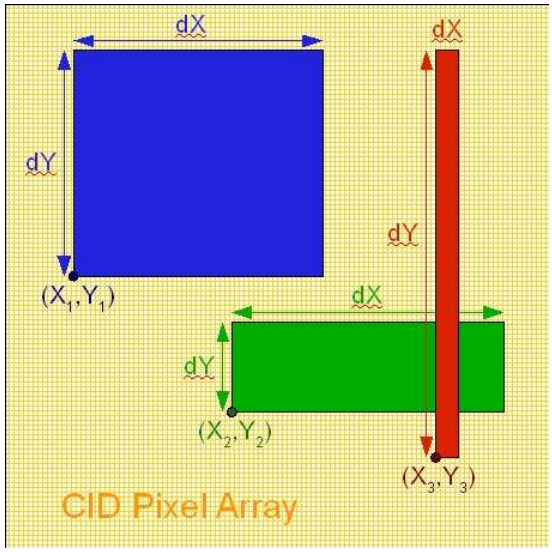

Figure 5.3: Possible Subarrays [46]

Another interesting option is to combine several neighbouring pixels together to a region which can be read together. This offers the advantage of a higher readout frequency and a better signal to noise ratio on the one hand, but decreases the resolution on the other hand. For CCD cameras, this method is known as 'binning'. In contrast to the binning of the CCD, the pixels in the CID camera are not physically combined with one another, but just read out together. Additionally, it is possible to define several rectangular subarrays of pixels that are supposed to be read independently. Those are given by the position of a corner (X,Y) and the lengths of each side (dX,dY). This way, several subarrays can be analysed during one measurement. The size of the subarrays can range from a single pixel up to the entire area of the imager. Due to the non-destructive readout of the CID camera, the different sub-arrays may overlap and may even have different exposure times, as illustrated in Fig. 5.3.

These features of the CID-camera allow for different exposure algorithms which are described in the following subsections.

5.2.1 Fixed Time Mode

In analogy to the CCD-camera, the CID can read out pixels in a fixed time mode. In this mode no NDROs are performed and no pixels are injected during the exposure. The dynamic range of the CID-camera for the fixed time mode given as the ratio between the full well capacity and the read noise like for a normal CCD-camera. The camera cannot take advantage provided by NDROs.

5.2.2 Time Resolved Mode

The non-destructive readout enables a *time resolved pixel readout*. This readout mode provides information about the temporal development of the charge acquisition within the pixel. This information can be plotted in total, as the 1^{st}, or 2^{nd} derivative of the accumulated charge versus time. Thereby, the user is able to adjust his settings in real time. It should be noted that this measuring mode requires a high memory capacity to store the data.

5.2.3 Random Access Integration

The third readout mode is called *Random Access Integration (RAI)*. For each sub-array, a control region can be defined, which is read out continuously. As soon as the accumulated charge within the control region exceed a predefined threshold, the entire sub-array will be injected and the whole process starts again until the user-defined maximum exposure time is reached. Therefore, it is sensible to choose the area with the highest illumination level as control region to ensure that no pixel saturates. The RAI mode extends the dynamic range substantially, since the maximum signal is no longer limited by the full well capacity of the pixel, but by the number of readout cycles done within the user-defined maximum exposure time.

Nevertheless, there are some practical limitations to the theoretically achievable dynamic range. Since the maximum readout-cycle frequency determines the maximum number of readout cycles, it is also a major limitation to the achievable dynamic range. This maximum readout-cycle frequency depends on the operational frequency of the CID camera on the one hand and on the number of operations that have to be performed during one readout cycle on the other hand. The number of operations will increase, if there are more or larger subarrays defined, since more pixels have to be read. However, it is possible to combine several pixels to read them out together (binning), which will decrease the

number of operations, since multiple pixels can be read simultaneously. Another issue at high illumination is that the threshold in the control region is exceeded sooner and more readout cycles are required, which can again lower the dynamic range[46].

5.2.4 Extreme DR

As a new feature of the SpectraCam SPM the *Extreme Dynamic Range (XDR)* mode has been included. It takes full advantage of the new design of the CID820 chip, like the preamplifier-per-pixel architecture, and thereby maximises the achievable dynamic range. While Random Access Integration still suffers from the limitation due to the finite cycle frequency, a short pre-exposure is made in the XDR mode to adjust the readout cycle to the actual light distribution. The better the adjustment, the higher the dynamic range that can be achieved.

If the pre-exposure is too long, the pre-exposure will overexpose, and the adjustment for high light intensities will fail. If the pre-exposure is too short, the camera can handle higher light intensities, but carries the risk of an increased background due to the lower signal to noise ratio for short exposures. In addition, the pre-exposure time should always be far larger than the time the mechanical shutter needs for opening and closing to ensure a constant illumination of the entire pixel array. To overcome this problem, it is possible to define two pre-exposures, a shorter and a longer one. Thereby, one is able to combine the advantages of short and long pre-exposures without suffering from their disadvantages.

The dynamic range of this algorithm can be calculated according to [17]

$$R = \frac{E_f P_f P_2 Q}{m\sigma} \tag{5.1}$$

where

- R = dynamic range
- E_f = ratio of full well capacity to lowest signal to be measured
- P_f = ratio of user specified exposure time to pre-exposure time
- P_2 = ratio of longer pre-exposure time to shorter one (if two pre-exposures are required)
- Q = full well capacity
- m = detection limit factor (2σ or 3σ)
- σ = read noise (30 electrons rms).

Using the XDR mode and maximising/minimising the above named values, the dynamic range can exceed 10^9 [17].

5.3 Software

The camera is controlled by the *Racid Exposure* software. It is a graphical user interface software which enables the user to adjust all settings of the camera down to the electrode voltages within the pixels. For each image acquisition several automated corrections can be applied, like a fixed noise pattern (FPN) subtraction for example.

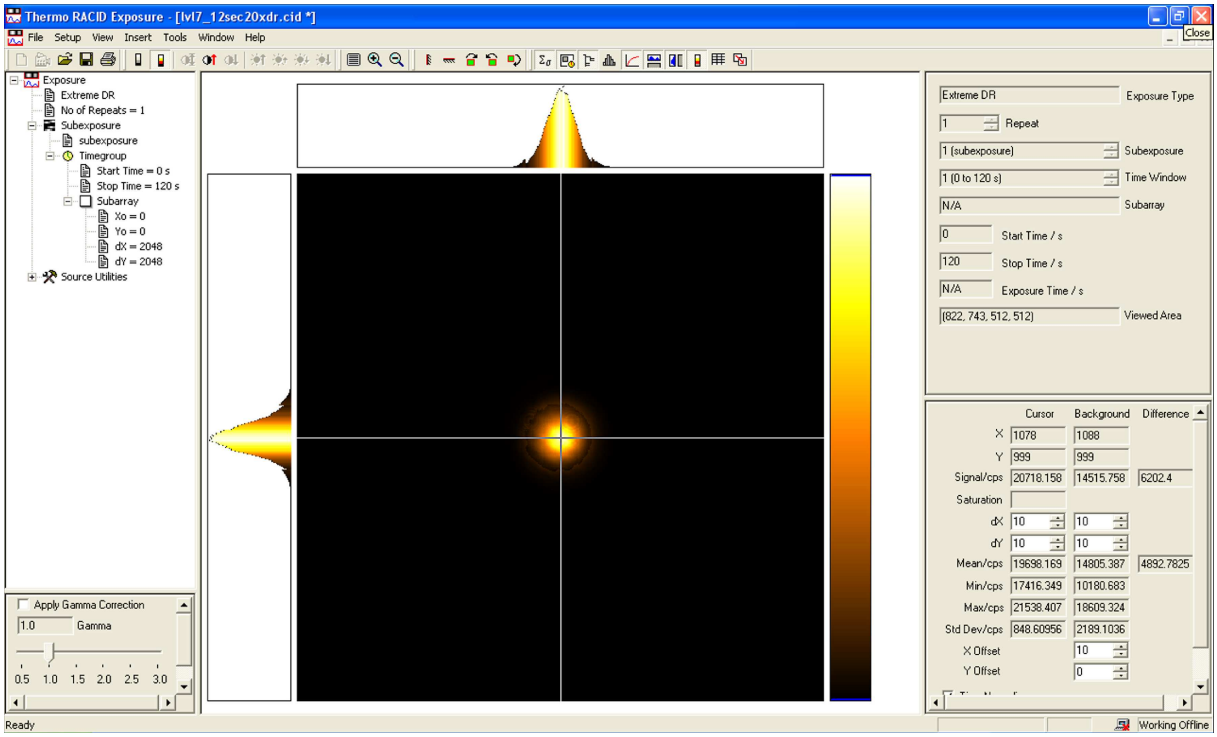

Figure 5.4: Graphical user interface of the Racid Exposure software

Fig. 5.4 shows a screenshot of the Racid Exposure software. In the central part, the acquired image is shown with the corresponding exposure data like exposure algorithm, exposure time, and size of the subarrays in the left and the upper right part. In the lower right part, the statistics of the image at the cursor position is displayed.

Before the exposure, several settings can be adjusted in the window shown in Fig. 5.5. One can choose the appropriate readout algorithm and the exposure time for the measurement. In this experiment, the Extreme DR algorithm was mainly chosen as the algorithm granting the highest dynamic range. In the subarray settings shown in Fig. 5.5(b), the size of the subarray and the number of NDROs are set up. Further options are available for different exposure algorithms.

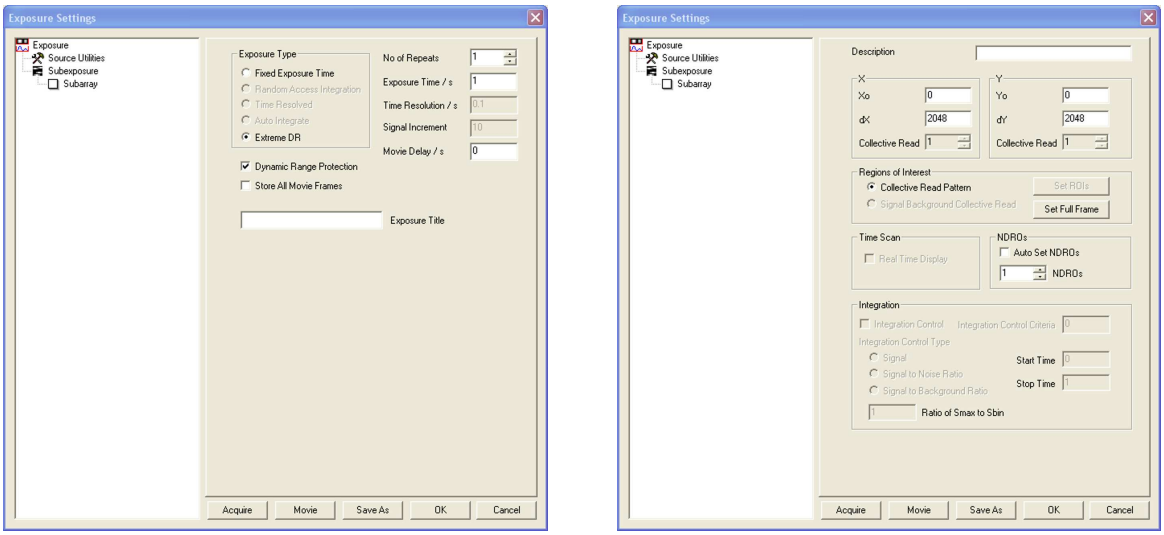

(a) Exposure settings (b) Subarray settings

Figure 5.5: New exposure window of the Racid Exposure software

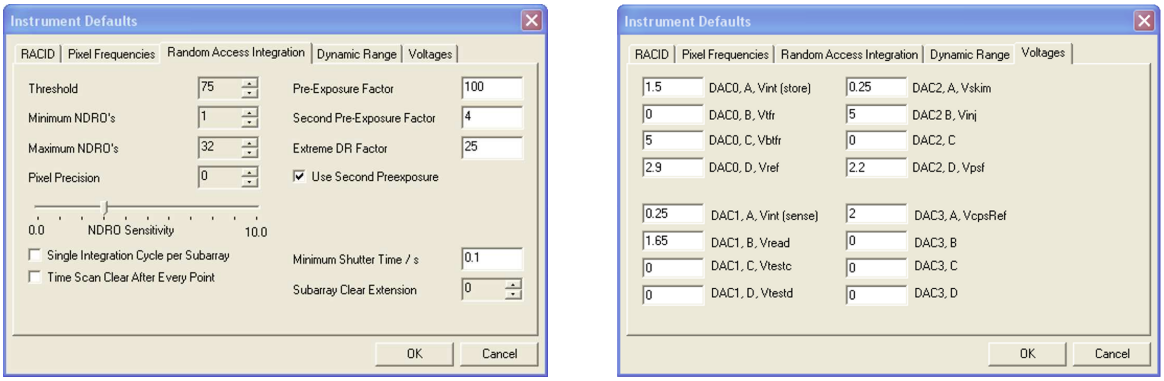

(a) XDR settings (b) Voltage settings

Figure 5.6: Additional settings in the Racid Exposure software

In the window shown in Fig. 5.6(a), the options for the Extreme DR and the Random Access Integration algorithms can be set. The most important values are the *Pre-exposure Factors* listed on the right hand side of Fig. 5.6(a). The Pre-Exposure Factor gives the ratio between the exposure and the pre-exposure times and is listed as P_f in equation 5.1. The Second Pre-Exposure Factor is the ratio between the longer and the shorter pre-exposure time in case a second pre-exposure is defined and corresponds to P_2 in equation 5.1. The *Extreme DR Factor* determines the time period in which a pixel will not saturate. The camera is able to cycle pixels that saturate in times as short as the shortest pre-exposure time divided by the Extreme DR Factor. This time T_{Sat} within each pixel can be cycled is given by

$$T_{Sat} = \frac{ExposureTime}{P_f * P_2 * XDRFactor} \tag{5.2}$$

In Fig. 5.6(b), the menu window is shown which allows for the adjustment of voltages within the CID pixel.

5.4 Commissioning

The CID-camera consists of a camera head and an external head exchanger. The head is mounted on the breadboard within the shielding box, while the external heat exchanger is mounted underneath. Both are connected via data and power cables and water tubes for the heat transfer. As coolant, de-ionised water with ethylene glycol as anti-freeze is used. The CID-camera is controlled via an Ethernet connection from the camera head to a laptop on which the Racid Exposure software is installed. To connect to the camera, a fixed IP of 192.168.1.1 with a subnet mask of 255.255.255.0 in the TCP/IP protocol has to be used.

Upon delivery, water condensed frequently on the protective glass plate in front of the imager chip which made an accurate image acquisitions impossible. Therefore, the camera the camera had to be sent back to the United States for repairs.

An internal vapour analysis was performed which indicated a partial hydrogen pressure. Therefore, the pinch tube was replaced, the head was re-pumped and refilled with argon afterwards, and the saturated hydrogen getter was re-activated. This put the atmosphere in the head in the viscous flow regime instead of the free molecular flow regime caused by the partial pressure of hydrogen. The viscous flow regime allows the argon to remain relatively warm because it will be in contact with the entire head. Since the cooling system has a high enough capacity, the additional cooling load is not an issue [49]. After the repair, there were no more condensing on the camera glass plate and the temperature dropped by almost 10°C which also reduced the background substantially. Additional test measurements under guidance of Thermo Fisher Scientific were carried out that ultimately led to a new firmware optimised for the experimental challenges of this setup.

5.5 Experimental Setup for the CID-Camera

For beam profile measurements at an accelerator, cameras are commonly not placed next to the beam line due to radiation issues. The light emitted by the beam is normally guided by a set of mirrors and lenses to the camera. The positioning of the camera away from the beam pipe allows for the installation of a shield to protect the camera from radiation damage.

The CID-camera is intrinsically less vulnerable to radiation damage than common CCD-cameras. Thermo Fisher Scientific has shortly developed a new CID-camera system which

is designed specifically for operation in high radiation measurements. This reduces the shielding requirements for this kind of camera.

At the lab test stand, a laser is used to simulate light emitted by the particle beam like SR or OTR. Since a laser has a small opening angle of 1.41 mrad, no objective lens is required for the camera, but the laser can be shot on the camera chip directly.

The CID-camera is a very sensitive device which cannot be as easily adjusted to different light intensities as a CCD-camera by just varying the exposure time. In order to achieve the maximum dynamic range without suffering negative effects described in section 5.6, the light intensity has to be adjusted carefully using neutral density filters. A sketch of the setup is given in Fig. 5.7.

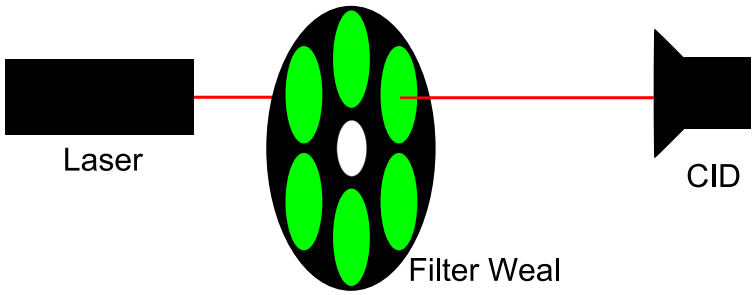

Figure 5.7: Setup for CID measurement

In later high dynamic range measurements, additional cages and baffles were inserted to minimise the scattered background light and thereby increase the dynamic range of the light distribution. For the same reason, a spatial mode filter is used for some measurements.

5.6 Negative Effects

There are several parameters which have to be adjusted properly for the optimum performance of the camera. A slight misadjustment of the camera settings may cause severe distortions in the acquired image and will also tremendously limit the achievable dynamic range. In Fig. 5.8(a), a laser beam profile is shown acquired using optimised settings for a 90 s exposure, given in table 5.2, with t_0 being the exposure time, t_1 and t_2 the first and second pre-exposure time, and XDR the XDR-factor. The grey values in Fig. 5.8 and 5.9 are scaled logarithmically while the profile above is scaled linearly to reveal potential effects on all scales. In the horizontal and vertical direction there are reflection effects visible due to the glass plate in front of the camera chip. The glass plate cannot be removed because the chip is cooled down to -47°C and requires a protective gas inside the camera head to prevent damage caused by freezing water.

In Fig. 5.8(b), the second pre-exposure time is reduced to 10 ms only. Since the shutter of the camera has an opening time of 13 ms [50] the chip will not be uniformly illuminated over an exposure time which is of the same order of magnitude. This does not have any negative effects for the image acquisition of the almost point like laser beam profile, but the image profile looks even better. But for larger images such short acquisition times have to be avoided to achieve a reliable image. If not explicitly stated otherwise, the minimum pre-exposure time of 100 ms as recommended by Thermo Fisher Scientific was used in all measurements.

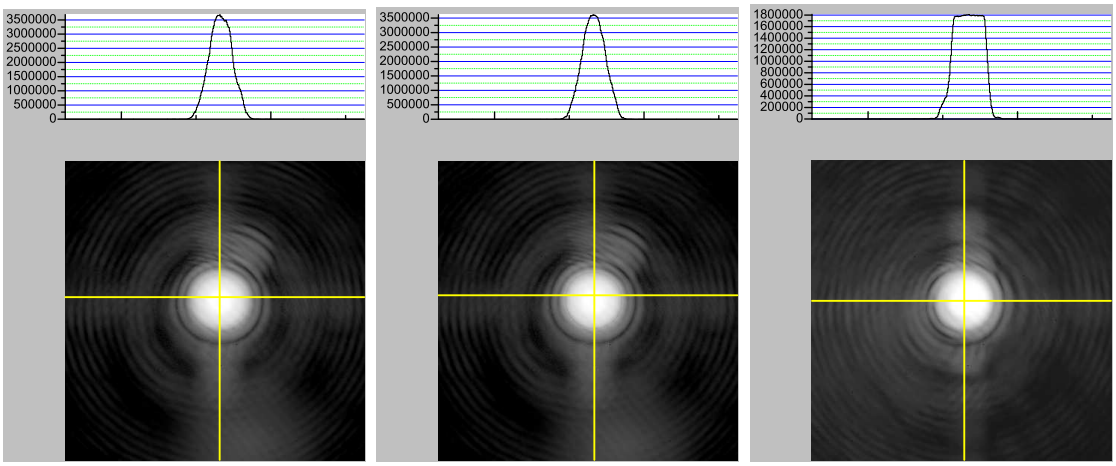

(a) Image with correct settings (b) Image with pre-exposure time too short (c) Image with background too high

Figure 5.8: Images of beam profiles with different camera settings

t_0	t_1	t_2	XDR
90 s	1 s	100 ms	10

Table 5.2: Camera settings used for image acquisition

An example for the limitations of the dynamic range is given in Fig. 5.8(c). By not closing the shielding box properly an artificial background was generated. This limits the dynamic range by increasing the standard deviation of the background on the one hand, but also decreases the maximum observable signal on the other hand. In Fig. 5.8(c), the camera therefore saturated at 1,800,000 cps.

After the pre-exposures the XDR algorithm calculates an optimised readout cycle for all pixels. If there is a strong background, the corresponding pixels have to be read more often and less operation cycles are available for the high intensity signal which will therefore saturate. For high dynamic range measurements, it is therefore crucial to minimise the background and to focus the signal on a small spot. The high dynamic range measurements presented later on are therefore only valid if the observed light distribution has its peak intensity in a very confined region with an almost negligible background.

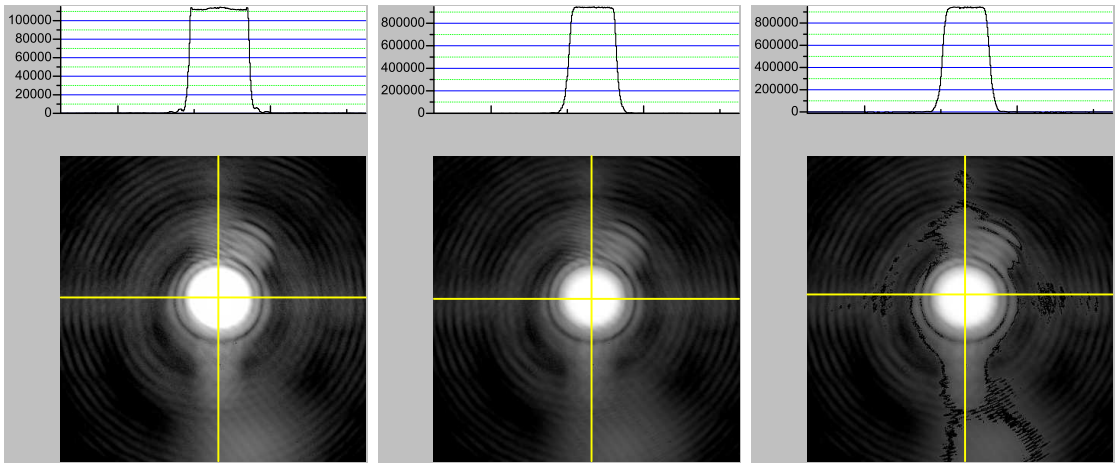

(a) Image with a single pre-exposure only

(b) Image with second pre-exposure time too long

(c) Image with XDR factor too low

Figure 5.9: Images of beam profiles with different camera settings

In Fig. 5.9(a) an image acquired without the first pre-exposure is shown. In the profile plot it is clearly visible that the camera saturated at 1,100,000 cps at a light intensity that triggered a count rate of over 3,500,000 cps measured in images 5.8(a) and 5.8(b). This proves the advantage of the dual pre-exposure mode over the single pre-exposure mode, even though the higher dynamic range of the dual pre-exposure mode was not expected to this extent based on equation 5.1.

In Fig. 5.9(b) the first pre-exposure remained at 1 s but the second was chosen to be 500 ms which is five times longer than the ideal case. The camera saturates again at a count rate of 900,000 cps which is by a factor of four too low for the light intensity applied. Assuming an approximately constant background for all images, the saturation threshold is proportional to the dynamic range and the measurement is in good agreement with equation 5.1.

In Fig. 5.9(c), both pre-exposures times remained at their ideal values, but the XDR-factor was reduced by a factor of five to XDR=2 only. As for the previous setting, the camera saturates at 900,000 cps, but the strong distortions visible in the image are even more obvious.

5.7 Camera Calibration

In this section the calibration of the CID-camera by two different methods is presented. Since the CID-camera counts the number of cycles to avoid saturation of the pixel, a highly linear response is expected. This needs to be validated before any quantitative measurements can be performed.

5.7.1 Calibration with a Mask

First, the CID-camera was calibrated by a well known high dynamic range light distribution. By comparing the camera count rate with the actual light distribution the camera can be calibrated. For accuracy reasons it is essential to know the exact correlation between the camera count rate and the observed light distribution.

In order to generate a well known high dynamic range light distribution, an aluminium mask with four circular holes of 3 mm diameter was illuminated by a homogeneous light source, as described in section 4.4. Onto these holes, neutral density filters can be screwed to vary the light intensity. On the backside, a small bar is mounted to support the homogeneous light source. The mask was built by the MPIK workshop based on the design drawing listed in Appendix B.

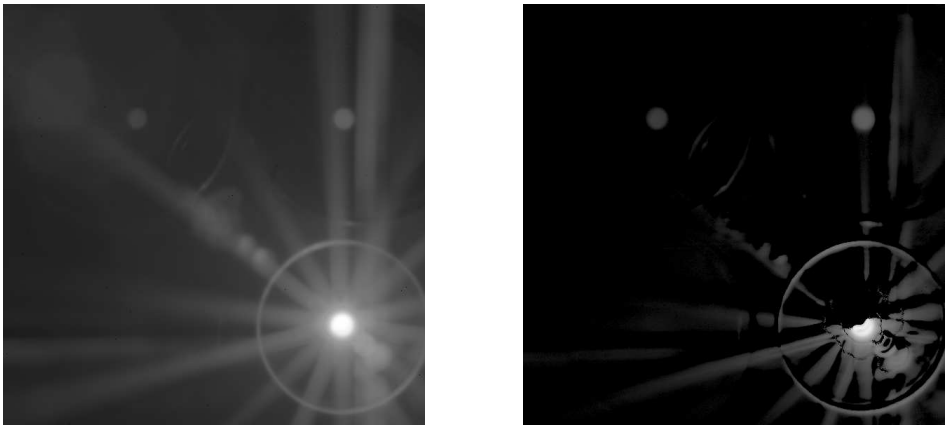

(a) Acquired image before background-correction with two superimposed light spots

(b) Acquired image after background-correction with the two light spots clearly visible

Figure 5.10: CID background-correction

A series of images with different neutral density filters were acquired by a 90 s exposure with a first pre-exposure of 1 s and a second pre-exposure of 100 ms. During all image acquisitions on one of the four holes on the mask no filter was mounted to serve as a reference for the light intensity. Therefore, the calibration can also be seen as the first dynamic range measurement.

As illustrated in Fig. 5.10(a), the high light intensity from the open hole causes reflections within the objective lens which superimpose the low signal from the holes above which are covered by neutral density filters. To eliminate these reflections, an image of the bright hole only is subtracted. An example for a background-corrected image is given in Fig. 5.10(b). Both images have the same logarithmic colour definition. The superimposition of the two low intensity signals in the upper region of the image is well reduced.

Since the light intensity of the four holes differed, the signal had to be normalised to the

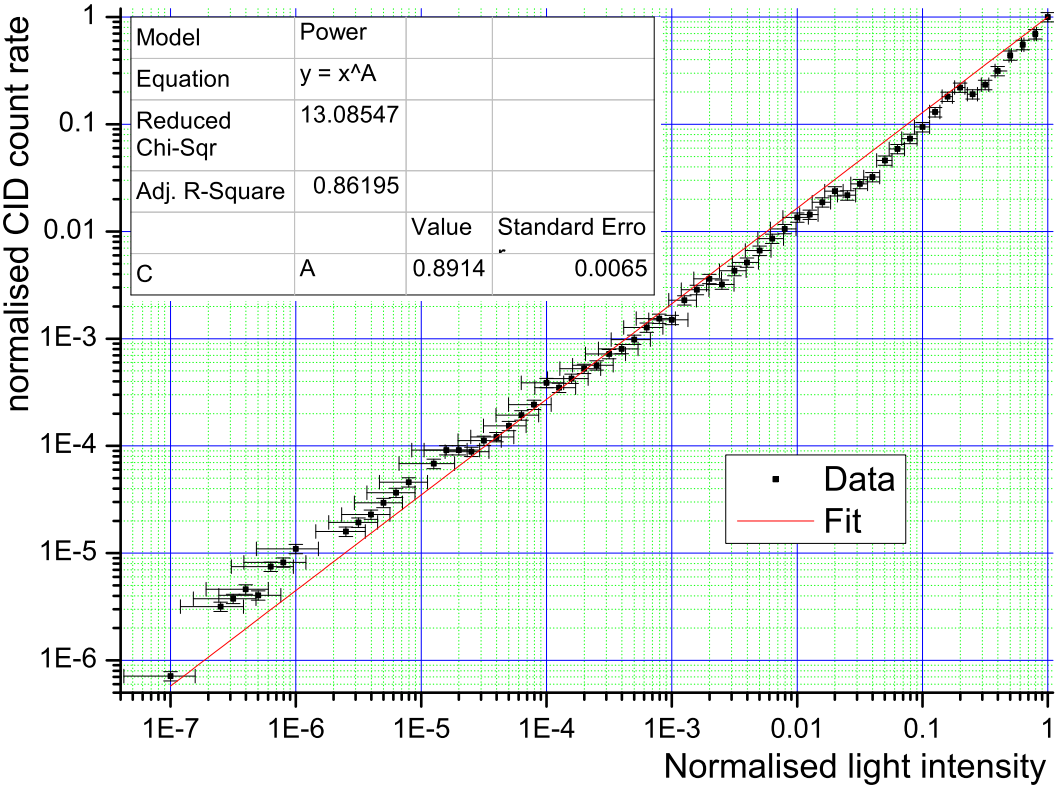

Figure 5.11: CID-calibration by a mask

light intensity of the hole without neutral density filters included. The corrected camera count rate is plotted versus the normalised light intensity generated by the neutral density filters, as shown in Fig. 5.11. An error of 20% is assumed for the CID-output and the error of the light intensity is derived from the neutral density filter errors. The measured data is fitted according to $A|x - x_c|^p$ and the exponent p was found to be $p = 0.89 \pm 0.01$ which does not match the expected linearity of the camera.

The uneven course of the data points and the very high reduced X^2 value give rise to assume a systematic error. The error is probably caused by the setting of the neutral density filters and is not due to the CID-camera.

The neutral density filters are wavelength dependant, Fig. 4.3. As already stressed in section 4, this dependency is strongest for the high level density filters that have a far higher transmission for wavelengths above 670nm. Since the OSL1-EC covers a broad spectral range from 450nm up to 800nm, as shown in Fig. 4.4(b), particularly the high level neutral density filters are sensitive to large systematic errors. This explains the discontinuity where the strongest neutral density filter is exchanged.

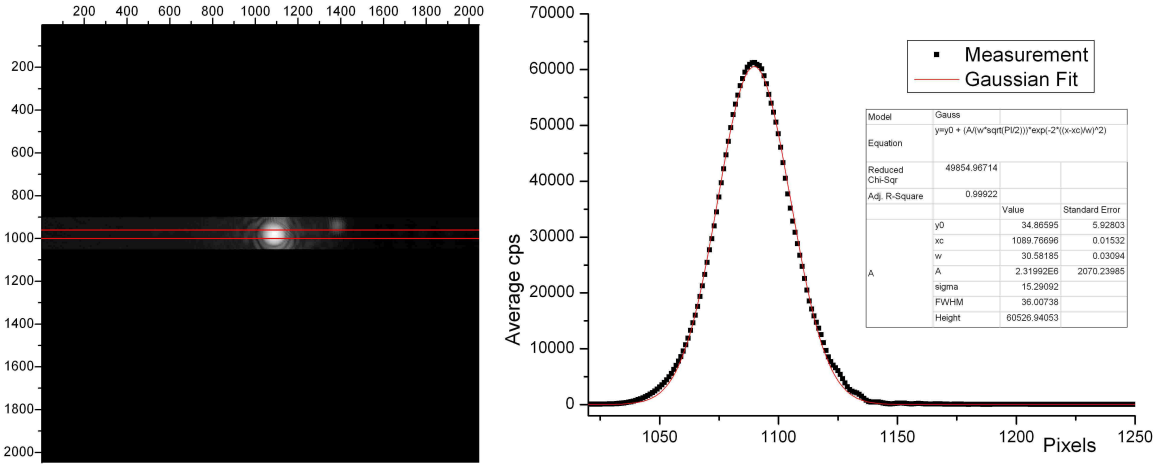

(a) Image of 2D laser profile with projection region

(b) Projection to horizontal plane

Figure 5.12: Example of a laser profile

5.7.2 Calibration with the Laser

Since the Calibration with mask failed due to the wavelength dependant neutral density filters, a laser calibration was performed in addition. The laser in use has a wavelength of 633nm, which is exactly the wavelength that the neutral density filters are calibrated for. Therefore, laser profiles of different light intensities generated by combinations of neutral density filters are measured.

For the measurement, the pre-exposure factor was set to 300 and the exposure-time was increased from 60 s for high intensities, over 120 s in the medium, and up to 300 s for the low intensity regime. Since the pre-exposure factor is fixed, the ratio between exposure time and pre-exposure time is constant. If the pre-exposure time is too short for the high light intensity, the camera will saturate during the pre-exposure and can no longer generate an ideal read-out algorithm. The laser peak is horizontally projected over 40 pixels which corresponds to 480 μm. Thereby, the two dimensional image is projected to one dimension. It was therefore possible to use a thin subarray which also increases the dynamic range.

All profiles of different light intensity are projected over the same range and a Gaussian is fitted to the one dimensional data set using Origin 8.0. The resulting fit parameter for the Gaussian heights is taken as a measure of the camera output and is plotted versus the normalised light intensity calculated from the neutral density filters as displayed in Fig. 5.13.

Since the fitting error calculated by Origin is negligibly small, an error of 5% is assumed for the fitting parameter. The light intensity passing through a series of neutral density filters numbered by i is given by $I = 10^{\sum_i x_i}$. The error of the light intensity is calculated

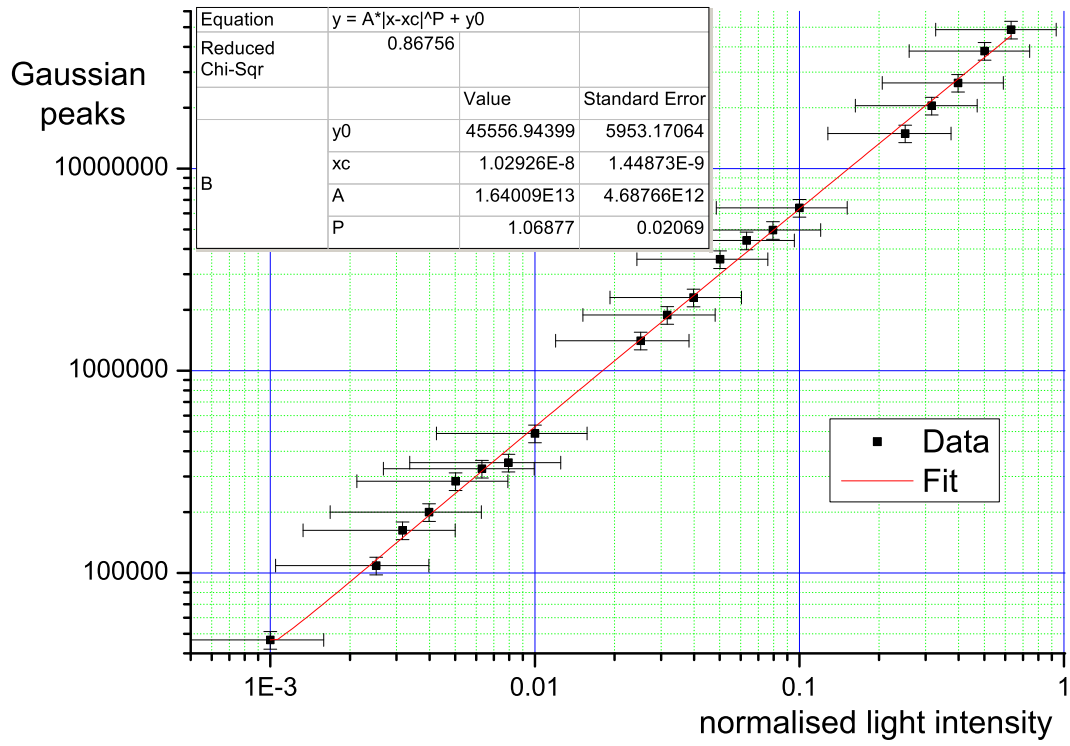

Figure 5.13: Calibration of the CID camera

according to the specifications of the neutral density filters, given in table 4.1 using the Gaussian error propagation formula.

$$(\Delta I)^2 = \sum_i \left(\frac{\partial I}{\partial x_i} \Delta x_i \right)^2 = (\ln(10) I)^2 \sum {\Delta x_i}^2 \tag{5.3}$$

A polynomial $A|x - x_c|^p + y_0$ was fitted to the data. The best fit exponent parameter p is $p = 1.069 \pm 0.021$. With respect to the large systematic errors of the neutral density filters even for their design wavelength, this is in good agreement with the expected linear response of the CID-camera.

5.8 High Dynamic Range Measurements

The dynamic range of a camera is defined as the highest observable signal divided by the lowest observable signal. When using a mask with different light intensities like in section 5.7.1 highest and lowest signal are easily measurable. As seen in section 5.7, it is very difficult to set up a well defined light distribution with dynamic ranges high enough to fully test the CID-camera. Even the Gaussian profile of a laser that could be used as a well known light distribution, only ranges over four to five orders of magnitude.

For even higher dynamic ranges, it is required to make two assumptions. First, one has to assume the linearity of the camera which has been tested in section 5.7 in order to

be able to calculate the dynamic range based on the camera output and to be no longer constrained by a well known light distribution. Secondly, the assumption is needed that any signal larger than the standard deviation of the background is measurable. This assumption changes the definition of the dynamic range to be the ratio between the highest observable signal divided by the standard deviation of the background.

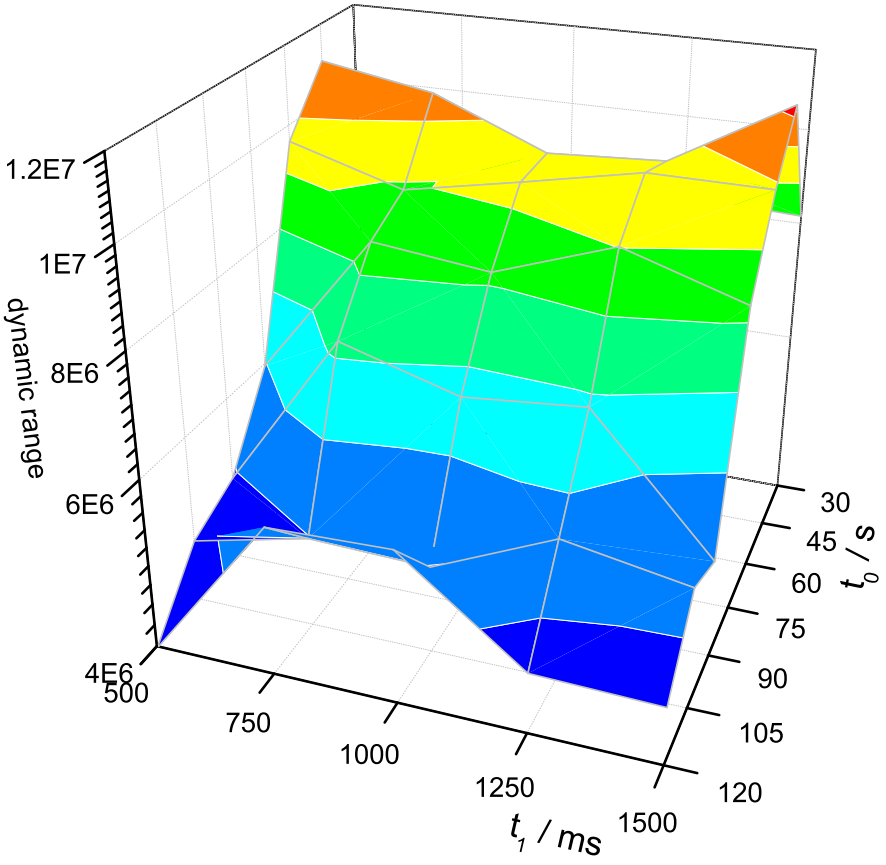

Figure 5.14: Dynamic range vs t_0 and t_1

As discussed in section 5.6, a too short second pre-exposure t_2 increases the dynamic range while causing an inhomogeneous illumination of the camera chip. The second pre-exposure time is therefore set to its minimum value, t_2=100 ms. The XDR factor was found to have only a slight effect on the achievable dynamic range. The two remaining quantities are the total exposure time t_0 and the first pre-exposure time t_1.

For the measurement, all the negative effects described in section 5.6 needed to be avoided carefully to achieve the optimum result. It is also important to perform the measurements on a warm laser. If the laser is still warming up, the results of the measurement are getting worse and are not reproducible either. The major source of fluctuations in the dynamic range is probably caused by laser instabilities. The achieved dynamic range plotted versus the exposure time t_0 and the first pre-exposure time are given in Fig. 5.14.

The standard deviation of the background required for the calculation of the dynamic

range was determined in a slightly illuminated corner of the image over 200×200 pixels. The highest dynamic ranges of up to $1{:}11{\cdot}10^6$ are achieved for 45 s to 60 s exposures with first pre-exposures between 750 ms and 1250. In this region, the dynamic ranges vary only a little, which makes it the most stable operating region. For higher exposure times they drop very fast particularly for a pre-exposure factor below 750 ms or above 1250 ms.

5.9 Dynamic Range for Low Exposure Times

For most accelerators acquisition times in the order of minutes are far too long. It is therefore essential to know what dynamic ranges are achievable for far lower exposure times in the order of a few seconds.

The dual pre-exposure mode is specifically designed for longer exposure times to achieve higher dynamic ranges. For short exposure times, it has to be checked which exposure mode grants the better results. Measurements are done for exposure times ranging from 25 s down to the minimum exposure time possible, 1 s for the single pre-exposure mode, 2 s for the dual pre-exposure mode. The exposure time is limited by the minimum values for first and second pre-exposure factors (2 and 10) pre-defined by the "Racid Exposure" software and the claim to have no shorter pre-exposure times than 100 ms.

For all these exposure times, the maximum signal at which the camera saturated was fixed at $4.6 \cdot 10^6$ cps and was limited by the 100 ms pre-exposure. This limitation could be overcome by a faster shutter. The dynamic range is therefore inversely proportional to the standard deviation of the background and is shown for single and dual pre-exposure modes in Fig. 5.15(a).

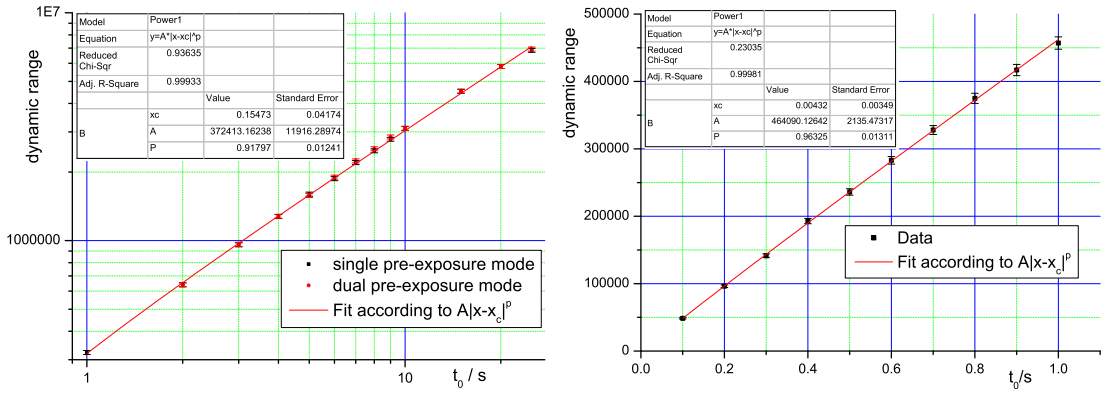

(a) Dynamic range vs exposure time for single and dual pre-exposure mode

(b) Dynamic range vs exposure time with $t_2 =$ 10ms

Figure 5.15: Dynamic range for short exposure times

The single and the dual exposure mode grant precisely the same dynamic ranges. The single pre-exposure mode is therefore preferable because it requires a shorter time to

calculate the optimised readout algorithm.

The dynamic range rises linearly with the exposure time. The maximum observable signal is mainly determined by the pre-exposure time and the decrease of the dynamic range is due to a stronger background. In shorter exposure times, not enough injection cycles in the low intensity region can be performed to achieve a reasonable signal.

To realise even shorter exposure times, the minimum pre-exposure time was reduced to 10 ms. The manufacturer of the camera advised against this to ensure a homogeneous illumination of the camera chip, but for the tiny laser spot this is not an issue. The results are displayed in Fig. 5.15(b). A fit was performed by the Origin fit routine according to $A \cdot |x - x_c|^p$. The exponent is determined to be 0.96 ± 0.01. The fit allows for an extrapolation down to exposure times below 100 ms. Based on this extrapolation, the critical exposure time is determined to be (4 ± 3) ms at which the dynamic range vanishes.

5.10 Conclusion

The unique architecture of charge injection devices allow for an intrinsically very high dynamic range. In the measurements carried out in the frame of this thesis, dynamic ranges of over seven orders of magnitude have been achieved. Measurements with exposure times ranging from 100 ms up to 120 s were performed and evaluated. The effects of the different parameters that need to be adjusted are explained and the consequences of misalignment pointed out.

The highest dynamic ranges are found for exposure times in the range between 40 s and 60 s. For lower exposure times, the dynamic range decreases linearly which is due too an increased background. CID-cameras might therefore also be suitable for applications with short acquisition times, but they cannot deploy their full potential. For such applications, one also needs to take the pre-exposures and the duration of the optimisation process into account.

A particular feature of the XDR-algorithm is the dependency of the dynamic range on the light distribution to be measured. This grants the opportunity to set up a transverse beam profile monitor with variable dynamic range and spatial resolution by including variable focussing devices.

6 Flexible Core Masking Technique

If a camera does not have an intrinsically sufficient high dynamic range like a CID-camera, a technique is required to increase its dynamic range externally. The flexible core masking technique, described in the following chapters, is based on the core masking technique which is well established in astronomy to observe the corona of the sun for instance. For an accurate image acquisition of the corona, an exposure time is required at which a normal camera overexposes due to the bright central region of the sun. The resulting blooming effects will superimpose the corona light and make an accurate image acquisition impossible. Therefore, the central bright region of the sun is masked out to allow for a corona measurement without any negative blooming effects. The same principle can be applied for beam halo measurements, as shown in [51, 52, 53]. Test measurements of this kind have been performed at CERN by T. Lefèvre et al [20].

Unlike astronomical objects, an accelerator beam's profile is typically variable in shape. A technique using a fixed mask does not suffice any more and a flexible core masking technique is required. Taking advantage of the unique features of a *Digital Micro mirror Device (DMD)*, flexible masks required for this technique become feasible. In this section the DMD will be discussed in detail.

6.1 Digital Micromirror Device (DMD)

The (DMD) was developed in 1987 by L. Hornbeck [55]. The DMD used in this measurement is the Discovery 1100 by Texas Instruments, technical details are listed in tab. 6.1. It is built up of a layer with several microscopic mirrors upon. Each of these mirrors can be set individually to an ON or an OFF state by rotating them around a small angle. Thereby, incident light will be reflected in different directions according to the state that the illuminated pixel is in. Since the pixels only have a size of $13.7 \times 13.7 \mu m^2$ [56], it is even possible to display small figures. This way, the DMD can be used as a passive optical display. Or, if the reflected light is focused on a screen, it can be used as a projector. Due to the fast cycling time of the DMD of about $25 \mu s$ [57], it is even possible to overlay different colours to create a coloured image on the screen. This method is a central element of today's beamer technology [55].

Resolution	1024×768
Pixel Size	$(13.7 \times 13.7)\,\mu m^2$
Angle	12°
Optical Fill Factor	85%

Table 6.1: Main properties of the Discovery 1100[56]

Figure 6.1: DMD on circuit board [54]

For beam halo monitoring the DMD is used to separate the main core of the beam from its halo. OTR or SR is reflected by the DMD onto a camera that measures the beam profile. From the profile image a mask for the main beam core can be generated. If the mask is displayed on the DMD, the beam core will be deflected and only the beam halo will be monitored by the camera.

6.1.1 Single Pixel Design

The features of the DMD are based on its pixel design. Each single pixel can be separated in a substructure and superstructure. The mirror (Fig.2(b)-1) itself is attached to the superstructure. The substructure of the pixels consists of a silicon substrate (Fig.2(b)-2) with an insulating layer (Fig.2(b)-3) on top, which insulates the superstructure from the substructure. Within the insulating layer there are several holes in order to allow electrical connection of the superstructure with the circuits within the substrate. Upon the insulating layer, there is a thin metallic layer, which forms the lower address electrodes (Fig.2(b)-4) and also supports the hinge. The hinge consists of a flexible torsion beam (Fig.2(b)-5), the large hinge yokes (Fig.2(b)-6), and upper address electrodes (Fig.2(b)-7).

If there is an appropriate potential applied to the upper and the lower electrodes (Fig.2(b)-4; 2(b)-7), the electrostatic force between them induces a torque and causes the hinge to

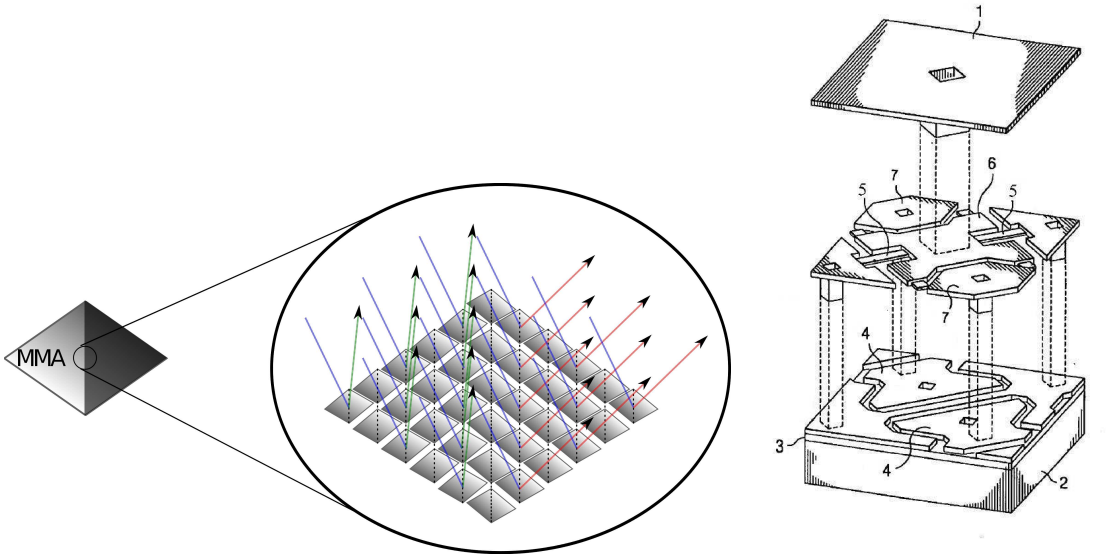

(a) DMD with pixel magnification (b) DMD Pixel Scheme [58]

Figure 6.2: Digital Micro-mirror Device (DMD) layout

tilt. The torsion beam (Fig.2(b)-5) acts as a torsion spring and creates a resisting torque. The hinge is tilted until the resisting torque of the torsion spring and the electrostatic torque are of the same magnitude or until it is stopped mechanically by touching the substructure. Since the pixel is used only in a digital ON-OFF mode, the voltage between the two electrodes is set high enough to cause the maximum deflection in one or the other direction. If the upper and the lower electrodes touch, some serious problems can occur. Due to the current, the two electrodes could weld and the pixel would be destroyed. Therefore, the electrodes are coated with a special material to prevent the electrodes from fusing together.

6.1.2 Software

The DMD is controlled by a computer software which is described in this section in more detail. The "*DMD Discovery 1100 Controller*" software [56] is a graphical user interface which enables the user to easily display images on the DMD. The images can be loaded as *.jpg, *.bmp, *gif, or *.ddc files into the Discovery software. Since the DMD is a digital device with its micro mirrors either set to 1 or set to zero, i.e. bent to the right or to the left, the image first has to be converted into a black-white image. The image pixels will be set to black or white according to whether their brightness is higher or lower than a user defined threshold. This works for coloured images as well as for greyscale picture. This newly created 1-Bit monochrome image can now be displayed on the DMD. In addition, the image can be inverted or mirrored by the software.

The source code of the software is available in Visual Basic 6.0. This allows for modi-

fication of the software, adjustment to individual needs and the insertion of additional software components which are also available in Visual Basic 6.0.

6.2 Experimental Setup

In this section, the implementation of the flexible core masking technique is presented. An image displayed on a DMD will serve as a mask to blank out the central beam core. The laser beam must therefore be reflected by a DMD onto a CCD camera. The schematic setting is illustrated in Fig. 6.3.

An image of the reflected laser beam is acquired by the CCD-camera. From this image a mask is generated which covers n·σ of the laser beam profile, with σ being the standard deviation of the profile. If this mask is displayed on the DMD at the correct position, the central part of the laser beam will be deflected and only the beam halo will still be reflected onto the camera.

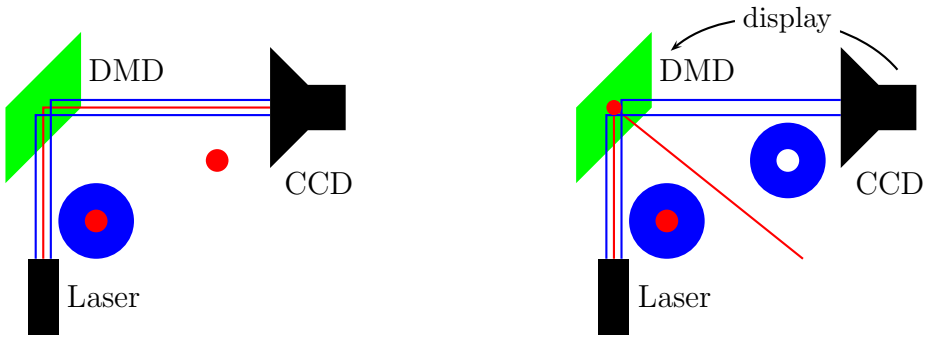

(a) Laser profile measurement (b) Display beam core on DMD

Figure 6.3: After the core profile is measured (a), the image (red) is displayed on the DMD to mask out the core that only the halo is deflected onto the camera (b)

The CCD-camera and the DMD are controlled using a single computer program and thereby creating an interface between the camera and the DMD which is described in further detail in section 6.4.

6.3 Generation of the Mask

The mask is generated by displaying an image of the laser beam core on the DMD. This image is acquired by directing the laser on the camera chip and adjusting the exposure time in such a way that the maximum signal is little below the saturation threshold. Since the DMD is a digital device, the grey-scale image acquired by the CCD has to be transformed into a binary image. All pixels above a certain threshold are set to white,

and all pixels below are set to black. Finally, the mask can be rescaled to the size required for the measurement.

The mask generation process consists therefore of three parts:

- the beam profile measurement
- the conversion in a binary image and
- the re-scaling of the mask to the desired size.

To have a minimum negative effect of any light intensity fluctuations on the mask size during the image conversion, the threshold should be applied at the point of the maximum slope of the intensity distribution. As the mask is resized the error of the mask shape also increases by the scaling factor. It can therefore be assumed that the total error of the mask is given by

$$\Delta M \propto \left(\frac{\partial I(x)}{\partial x}\right)^{-1} * R \quad , \tag{6.1}$$

with ΔM being the error of the mask shape, $I(x)$ being the light intensity distribution at threshold position x, and R being the scaling factor. Assuming a Gaussian intensity distribution, ΔM is minimised by setting the first derivative to zero.

$$\frac{\partial}{\partial x}\left(x\frac{\partial}{\partial x}e^{-\frac{x^2}{2\sigma^2}}\right) = -\frac{\partial}{\partial x}\frac{x^2}{\sigma^2}e^{-\frac{x^2}{2\sigma^2}} \tag{6.2}$$

$$-\frac{\partial}{\partial x}\frac{x^2}{\sigma^2}e^{-\frac{x^2}{2\sigma^2}} = \left(-\frac{2x}{\sigma^2}+\frac{x^3}{\sigma^4}\right)e^{-\frac{x^2}{2\sigma^2}} = 0 \quad . \tag{6.3}$$

This yields $x^2 = 2\sigma^2 \Rightarrow x = \sqrt{2}\sigma$. The threshold for setting the 8-bit grey values to black or white is therefore chosen to be at $1/e$ of the maximum brightness. The highest brightness in an 8-bit image is $2^8 - 1 = 255$ which gives a threshold of $255/e$.

Before this optimisation process, the mask was generated using the default threshold value of the DMD. With such an inaccurately generated mask, no halo monitoring is possible since strong interference and diffraction patterns will superimpose the halo signal. Since the manual threshold adjustment was not foreseen in the original controlling software and could not be included, it had to be rewritten.

Since the image is taken by the CCD with a pixel size of 5.2 μm and is displayed on the DMD with pixel size of 13.68 μm, the image has to be rescaled by a factor of $13.68/5.2 \approx 2.63$. If the laser beam hits the DMD at an incident angle α, as displayed in Fig. 6.3, the horizontal component of the image also needs to be stretched by a factor of $\cos(\alpha)^{-1}$.

6.4 Control Software

Two separate computer programs for the control of the CCD-camera and the DMD were delivered with the hardware. The producing companies, IDS [44] and Texas Instruments [59], kindly provided the source code written in Visual Basic 6.0, which allowed for the fusion of both programs to a single software able to control the CCD and the DMD, generate the mask, and display the mask on the DMD at the correct position to deflect the laser beam core.

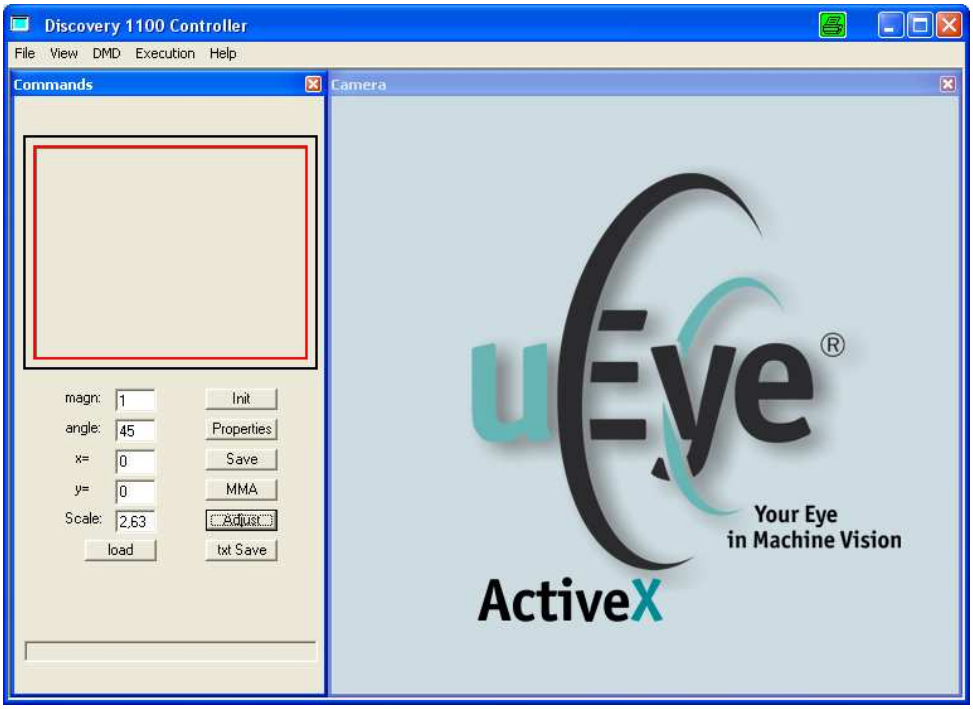

Figure 6.4: Graphical User Interface

A screenshot of the Graphical User Interface of the combined control software is shown in Fig. 6.4. In the "Camera" window on the right hand side, the image taken by the CCD is displayed in live mode after the camera is initialised by the "Init" button in the "Commands" window. The "Properties" button opens a window to set various camera properties like the exposure time. The "save" button below allows for saving the image which is temporarily displayed in the "Camera" window as a bitmap file. The "MMA" button generates a mask based on the image displayed in the "Camera" window and displays it on the Micro-Mirror-Array. By changing the numbers in the text boxes to the left, it is possible to adjust the magnification and the position of the mask, or correct for an angle in the set-up, or outweigh the different pixel sizes of CCD and DMD. The changes will be applied to the displayed mask by pressing the "Adjust" button. With the "txt save" it is possible to save the currently displayed image as a text file. The brightness of each single pixel of the image is saved as an integer ranging from 0 to 255. This enables

further analysis by C++ and Origin.

6.5 Calibration

Due to the small dynamic range of the CCD-camera at a fixed exposure time, it is necessary to check the linearity of the CCD output as well as the exposure time dependency. As Calibration, laser light passing through different neutral density filters was used. To avoid the problems caused by the wavelength dependent neutral density filters, a laser Calibration is performed as discussed in section 5.7.2 for the Calibration of the CID-camera.

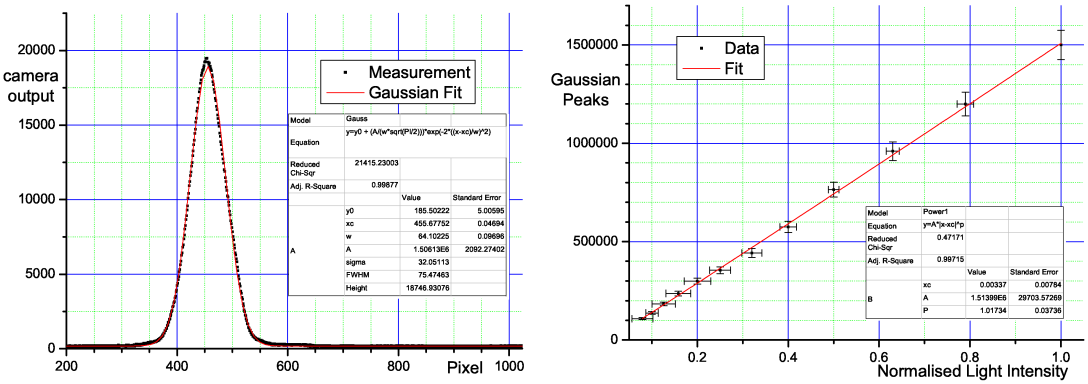

(a) Projected data with Gaussian fit

(b) Gauss fit peaks vs light intensity

Figure 6.5: CCD Camera Calibration

Laser beam profiles at different intensities were measured and projected to one dimension. On each data set a Gaussian distribution was fitted, as shown in Fig 6.5(a). The peak value determined by a Gaussian fit was plotted versus the light intensity derived from the neutral density filters. The error of the light intensity was calculated using the errors of the neutral density filters listed in 4.1, the errors of the Gaussian Peaks were assumed to be 5%. This data was fitted according to $y = A|x - x_c|^p$ to test the linearity. The exponent p was found to be 1.017 ± 0.037 which indicates the linearity of the camera output.

In a second step, the dependency on the exposure time is tested. Depending on the light intensity the highest exposure time without saturation effects is chosen, as illustrated in Fig. 6.6(a). In Fig. 6.6(b), the Calibration of the CCD-camera with respect to its exposure time is presented. Again, the error of the light intensity was derived from the error of the neutral density filters and the error of the highest exposure time at which no saturation occurs is estimated to be 10%. Since the exponent parameter of the fit according to $y = A|x - x_c|^p$ is $p = 0,9666 \pm 0,008$ the ratio of camera output and exposure time can be considered to be a good measure for the light intensity.

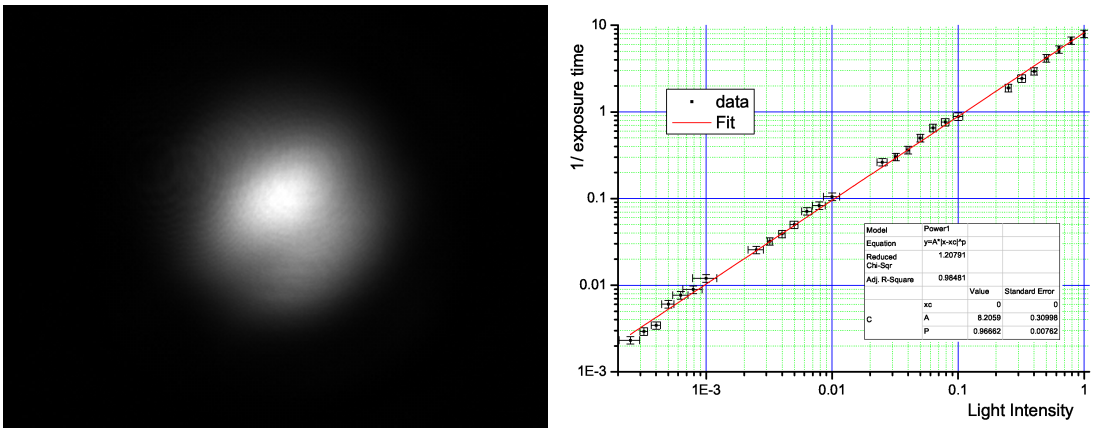

(a) Image of highest possible exposure time (b) Inverse exposure time vs light intensity

Figure 6.6: Inverse exposure time vs light intensity

6.6 Negative Effects

Apart from negative effects resulting from errors in the mask, there are several further error sources. A special inconvenience is the interference which is caused by the coherent laser.

Since the DMD has a grid-like structure, it does not reflect the laser beam, but it rather generates a broad interference pattern as it is known from spectroscopy. Due to the large angular dependency of the interference pattern, already after a few cm the maxima have no overlap any more and can be measured like a reflected beam. To minimise potential distortions of the image due to interference or the required horizontal stretching of the mask, the beam is reflected almost perpendicularly to the DMD. Assuming that the laser profile remains intact, the main interference maximum is observed. This assumption is tested and found to be valid. Corresponding experimental results are given in section 6.7.

Interference also takes place at the glass plate in front of the CCD-pixel-array. If the laser beam enters the camera in an unfortunate angle, the beam profile will be strongly distorted, as shown in Fig. 6.7(a). In addition, due to some slight uncleanness of the plate, Newton rings can occur as demonstrated in Fig. 6.7(a). These effects have a severe effect during the mask generation since the errors result in a distorted mask which cannot properly mask out the beam core any more. Therefore, especially during the mask generation process, great care has to be bestowed on a neat measurement.

6.7 Flexible Core Masking Measurements

In this section test measurements of the flexible core masking technique with a DMD are presented. First, the laser beam core profile is acquired to generate a mask. Secondly,

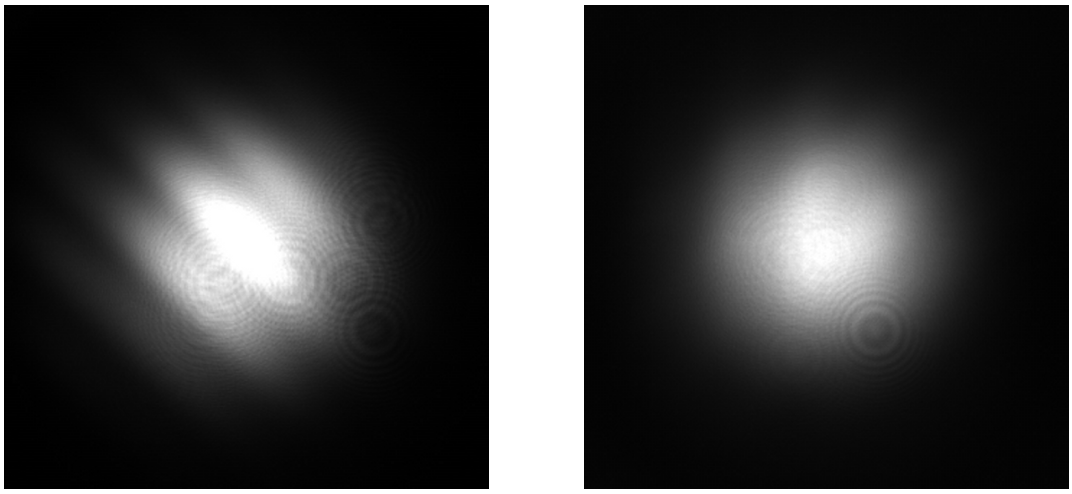

(a) distorted image (b) undistorted image

Figure 6.7: Distorted 7(a) and undistorted 7(b)image

the mask is displayed on the DMD to blank out the beam core to allow for the beam halo measurement as the third step.

In contrast to a CID-camera, a CCD-camera has no continuous intensity output. As an 8 bit camera it generates integer values between 0 and 255. The definition of the dynamic range as the maximum observable signal divided by the standard deviation of the background is therefore only sensible, if the standard deviation is in the order of one. To avoid diverging dynamic ranges due to an apparently constant background, no background deviation smaller than 0.5 is valid.

The first step of the flexible core masking technique is the generation of the mask. Therefor, an image of the laser beam profile is taken at the position where in the later experiment the DMD will be located. This grants the advantage over the method described in section 6.2 that the widening of the laser needs not to be taken into account and that no distortions caused by the DMD will diminish the quality of the mask. However, for an automated mask generation-image acquisition system, this setup is not suitable.

6.7.1 Pure laser beam

In a first step, the profile of the pure laser beam is measured without any additional devices in the beam line. After the mask generation, as described in section 6.3, camera and DMD are set up as displayed in Fig. 6.3(b). With the control software, the mask size can be varied and the camera exposure time adjusted accordingly. Images of laser beam profiles with deflected beam cores are given in Fig. 6.8, for a 1σ mask in 6.8(a), for a 2σ mask in 6.8(b), and for a 3σ mask in 6.8(c).

The images were saved as an ASCII document which allowed for a quantitative analysis.

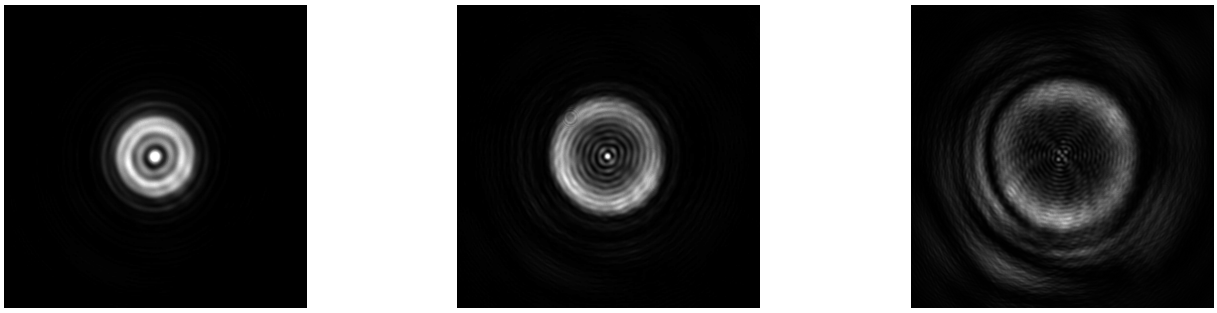

(a) 1σ mask (b) 2σ mask (c) 3σ mask

Figure 6.8: Laser beam halo profile acquired with different mask sizes

The data is projected over a row of 10 to 20 pixels including the maximum of the distribution to optain better statistics. Since all images are taken with different exposure times, the data needs to be corrected by dividing the camera output by the individual exposure time of the measurement.

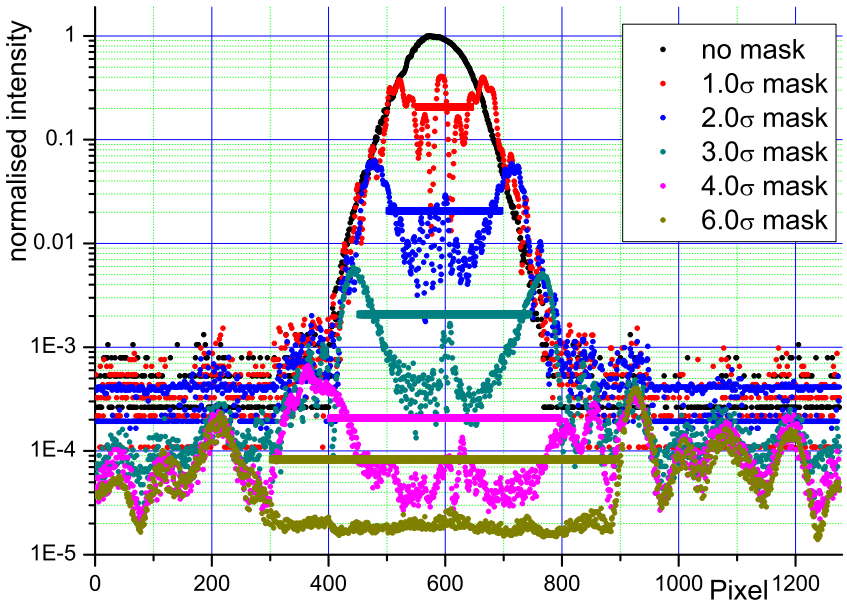

Figure 6.9: Laser images with various mask sizes with horizontal bars to indicate the mask size

The profiles for different mask sizes are displayed in Fig. 6.9. The horizontal lines mark the mask size of the data set with the corresponding colour. Since the mask is manually positioned for each image, the actual mask position may vary within a 20 pixel range. In the central region a strong interference pattern is visible which is generated by the mask. But since this is not the region of interest, the pattern does not disturb the measurement.

However, some weaker wiggles are also visible outside the beam core for the 3σ, 4σ, and 6σ mask measurements. Intensity and shape of this pattern are independent of the mask size and they are therefore not caused by the mask.

For further analyses of this pattern, the laser is directly shot onto the CCD-camera with such a high exposure time that the central part is overexposed but the outer region are still visible. To prove that these wiggles are really part of the intrinsic laser profile, the laser is rotated around the beam axis. If the pattern is part of the laser profile, it will rotate together with the laser.

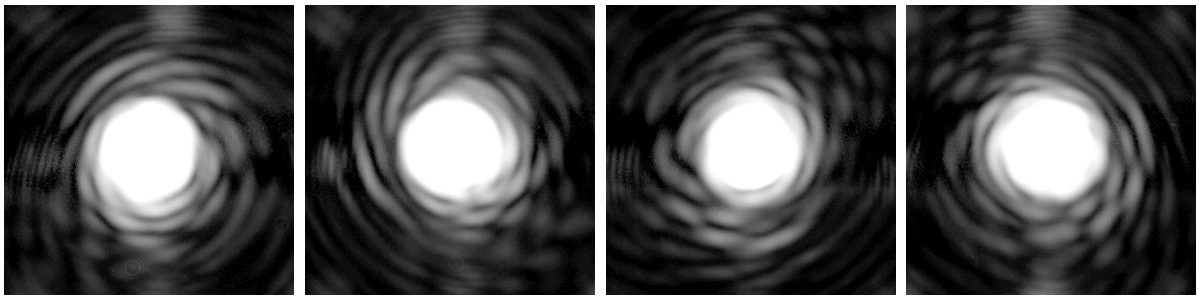

(a) 0° rotated laser (b) 90° rotated laser (c) 180° rotated laser (d) 270° rotated laser

Figure 6.10: rotated laser beam profile

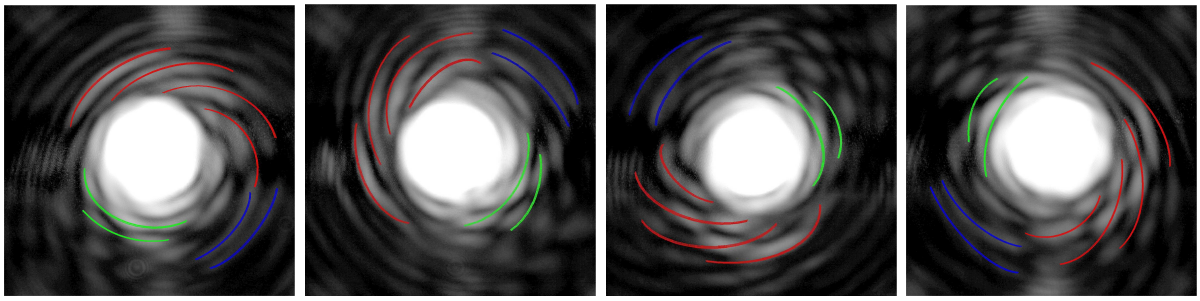

(a) 0° rotated laser (b) 90° rotated laser (c) 180° rotated laser (d) 270° rotated laser

Figure 6.11: markings for characteristic structures in the laser profile

In Fig. 6.10, the thereby acquired images are shown. Even though the exposure time is chosen high enough that the central part is fully overexposed, the outside patterns are still very weak. Therefore, the grey scale of the image was set logarithmically to increase the contrast. Some characteristic structures within the laser profile are marked in Fig. 6.11. The comparison of the images confirms that there are pattern outside the beam core which are part of the intrinsic laser profile. But since the core intensity is not measurable due to the overexposure, no quantitative analysis of this pattern is possible. Final proof is brought by the comparison with a measurement by the CID-camera that is capable of acquiring the whole profile.

The limitation to the dynamic range due to the distorted Gaussian profile has underlined the necessity to pose restrictions on the intensity distribution that the masking technique can be applied on. The distribution obviously has to be monotonously decreasing in radial direction. In addition, in order to make the rescaling of the mask possible, the intensity distribution has to satisfy the condition $\mathrm{I}((\alpha x)^2 + (\alpha y)^2) = \text{const.}\ \forall\ \alpha \in \mathbf{R}, \forall\ x, y \in D$.

6.7.2 Iris Correction

Since the laser does not have a sufficiently high dynamic range, an iris is used to "cut off" the pattern outside the beam core. The iris is placed in front of the DMD to ensure not to cut off diffraction patterns created by the DMD. As the DMD and the mask can generate interference patterns, it is important to include the iris in front of the DMD in order not to cut off any interference patterns caused by the DMD.

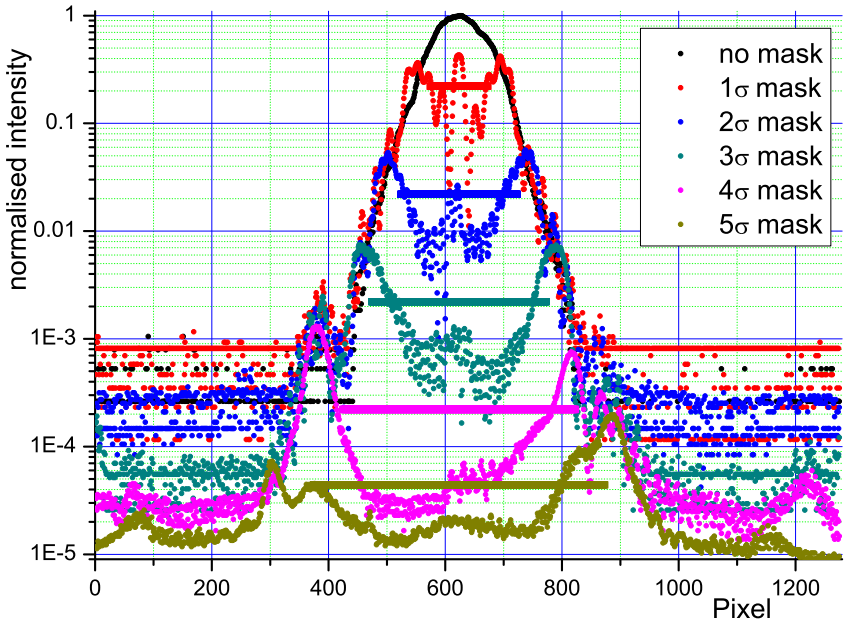

Figure 6.12: Laser images with various mask sizes and an iris to cut off outer laser beam profile patterns with horizontal bar to indicate the mask size

Results of measurements using an iris correction are given in Fig. 6.12. The iris has generated a nice flat background which is required for the calculation of the dynamic range. The background is identified on the pixels outside pixel no. 250 and pixel no. 1000. The standard deviation in this region of the projected camera output is calculated to be 0.91. This number needs to be rescaled by the exposure time of 600 ms yielding 0.0015. With a maximum observable signal of 253, rescaled by the exposure time of 559 μs to 452, this grants a total dynamic range of about 5.5 orders of magnitude.

This method of determining the background using an iris will no longer be possible for the spatial mode filter setup, described in section 6.7.3. In this case, the background must be determined in one of the corners where the effect of scattered light is lowest. A rectangle of 30×60 pixels is chosen. This grants the dynamic range of the two-dimensional image, which might differ from the dynamic range of the one-dimensional projection. For a better comparison, the dynamic range of the 2D data is also calculated here. The standard deviation of the background in the 5σ mask image was 0.28. This violates the

claim that any background deviation of a CCD-camera is larger than 0.5 and the minimum standard deviation of 0.5 is therefore chosen for further calculations and is rescaled by the exposure time of 600 ms to $8.3 \cdot 10^{-4}$. With a maximum signal of 255 rescaled to 456, a dynamic range of 5.7 orders of magnitude was determined.

6.7.3 Spatial Mode Filter

In the method described above the undesired pattern outside the laser beam core is cut off by an iris. This way, the mask always has to be smaller than the iris to observe a reasonable signal. To overcome this limitation a spatial mode filter can be used to generate a perfect Gaussian beam profile instead of cutting off the fringes. The basic principle of a spatial mode filter was explained in section 4.7.

The major challenge of setting up the spatial mode filter is the high precision adjustment of the lenses and the pinhole. If the focussing lens is not positioned centrally on the beam axis or tilted, the focal point will be shifted in transverse direction, which makes the re-collimation of the beam by the second lens impossible. This effect is comparably small but the positioning of the spatial mode filter with respect to the laser needs to be checked before each measurement. If the pinhole is misplaced in the transverse direction, the beam profile is strongly distorted in one direction. By the use of the micrometer screws, this positioning is done very precisely and its negative effects can almost be neglected.

A more serious problem is the longitudinal position of the pinhole. In case of a longitudinal misplacement of the pinhole, it is not exactly located in the Fourier plane of the focussing lens. The Fourier transform will still have a spatial component that creates a strong interference pattern when passing through the pinhole. The correct longitudinal adjustment of the pinhole mainly determines the dynamic range of the resulting Gaussian distribution of the laser beam.

Additionally, the distance between the two lenses needs to be set precisely to avoid any total focussing or defocussing effect of the spatial mode filter. This is a major issue for the core masking technique since a smaller laser beam also requires a smaller mask, which will create a wider interference pattern. For previous measurements this interference pattern was concealed in the central beam core where it did not do any harm. A wider interference pattern could superimpose the halo and thereby prevent its precise measurement. However, a defocussed laser beam might become too large to be observed on the limited CCD-camera chip.

The most reliable method of adjusting the spatial mode filter was achieved by first positioning the pinhole with respect to the first focussing lens. If the focal point of the lens does not match the pinhole, a lot of light will be backscattered. By minimising the scattered light between lens and pinhole, the longitudinal and transverse position of the

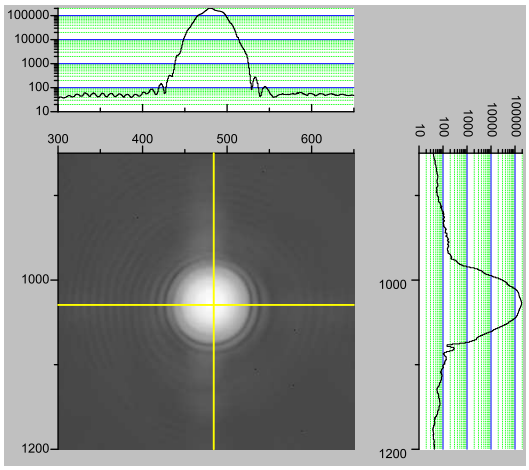

(a) CID-measurement of a laser profile corrected by a spatial mode filter

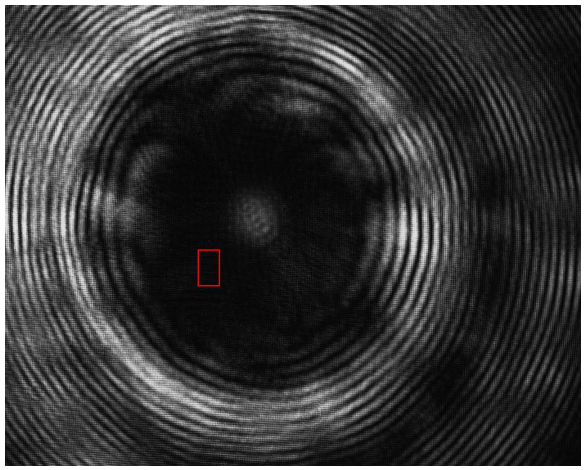

(b) Weakly illuminated area for background calculation of 4σ mask measurement

Figure 6.13: Profiles of laser beam corrected by a spatial mode filter with horizontal bar to indicate the mask size

pinhole can be adjusted very precisely. For the positioning of the second lens, a total focussing effect of the spatial mode filter must be avoided. It proved to be most accurate to focus the laser to a distant point.

In Fig. 6.14, the results of a flexible core masking technique measurement for several mask sizes are shown. As a measure of the quality of the spatial mode filter, a Gaussian distribution is fitted to the data without mask included. It matches the acquired data neatly over more than four orders of magnitude. In addition, a counter measurement is performed using the CID-camera, shown in Fig. 6.13(a).

In the outer halo regions shown in Fig. 6.14, a strong interference pattern is visible which is generated by the spatial mode filter and dominates the signal in this region. Due to alignment problems, an iris cannot be included in this setting to correct this effect. The background required for the dynamic range calculation therefore needs to be taken from the lowest illuminated region.

In a 30×60 pixel size region, shown in Fig. 6.13(b), the standard deviation of the signal is 4.61. Rescaled by the exposure time of 750 ms and a 100 times weaker neutral density filter, the standard deviation of the light intensity is found to be $61.5 \cdot 10^{-6}$. With the maximum signal of 255, rescaled by the exposure time of 3.6 ms to be 70.8, the dynamic range is calculated to be $1.1 \cdot 10^{6}$. The increase of the dynamic range of an 8 bit CCD-camera with a dynamic range of 256 by a factor of 4000 to up to over six orders of magnitude by the flexible core masking technique is a great improvement which allows for beam halo measurements and testing theoretical calculations which are normally of the order of 10^{-4} [60].

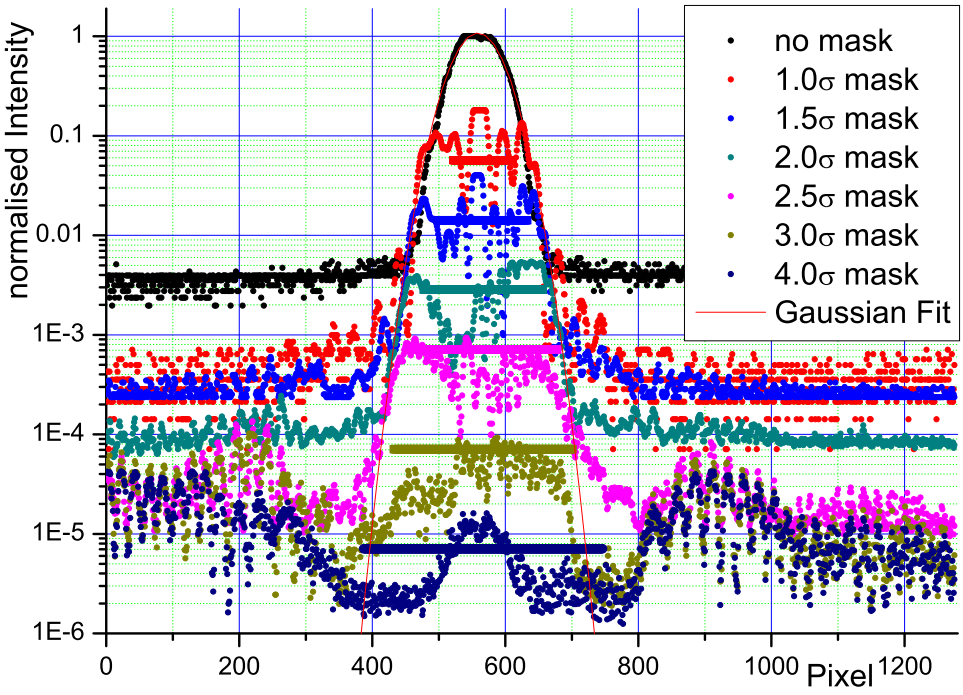

Figure 6.14: Profiles of laser beam with various mask sizes corrected by a spatial mode filter

6.8 Conclusion and Outlook

It was shown that the flexible core masking technique is capable of to significantly increasing the dynamic range of ordinary CCD-cameras. The dynamic range of an 8-Bit camera was increased by a factor of 4000 to over six orders of magnitude. This exceeds the dynamic range of most simulations which have been performed so far and will therefore be sufficient for any kind beam halo measurements.

The interference pattern generated by the DMD was found to be a minor problem since the maximum of the pattern was of the same shape as the original beam and the high angle between two neighbouring maxima allowed for their separation. The interference pattern generated by the mask was confined in the central region for $1/e^2$ beam diameters larger than 0.5mm but superimposed the outer halo region for smaller diameters and made measurements impossible in this region.

Despite these drawbacks, the flexible core masking technique grants a dynamic range almost as high as a CID-camera at much lower costs and with far higher acquisition rates. With a 40kHz frame rate of the DMD, the acquisition rate is only limited by the exposure time of the CCD or the operation speed of the PC. In addition the whole setup is much smaller in size than the CID-camera and could thus be easily put underneath a radiation shield.

The dynamic range measured by the flexible core masking technique was still limited by

the non-ideal laser beam profile that did not grant the high dynamic range required for such measurements. The technique as such may well be suited for even higher dynamic ranges.

7 Summary

A beam of charged particles in an accelerator or storage ring normally consists of an almost Gaussian shaped beam core and some tail distribution which is refered to as the beam halo. Although there is no general definition of the halo, it is usually a region in the beam profile that is close to the dense core of the beam, but with a particle density that is several orders of magnitude lower. Particles in the halo region of the beam distribution are very likely to get lost in the accelerator and thus reduce the experimental output, lead to an increase of signal background and, in high energy machines, even risk to severly damage the machine or its experimental installations. A thorough understanding of beam halo formation and transport along with a possible control or suppression of these particles is thus highly desirable for essentially any particle accelerator.

Computer simulations and halo models can only be tested and benchmarked if beam instrumentation exists that is able to measure the beam profile with a sufficiently high dynamic range. Few monitors are able to achieve a dynamic range of 10^6 or more and most of them have to intercept the beam with all kinds of unwanted effects. The aim of this thesis was to identify methods that are able to measure the beam profile of essentially any kind of charged particle beam in a non- or least disturbing way.

Light emitted by a beam of charged particles, such as synchrotron radiation, or generated by the beam in the form of optical transition radiation or luminescent screens is linear to the beam charge over a wide range and thus an ideal way of determining the beam profile. A core idea of the here-presented work was to develop a monitor able to detect this light with a high dynamic range and without restricting the monitor to a specific accelerator environment.

First, the angular distribution of synchrotron radiation and transition radiation were analyzed in detail and it was found that a laser beam can be used as a good approximation of both radiation types. A compact laboratory test stand was designed and built up consisting of a shielding box for background suppression and a breadboard for mounting different optical set ups.

Second, the novel SpectraCam XDR charge injection device camera was mounted and characterized in this test stand. Its dynamic range was determined for different exposure times and pre-exposure settings. This allowed for beam profile measurements with a dynamic range of up to 10^7 for sufficiently long exposure times. For short exposure times, it was found that the dynamic range scales linear with the exposure time. It was demonstrated that CID cameras can also be applied for short exposure even though they cannot deploy their full potential in this regime.

Since CID cameras are expensive devices with some limitations for short exposures times,

an alternative method was investigated in the frame of this thesis: A digital micro mirror device was used to provide a flexible mask to shield the intense light from the beam core from a conventional 8 bit CCD camera. A Visual Basic code was developed to control both the camera and the micro mirror array. Based on a first image acquisition, the beam core was defined, sent to the mirror array and then the halo region was remeasured with a different light attenuation realized by neutral density filters. It was shown that this method allows for greatly increasing the dynamic range of the camera by a factor of 4000! The high image acquisition rate that thus became available combined with the possibility to tremendously increase the dynamic range of a cheap CCD camera makes the flexible core masking technique an interesting option for future beam halo monitors.

Both monitors investigated in the frame of this thesis provide the opportunity for high dynamic range beam profile measurements in the order of 10^6 to even 10^7. This is comparable to the best halo monitors presently available and at least two orders of magnitude above all existing halo models. Since both monitors rely on the exploitation of light from the particle beam, they are highly generic and can be applied to essentially all different kinds of particle accelerators and storage rings. These monitors thus clearly have a very high potential for a future benchmarking and challenging of existing halo models as well as for the optimization of accelerator operation.

A Calculation of Optical Transition Radiation for tilted and 3D Surfaces

Depending on the optics used to capture and refocus the OTR light from the screen onto the camera system an decrease in light intensity toward the screen edges might be observed which is a result of non-ideal optics.

This effect can be counteracted if one does not rely on flat OTR screens, but adds an initial focusing by giving the screen a parabolic surface. This will increase the overall light transmission to the camera and eventually improve the signal quality. This section contains calculations done for the specific case of CTF3. As the focus of the work was later shifted to low energy machines, like UMER or the USR, it was moved to the Annex.

Optical transition radiation is a valuable tool for beam diagnostics and its potential use exceeds by far the simple use of beam profile monitoring discussed in this thesis. Since the angular distribution of OTR is energy dependant it can be used, e.g. for emittance measurements. A camera has to be focused on the OTR screen to measure the beam profile, while another monitor measures the angular distribution of the OTR light. Since the opening angle is given by $\theta \approx 1/\gamma$, the beam energy can be derived from its angular distribution. By providing the opportunity to measure the profile and the divergence of the beam at the same time, OTR allows for a single shot emittance measurement.

Because of this broad range of applications, optical transition radiation and its angular distribution is worth a closer analysis. A possible way to derive OTR is the virtual photon model. Due to the introduction of boundary conditions, the virtual photons become real and are emitted as OTR. Based on this model, Reiche et al. have derived the energy per frequency and solid angle to be [14]

$$W = \frac{\omega^2 q^2}{4\pi^4 c^3} \left| \int dxdy \frac{\omega}{\gamma v} \frac{x}{r} \cos(\theta) K_1 \left(\frac{\omega r}{\gamma v} \right) \exp -i\vec{k}\vec{r} \right|^2 \tag{A.1}$$

In this equation, K_1 is the Bessel-function, x, y and $\vec{r} = (x, y)^T$ the transverse coordinates, and $\vec{k}$ the wave vector of the emitted light. Any arbitrary surface expressed as $z(x, y)$ is represented in the phase factor $\vec{k}\vec{r} = k(x \sin(\theta) + z(x, y) \cos(\theta)$. For the case of an infinite flat foil, i.e. an integration from $-\infty$ to ∞ and $z(x, y) = 0$, this can be simplified to

$$W = \frac{q^2}{4\pi^2 c} \left(\frac{\beta^2 \sin(2\theta)}{1 - \beta^2 \cos^2(\theta)} \right)^2 \qquad [14] \tag{A.2}$$

For beam diagnostics, a finite foil is used. The approximation of an infinite plane might not suffice any more but calculations for finite foils are required. An additional point of interest is the dependency of OTR on the foil shape. For reasons given in the introduction

it might be sensible to use curved foils to improve the overall signal output.

A.1 Mathematica Calculations

Equation A.1 can be solved numerically by Mathematica. To control the correctness of the implementation in Mathematica the OTR calculation done in [14] is performed. The calculated angular distribution of the OTR intensity at a wave number of $2\pi/$ mm generated by a $\gamma = 100$ electron beam passing through a vertical foil is shown is Fig. 1.1(a). The foil was chosen to be of 10mm×10mm size. On a logarithmic scale, the impact of the finite size of the insertion foil is clearly visible. Instead of a monotonously decreasing curve as expected for an infinite plane, an interference pattern is visible which are consistent the calculations performed in [14]. This matches theoretical predictions which state that the OTR of the infinite plane can be considered as the superposition of the OTR of a finite plane and the *optical diffraction radiation (ODR)* of the complementary plane.

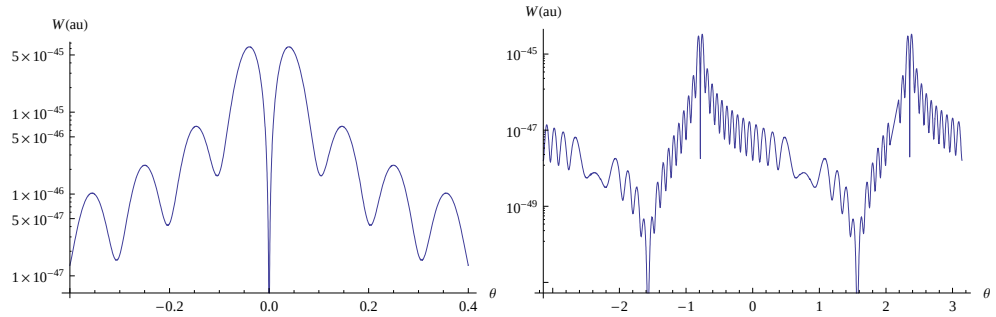

(a) Calculation of OTR for a foil perpendicular to the beam line

(b) Calculation of OTR for a foil in a 45° angle

Figure A.1: Calculation of OTR with a wave number of $2\pi/1$ mm of an electron beam with γ=100 generated by a 10mm×10mm size foil

For the same specification the angular distribution of OTR generated by an electron beam passing through a metal foil tilted by 45° is presented in Fig. 1.1(b). The OTR is no longer emitted in the forward direction, but under -45° and 135°, i.e. perpendicular to the foil. Due to relativistic effects the angular distribution of OTR is strongly energy dependent. The angular distribution of OTR generated by an electron beam of various energies passing through a metal foil tilted by 45° is calculated and the results are shown in Fig. A.2. The wavelength was chosen to be 10 μm. Shorter wavelength in the optical regime caused problems during the integration of equation A.1.

For higher energies the angular distribution is much narrower due to the Lorentz-boost. The two peaks, clearly separated for high energies, merge together for lower energies. The energy at which the two peaks merge together also depends on the frequency of the OTR

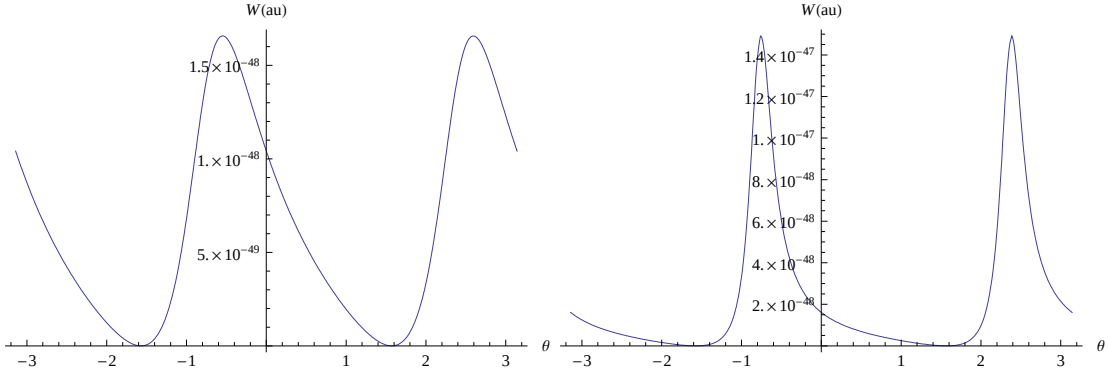

(a) Calculation of OTR for a 10 keV electron beam

(b) Calculation of OTR for a 100 keV electron beam

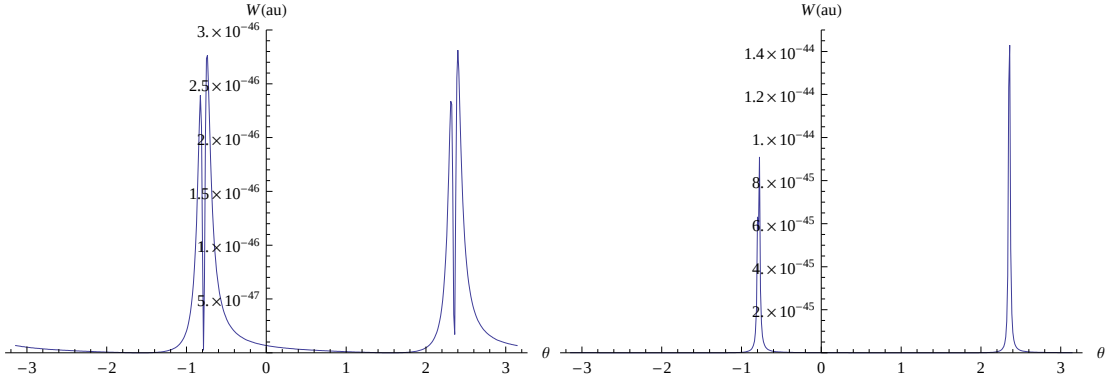

(c) Calculation of OTR for a 1,000 keV electron beam

(d) Calculation of OTR for a 10,000 keV electron beam

Figure A.2: Calculation of OTR of an electron beam of different energies passing through a 10mm×10mm size foil tilted by 45°

light, as it can be seen in Fig. A.3 for an 100 keV electron beam. Higher energies also caused problems during the integration of equation A.1. For shorter wavelengths, the two separated peaks merge together in the same way as it happened for low beam energies.

The calculated emission perpendicularly to the foil is in contradiction to previous calculations performed by R. Fiorito for instance [61]. For the case of a 10keV electron beam passing through an infinite plane at normal incidence, the angular distribution derived from equation A.2 is compared to the so called Ginzburg-Frank formula [61, 11, 62]:

$$W = \frac{q^2\beta^2}{\pi^2 c}\frac{\sin^2(\theta)}{(1-\beta^2\cos^2(\theta))^2} \tag{A.3}$$

The calculated angular distributions are presented in Fig. A.4. The calculation in Fig. 1.4(a) has two maxima located in the foil plane. S. Reiche argues that his theory is more reliable since according to his equation the intensity drops to zero in the foil plane, i.e. at $\pi/2$, as shown in Fig. 1.4(b) [14].

For comparison the OTR emitted by a 10 keV electron beam passing through an infinite foil in normal incidence is calculated by numerically integrating equation A.1. The an-

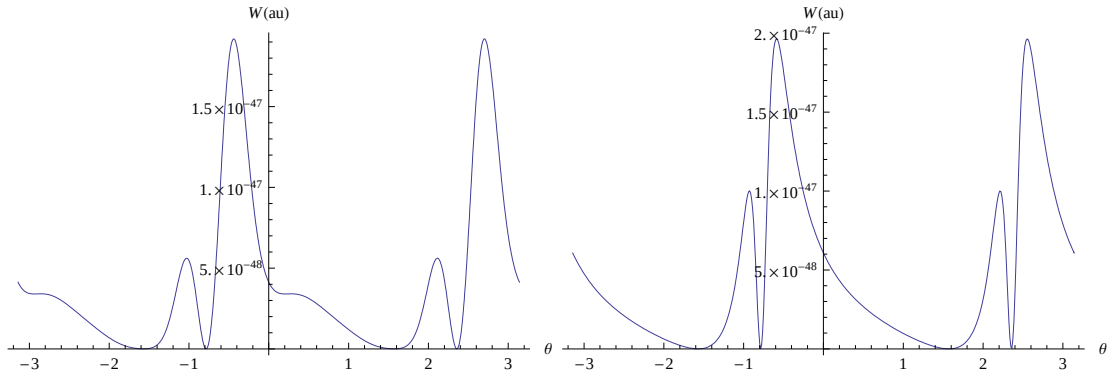

(a) Calculation of OTR at 10 mm wavelength (b) Calculation of OTR at 1 mm wavelength

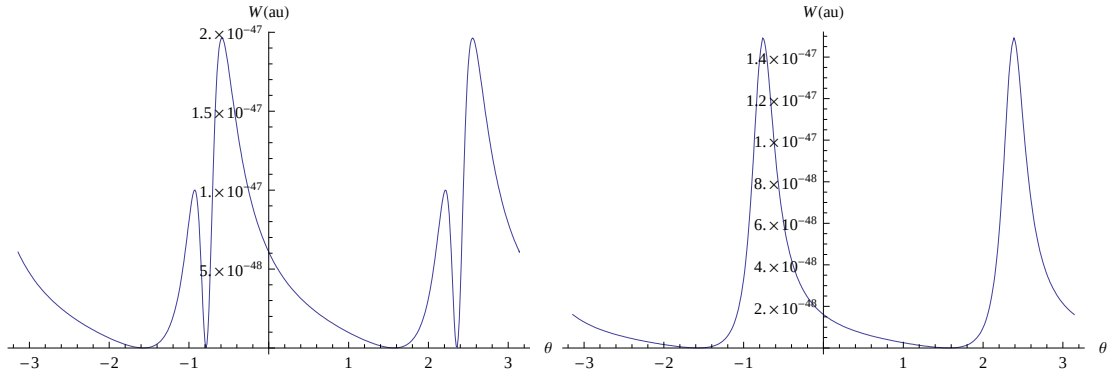

(c) Calculation of OTR at 100 μm wavelength (d) Calculation of OTR at 10 μm wavelength

Figure A.3: Calculation of OTR of different frequencies generated by a 100 keV electron beam passing through a 10 mm×10 mm size foil tilted by 45°

gular distribution matches. The intensity varies slightly which is due to the frequency dependency that is neglected in the approximation of equation A.2.

To check the consistency of the calculation, angular distributions for two different angles between the velocity and the foil normal vector, 5.7° and 26.6°, are calculated. The maxima are located at -0.1 rad (−5.7°) and -0.5 rad (−26.6°) which indicates the consistency of the calculation.

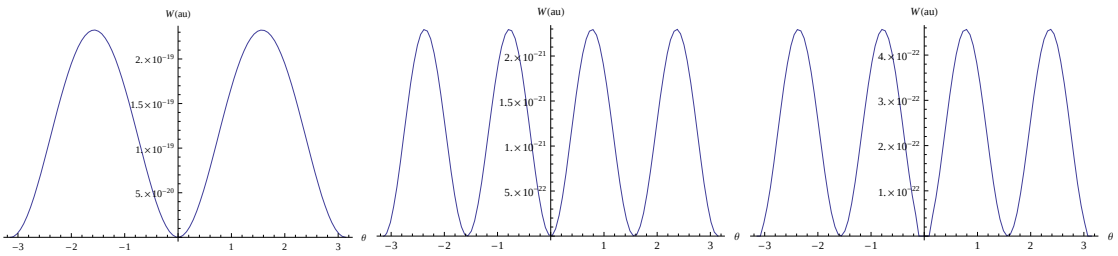

(a) Calculation based on an approximation of R. Fiorito (b) Calculation based on an approximation by S. Reiche (c) Calculation of the exact equation of S. Reiche for an 10 mm×10 mm foil

Figure A.4: Calculation of OTR form a 10keV electron beam passing through an infinite foil at normal incidence

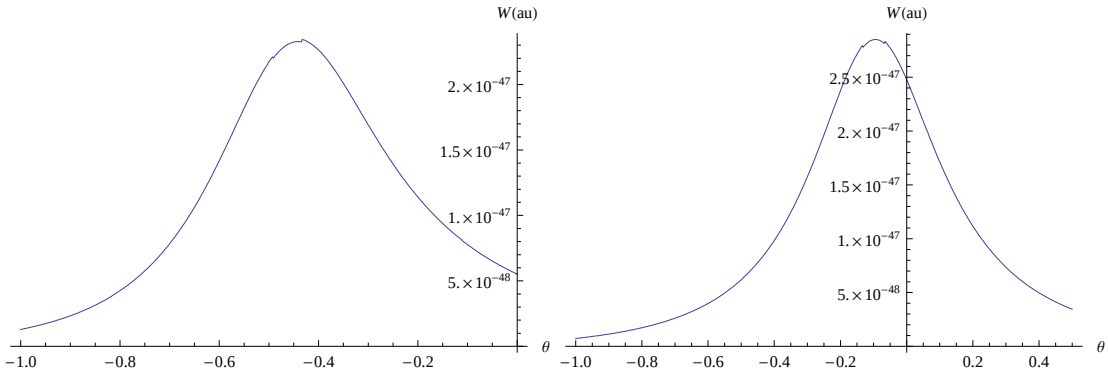

(a) Calculation of OTR for foil tilted by 26.6° (b) Calculation of OTR for foil tilted by 5.7°

Figure A.5: Calculation of OTR of 10 μm generated by a 100 keV electron beam passing through a 10 mm×10 mm size foil tilted by different angles

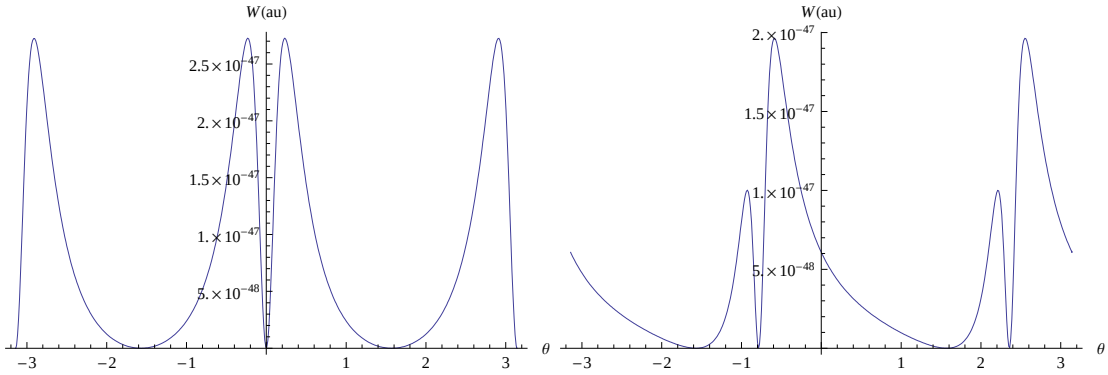

(a) Calculation of OTR for a parabolic foil, $z = x^2$ (b) Calculation of OTR for sinusoidal foil, $z = \sin(x)$

Figure A.6: Calculation of OTR of 10 μm generated by a 100 keV electron beam passing through a 10 mm×10 mm size foil of different shapes

An additional interesting question is how curved foils influence the OTR emission. Non-ideal optical elements required for focusing the OTR onto the camera system reduce the light intensity and might cause distortions. If these optical elements could be partially substituted by an appropriately shaped foil, it would increase the overall light transmission towards the camera and improve the signal. The effect of curved foil on OTR and there expected focusing properties are of great interest for the design of beam profile monitors. Calculations are done for a parabolic foil, presented in Fig. 6(a), and for a sinusoidal foil, presented in Fig. 6(b). The calculated distributions have a great resemblance with a perpendicular foil or a foil tilted by 45° respectively. Apparently, only the slope of the foil at zero crossing is relevant for the angular distribution.

A.2 Conclusion

The angular distribution of OTR for a point like beam of different energies, light wavelengths, foil angles and shapes was calculated. The effects of these variations were clearly visible. Against expectations, the variation of the shape of the foil had only a limited impact on the angular distribution. Apparently, it only depends on the slope of the surface at the incidence point.

Due to the computational power requirements, it was impossible to calculate OTR for high energies or low wavelengths in the visible range by a numerical integration of equation A.1. The calculations based on the equation derived by S. Reiche differ from calculations performed based on the Ginzburg-Frank formula, as well as from calculations and measurements done by Wartski [13]. This indicates the limitations in the usage of Reiches equation.

B Graphics

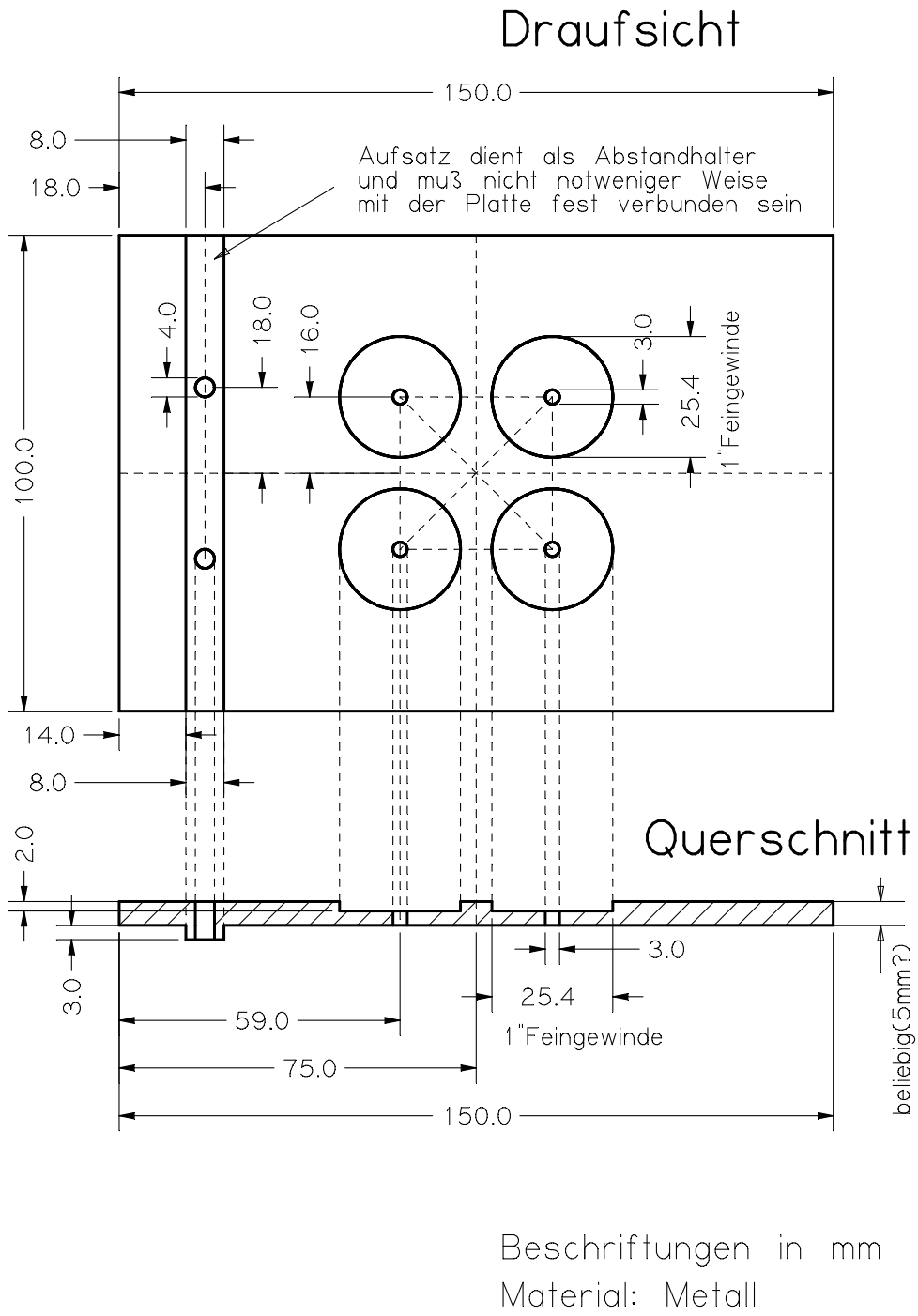

Figure B.1: Design drawing of the mask

C Used abbreviations

*.bmp	Bitmap
CCD	Charge coupled device
CID	Charge injection device
CLIC	Compact linear collider
CTF3	CLIC test facility 3
COTR	Coherent optical transition radiation
DMD	Digital micro mirror device
DR	Dynamic range
FLASH	Free electron laser in Hamburg
*.gif	graphics interchange format
ILC	International linear collider
IP	Internet protocol
*.jpg	joint photographic expert group
KV	Kapchinskij-Vladimirskij
LEDA	Low energy demonstration accelerator
LHC	Large hadron collider
MB	Maxwell-Bolzmann
MMA	Micro mirror array
NDRO	Non-destructive readout
ODR	Optical diffraction radiation
OTR	Optical transition radiation
PMT	Photomultiplier tubes
PSR	Los Alamos proton storage ring
RAI	Random access integration
SR	Synchrotron radiation
*.txt	Text
UMER	University of Maryland electron ring
XDR	Extreme dynamic range

D Computer programs

D.1 background correction

```
#include <iostream>
#include <fstream>
#include <string>
#include <sstream>
#include <vector>

using namespace std;

int main()
{
ofstream ausgabe("daten/dataoutput.txt"); //define output file
   ifstream file("daten/datafile.txt"); //define input file containing
                                          image data
   string line;
   int n=0;

   vector < vector < double > > info2;
   ifstream file2("daten/background.txt"); //define input file containing
                                             background
   while ( getline(file2, line) )
   {
      vector < double > data;
      double value;
      istringstream iss(line); //read background
      while (iss >> value)
      {
         data.push_back(value);
      }
      if(n>=3){
      info2.push_back(data);
      }
      n++;
   }

   n=0;
```

```
   while ( getline(file, line) ) //read image
   {
      int m=0;
      double value;
      istringstream iss(line);
      while (iss >> value)
      {
      if(n>=3)
              {
              ausgabe<<(value-info2[n-3][m])<<"           ";
//output corrected image data
              }
      m++;
      }
      if(n>=3)
             {
             ausgabe<<endl;
             }
      n++;
   }
   system("PAUSE");
}
```

D.2 Image Projection

```
#include <iostream>
#include <fstream>
#include <string>
#include <sstream>
#include <vector>

using namespace std;

int main()
{
ofstream ausgabe("daten/output.txt"); //define output file
   vector < vector < double > > info;
   ifstream file("daten/input.txt"); //define input file
```

```
   string line;
   int n=0;
   while ( getline(file, line) ) //read input
   {
      vector < double > data;
      double value;
      istringstream iss(line);
      while (iss >> value)
      {
         data.push_back(value);
      }
      if(n>=3){
      info.push_back(data);
      }
      n++;
   }
double summe=0;
for ( int j = 0;  j<info[1].size(); j++)
   {
      double profile=0;
      for ( int i = 1175; i < 1185; i++) //define projection range
      {
          if ( info[i][j]>0)
          {
             profile=profile+info[i][j]; //project over 10 rows
          }
      }
      ausgabe<< profile/10<<endl; //average
      summe=summe+profile;
   }
   system("PAUSE");
}
```

References

[1] L. Maiani. The large hadron collider project. *Fusion Engeneering and Design*, 46:433–447, 1999.

[2] G. Wilkinson. LHC-B: overview and recent developments. *Nuclear Instruments and Methods A*, 384:119–125, 1996.

[3] A. Di Ciaccio. Status and commissioning of the ATLAS experiment at the LHC. *Nuclear Instruments and Methods A*, 602:682–686, 2009.

[4] Y.P. Sun, J. Gao, Z.Y. Guo, and W.S. Wan. International linear collider damping ring design based on modified FODO arc cells. *Physical Review Special Topics - Accelerators and Beams*, 11:061001, 2008.

[5] N. Muchnoi, H.j. Schreiber, and M. Viti. ILC beam energy measurement by means of laser Compton backscattering. *Nuclear Instruments and Methods A*, 2009.

[6] I. Wilson. The compact linear collider CLIC. *Physics Reports*, 403-404:365–378, 2004.

[7] V.M. Biryukov, V. N. Chepegin, Y. A. Chesnokov, V. Guidi, and W. Scandale. Crystal collimation as an option for the large hadron colliders. *Nuclear Instruments and Methods B*, 234:23–30, 2005.

[8] K. Wille. Synchrotron radiation. *Joint Universities Accelerator School, Archamps, France*, 2008.

[9] K.Wille. Synchrotron radiation sources. *Reports on Progress in Physics*, 54:1005–1068, 1991.

[10] I Frank and J Ginzburg. J. Physics USSR 9, 353, 1945.

[11] L Wartski. Interference phenomenon in optical transition radiation and its application to particle beam diagnostics and multiple scattering mesurements. *Journal of Applied Physics*, 46:3644–3653, 1975.

[12] Beth Gitter. Optical transition radiation. Technical report, UCLA department of Physics, 1992.

[13] L. Wartski, J. Marcou, and S. Roland. Detection of optical transition radiation and its application to beam diagnostics. *Proceedings of Particle Accelerator Conference, San Fransisco, USA*, 1973.

[14] J.B. Rosenzweig S. Reiche. Transition radiation for uneven, limited surfaces. *PAC2001*, 2:1282–1284, 2001.

[15] C. Bal, E. Bravin, T. Lefèvre, R. Scrivens, and M. Taborelli. Scintillating screens study for leir/lhc heavy ion beams. *Proceedings of Diagnostics Particle Accelerator Conference, Lyon, France*, 2005.

[16] Saint-Gobain Crystals & Detectors. Scintillation Products. http://www.detectors.saint-gobain.com/, 2001.

[17] S. Bhaskaran, D. Baiko, G. Lungu, M. Pilon, and S. VanGorden. SpectraCam SPM - a camera system with high dynamic range for scientific and medical applications. *Prceedings of Spie*, 5902:59020D, 2005.

[18] F. Martinache, O. Guyon, A. Pluzhnik, R. Galicher, and S.T. Ridgway. Exoplanet imaging with a phase-induced amplitude apodization coronograph. ii. performance. *The Astrophysical Journal*, 639:1129–1137, 2006.

[19] G. Guerri, S. Robbe-Dubois, J-B. Daban, L. Abe, R. Douet, Ph. Bendjoya, F. Vakili, M. Carbillet, J-L. Beuzit, P. Puget, K. Dohlen, and D. Mouillet. Apodized lyot coronagraph for vlt-sphere: Laboratory tests and performances of a first prototype in the visible. *Instrumentation and Methods for Astrophysics*, 2009.

[20] T. Lefèvre, E. Braun, R. Corsini, D. Schulte, and A.L. Perrot. Beam halo monitoring at CTF3. *Proceedings of European Particle Accelerator Conference, Lucerne, Switzerland*, 2004.

[21] P. Cameron and K. Wittenberg. Halo diagnostics summary. European Particle Accelerator Conference Proceedings, Lucerne, Switzerland, 2004.

[22] A. Browman, M Borden, D. Fitzgerald, R. Macek, R. McCrady, T. Spickermann, and T. Zaugg. Halo measurements of the extracted beam at the los alamos national laboratory. *Proceedings of Particle Accelerator Conference, Portland, USA*, 2003.

[23] P. Cameron and K. Wittenberg. Halo diagnostics summary. *AIP Conference Proceedings*, 693:103–107, 2003.

[24] G. Turchetti, C. Benedetti, A. Bazzani, and S. Rambaldi. Collective effects and collisions in halo genesis and growth. *AIP Conference Proceedings*, 693:81–84, 2003.

[25] N.Pichoff. Intrabeam scattering on halo formation. *Proceedings of Particle Accelerator Conference*, 18:3277–3279, 1999.

[26] N. Pichoff, P-Y. Beauvais, R. Duperrier, G. Haouat, and J-M Lagniel D. Uriot. CEA studies on halo formation. *AIP Conference Proceedings*, 693:49–52, 2003.

[27] F. Toral, D. Burgos, J. L. Carrillo, I. Gutierrez, E. Rodriguez, S. Sanz, and C. Vazquez. Design, manufacturing and tests of a micrometer precision mover for ctf3 quadrupoles. *European Particle Accelerator Conference Proceedings, Genoa, Italy*, 2008.

[28] T.P. Wangler, K.R. Crandall, R. Ryne, and T.S. Wang. Particle-core model for transverse dynamics of beam halo. *Phyical Review Special Topics - Accelerators and Beams*, 1:084201–1 to 084201–9, 1998.

[29] I. M. Kapchinskij and V.V. Vladimirskij. Limitations of proton beam current in a strong focusing linear accelerator associated with the beam space charge. *Proceedings International Conference on high-energy accelerators and instrumentations*, 1959.

[30] I. Hoffmann and A.V. Fedotov. Summary of beam dynamics working group. *29th ICFA Advanced Beam Dynamics Workshop: Beam Halo Dynamics, Diagnostics, and Collimation (HALO03), Long Island, New York, USA*, 2003.

[31] G. de Rijk. The LEP magnet system at 100GeV. CERN Document Server, 1999.

[32] Flash. the free-electron laser in hamburg. http://flash.desy.de/sites/site_vuvfel/-content/e395/e2188/FLASH-Broschrefrs_web.pdf.

[33] E. Bravin and T. Lefèvre. OTR studies for the high charge CTF3 beam. *Proceedings of Particle Accelerator Conference, Portland, USA*, 2003.

[34] M. et al Reiser. The maryland electron ring for investigating space-charge dominated beams in a circular fodo system. *Proceedings of Particle Accelerator Conference, New York City, USA*, 1999.

[35] C .P. Welsch, M. Grieser, J. Ullrich, and A. Wolf. An ultra-low-energy storage ring at FLAIR. *Nuclear Instruments and Methods A*, 546:405–417, 2005.

[36] J.D. Gilpatrick. Wide dynamic-range beam-profile instrumentation for a beam-halo measurement: description and operation. *AIP Conf. Proc.*, 693:122–125, 2003.

[37] S. Igarashi, D. ARAkawa, k. Kiyomi, S. Hikaru, T. Toyama, and M. Yoshii. Flyingwire beam profile monitors at the kek ps main ring. *Nuclear Instruments and Methods in Physics Research A*, 482:32–41, 2002.

[38] http://www.umer.umd.edu/.

[39] M. et al Walter. Commissioning of the University of Maryland Electron Ring (UMER): Advance towerd multiturn operation. *Physics of Plasmas*, 13:056703–1 to 056703–5, 2006.

[40] http://pubweb.bnl.gov/users/diktys/www/Halo/.

[41] *Princeton Instruments: PI-MAX2-512 http://www.roperscientific.de/.*

[42] http://www.thorlabs.com/.

[43] Schott. Panelite backlights. http://www.spectraservices.com/.

[44] http://www.ids-imaging.de/.

[45] http://www.thermo.com/com/cda/product/detail/1,,10118190,00.html. *CIDTEC SpectraCAM 84 & 86.*

[46] C.P. Welsch, E. Bravin, B. Burel, and T. Lefvre. Operational experience with SpectraCam CID camera system. CERN - CLIC Note 657.

[47] M. J. Pilon. Racid exposure software time resolved spectroscopy (TRS) drivers. Technical report, Thermo Fisher Scientific, 2006.

[48] Quentin S. Hanley, J. Bruce True, and M. Bonner Denton. Evaluation of charge-injection cevices for in laue diffration imaging. *J. Synchrotron Rad.*, 2:215–228, 1995.

[49] Private communication.

[50] Uniblitz. CS35 shutter specifications, 02 2008.

[51] C.P. Welsch, E. Bravin, and T. Lefvre. A beam halo monitor based on adaptive optics. *Prceedings of Spie*, 6616:9, 2007.

[52] J. Egberts, S.Artikova, E. Bravin, T. Chapman, T. Lefèvre, M. Pilon, and C.P. Welsch. Design of a beam halo monitor with dynamic range. *Proceedings of Linear Accelerator Conference, Victoria, Canada*, 2008.

[53] J. Egberts, S. Artikova, and C.P. Welsch. Flexible core masking technique for beam halo measurements with high dynamic range. *Proceedings of Diagnostics Particle Accelerator Conference, Basel, Switzerland*, 2009.

[54] *DMD Discovery 1100 Controller Board & Starter Kit.*

[55] Don Russell. Texas instruments DLP technology industry leader in MEMS manufacturing, 2006. Presentation.

[56] Texas Instruments Technology. *DMD Discovery 1100 Chip Set*, 2004.

[57] DMD-frequently asked questions.

[58] T.J. Meyer, B.A. Mangrum, and M.F. Reed. Split beam micromirror. Technical report, Texas Instruments Inc., 2006.

[59] http://www.ti.com/.

[60] T. Shea and P. Cameron. Halo diagnostics overview. 29th ICFA Advanced Beam Dynamics Workshop: Beam Halo Dynamics, Diagnostics, and Collimation (HALO03), Long Island, New York, USA, 2003.

[61] A.G. Shkvarunets and R.B. Fiorito. Vector electromagnetic theory of transition and diffraction radiation with application to the measurement of longitudinal bunch size. *Phyical Review Sspecial Topics - Accelerators and Beams*, 11:012801–1 to 012801–14, 2008.

[62] S. Casalbuoni, B. Schmidt, P. Schmüser, V. Arsov, and S. Wesch. Ultrabroadband terahertz source and beamline based on coherent transition radiation. *Phyical Review Special Topics - Accelerators and Beams*, 12:030705–1 to 030705–13, 2009.

Erklärung:

Ich versichere, dass ich diese Arbeit selbständig verfasst habe und keine anderen als die angegebenen Quellen und Hilfsmittel benutzt habe.

Heidelberg, den .....